

PERFORMANCE TRACKING & CHARACTERIZATION OF COMMERCIAL  
SOLAR PANELS

A THESIS SUBMITTED TO  
THE GRADUATE SCHOOL OF NATURAL AND APPLIED SCIENCES  
OF  
MIDDLE EAST TECHNICAL UNIVERSITY

BY

CELAL GÜVENÇ OGULGÖNEN

IN PARTIAL FULFILLMENT OF THE REQUIREMENTS  
FOR  
THE DEGREE OF MASTER OF SCIENCE  
IN  
CHEMICAL ENGINEERING

FEBRUARY 2014



Approval of thesis:

PERFORMANCE TRACKING & CHARACTERIZATION OF COMMERCIAL  
SOLAR PANELS

submitted by **C. GÜVENÇ OGULGÖNEN** in partial fulfillment of the requirements  
for the degree of **Master of Science in Chemical Engineering Department,**  
**Middle East Technical University** by,

Prof. Dr. Canan Özgen \_\_\_\_\_  
Dean, **Graduate School of Natural and Applied Sciences**

Prof. Dr. Halil Kalıpçılar \_\_\_\_\_  
Head of Department, **Chemical Engineering**

Asst.Prof. Dr. Serkan Kıncal \_\_\_\_\_  
Supervisor, **Chemical Engineering Dept., METU**

**Examining Committee Members:**

Prof. Dr. İnci Eroğlu \_\_\_\_\_  
Chemical Engineering Dept., METU

Asst.Prof. Dr. Serkan Kıncal \_\_\_\_\_  
Chemical Engineering Dept., METU

Prof. Dr. Raşit Turan \_\_\_\_\_  
Physics Dept., METU

Assoc. Prof. Dr. Görkem Külâh \_\_\_\_\_  
Chemical Engineering Dept., METU

Eyüp Tongel \_\_\_\_\_  
ASELSAN

**Date:** 12.02.2014

**I hereby declare that all information in this document has been obtained and presented in accordance with academic rules and ethical conduct. I also declare that, as required by these rules and conduct, I have fully cited and referenced all material and results that are not original to this work.**

Name, Last name: C. Güvenç OGULGÖNEN

Signature:

## ABSTRACT

### PERFORMANCE TRACKING & CHARACTERIZATION OF COMMERCIAL SOLAR PANELS

Ogulgönen, C. Güvenç

M. Sc. Department of Chemical Engineering

Supervisor: Asst. Prof. Serkan Kınca

February 2014, 147 pages

This study aims to characterize the performance of different types of commercial solar panels in terms of the meteorological parameters such as irradiance, temperature, pressure, relative humidity with the technologies of mono and polycrystalline along with thin film, by evaluating the performance data collected with a Daystar MT-5 I-V curve tracer. The approach to this characterization is a comprehensive data collection scheme where solar panel performance is monitored side-by-side with an exhaustive list of atmospheric conditions gathered by the HOBO U30 Weather Station for two and a half years in the atmospheric conditions of Ankara. In addition to that, a light soaking station for accelerated module testing is designed, constructed and tested with the sample solar cells. Statistical analysis are made to calculate and evaluate the global performance metrics such as performance ratio and light soaking station successfully tracked and showed the change of performance for the sample cells.

**Keywords:** Photovoltaic cells, solar energy, degradation mechanism, performance modeling

## ÖZ

### TİCARİ GÜNEŞ PANELLERİNİN PERFORMANS TAKİBİ VE KARAKTERİZASYONU

Ogulgönen, C. Güvenç

Yüksek Lisans, Kimya Mühendisliği Bölümü

Tez Yöneticisi: Yrd. Doç. Dr. Serkan Kıncal

Şubat 2014, 147 sayfa

Bu çalışma, monokristal, polikristal, ince film gibi farklı teknolojilerde üretilmiş endüstriyel güneş panellerinin sıcaklık, güneş ışınması, basınç, bağıl nem gibi meteorolojik değişkenlere bağlı olarak performans karakterizasyonunun Daystar MT-5 I-V eğrisi takip ekipmanının topladığı veriler ile değerlendirilmesini amaçlamaktadır. Karakterizasyon yaklaşımı, çok sayıda veri toplanması ile aynı dış şartlara maruz bırakılan güneş panellerinin meteorolojik değişkenlere göre HOBO Meteoroloji Ekipmanı ile iki buçuk yıl boyunca Ankara şehri atmosfer şartlarında toplanan verilerin değerlendirilmesini içermektedir. Bunun yanında, bir güneş paneli yaşlandırma ünitesi tasarlanmış, inşa edilmiş ve örnek güneş gözeleri ile operasyonu test edilmiştir. Evrensel düzeyde Kabul edilen performans oranı gibi parametreler istatistiksel analizlerle hesaplanmış, karşılaştırılmış ve yaşlandırma ünitesi başarılı bir şekilde örnek gözelerin performansını takip edip değişimleri gözlemlemeyi mümkün kılmıştır.

**Anahtar Kelimeler:** Fotovoltaik hücreler, güneş enerjisi, bozunma mekanizmaları, performans modellemesi

**To my family**

## ACKNOWLEDGEMENTS

Firstly, I would like to thank to my supervisor Asst. Prof. Dr. Serkan Kınca for his great help on the thinking process and the hard work he put for this study. Without his great vision, guidance, understanding and belief in me, I would not have the motivation to go through this process.

I am grateful to Prof. Raşit Turan and The Center for Solar Energy Research and Applications (GÜNAM) for providing me the biggest support to conduct this study in a healthy and creative environment with all the tools needed.

Thank you Prof. Üner, for the ideas you seeded to our brains, for giving me the inspiration to start my graduate work and the motivation for writing my thesis. I promise I am going to fill the notebook that you gave to me with useful information.

I would also like to thank to my friends; Memo, Ata, Neco, İbo, Can, 2 Burcus, Must and all Block C residents for their endless support and for the laughs that make our days less boring most of the time. Without the things we shared, I would not be as happy as I am now, for sure.

I should also mention the staffs of our department Ertuğrul Özdemir, Süleyman Nazif Kuşhan, Adil Demir, İsa Çağlar, Mustafa Cansuyu for letting me learn from their technical knowledge and for the physical work they put together for this study. They are very good at what they do and they are also very kind and nice people to anyone willing to learn and share.

I also thank Assoc. Prof. Çerağ Dilek for her kindness and big effort to make my thesis writing process easier.

Apart from all of the valuable people above, my deepest gratitude, coming from my soul, are to my parents. Their unlimited love, support and confidence in me throughout my life made me who I am now.



## TABLE OF CONTENTS

ABSTRACT.....	v
ÖZ .....	vi
ACKNOWLEDGEMENTS.....	viii
TABLE OF CONTENTS.....	ix
LIST OF FIGURES .....	xiii
LIST OF TABLES .....	xvii
1. LITERATURE SURVEY AND BACKGROUND .....	1
1.1. Different Photovoltaic Technologies .....	1
1.1.1. Crystalline silicon.....	2
1.1.1.1. Single crystal silicon.....	4
1.1.1.1.1. Czochralski Growth (CZ):.....	5
1.1.1.1.2. Float Zone Method (FZ):.....	5
1.1.1.2. Multi crystal silicon .....	6
1.1.2. Thin film.....	9
1.1.2.1. Amorphous silicon.....	9
1.1.2.2. Cadmium telluride (CdTe) .....	11
1.1.2.3. Copper Indium Gallium Diselenide (CIGS).....	11
1.1.2.4. Group III-V.....	12
1.2. Panel Degradation Mechanisms .....	13
1.2.1. Overview for Common Degradation Modes .....	13
1.2.2. Physical Degradation Modes.....	19
1.2.2.1. Corrosion .....	19
1.2.2.2. Discoloration .....	20
1.2.2.3. Glass soiling: .....	21
1.2.2.4. Delamination .....	22

1.2.2.4.1. Front- side delamination:.....	23
1.2.2.4.2. Front grid and AR coating:.....	23
1.2.2.4.3. Bubbles:.....	24
1.2.2.5. Breakage and cracking cells .....	25
1.2.2.6. Potential Induced Degradation (PID) .....	26
1.2.2.7. Hot spots .....	27
1.2.2.8. Mismatched Cells .....	27
1.2.2.9. Temperature Induced Degradation .....	28
1.2.3. Light Induced Degradation.....	31
1.3. Performance Characterization Studies – Outdoor Testing Stations.....	37
1.3.1. PV Module I– V Characteristics.....	37
1.3.2. Effect of the type of PV technology .....	39
1.3.3. Ambient temperature .....	40
1.3.4. Solar Irradiation.....	40
1.3.5. Tilt Angle.....	41
1.3.6. Others .....	41
1.3.7. Evaluation of the PV Performance .....	41
1.3.7.1. Final yield (YF) .....	42
1.3.7.2. Reference Yield (YR).....	42
1.3.7.3. Performance Ratio .....	43
1.3.7.4. PVUSA Rating.....	43
1.3.7.5. Capacity Factor (CF) .....	44
1.3.7.6. System Efficiency .....	44
1.3.8. Outdoor Studies .....	44
1.4. Accelerated Testing in Light Soaking Station .....	49
1.4.1. Xenon Arc Lamps: .....	50
1.4.2. Fluorescent UV Lamps and Devices:.....	52
1.4.3. Metal Halide Lamps .....	54
2. EXPERIMENTAL SETUP .....	57

2.1. HOBO U30 Station.....	59
2.1.1. U30 Station Components .....	59
2.1.1.1. HOBO U30 Ethernet Data Logger .....	59
2.1.1.2. Solar Radiation Sensor (Silicon Pyranometer) S – LIB – M003.....	61
2.1.1.3. Rain Gauge Smart Sensor S – RGA – M002 .....	61
2.1.1.4. Temperature and Relative Humidity (RH) Smart Sensor .....	62
2.1.1.5. Wind Direction Smart Sensor S – WDA – M003 .....	63
2.1.1.6. Wind Speed Smart Sensor S – WMA – M003 .....	65
2.1.2. HOBOLink .....	65
2.2. Daystar Multi – Tracer.....	73
2.3. StellarNet Blue – Wave Spectrometer.....	78
2.4. FTP Server .....	80
2.5. Solar Module List and Justifications .....	82
2.5.1. Solar Modules List .....	83
3. LIGHT SOAKING STATION DESIGN.....	85
3.1. Overview of the Design .....	85
3.2. Choice of the Light Source .....	85
3.3. Choice of Instrumentation .....	88
3.4. Lamp Configuration and Station Housing Design .....	89
3.4.1. Single Light Source Characterization.....	91
3.4.2. Multiple Light Source Modeling.....	93
3.5. Finalized Design and Equipment.....	96
4. RESULTS AND ANALYSIS.....	99
4.1. PV Performance Monitoring Station Analysis .....	99
4.1.1. Data Integrity Issues.....	99

4.1.1.1.	Missing Data and Corrupt Sensor Problems.....	99
4.1.1.2.	Design Upgrade for Spectrophotometer (Shutter Arrangement).....	100
4.1.2.	Trend Analysis on Historical Climatic Data .....	100
4.1.3.	Correction for Module Tilt .....	112
4.1.3.1.	Determination of the Tilt Correction .....	112
4.1.3.2.	Yearly Trends of Solar Position .....	114
4.1.4.	Analysis of Solar Panel Performances .....	117
4.2.	LID Station Measurements .....	126
4.2.1.	Light Intensity Measurements .....	126
4.2.2.	Test Run of the Light Soaking Station .....	130
4.3.	Future Improvements .....	134
5.	SUMMARY AND CONCLUSIONS .....	135
	REFERENCES .....	137

## LIST OF FIGURES

Figure 1-1 Basic Flowchart for Crystalline PV Cell Production [8].....	3
Figure 1-2 Mono crystalline solar cell (left) and simplified cross-section of a mono crystalline solar cell (right)[6].....	4
Figure 1-3 Single crystal pattern.....	5
Figure 1-4 Structure of Polycrystalline Cell .....	6
Figure 1-5 Polycrystalline silicon solar cell.....	7
Figure 1-6 Crystalline Silicon Cell Production Steps Overview[6].....	8
Figure 1-7 Cross-section of a-Si solar cell.....	10
Figure 1-8 Cross-section of CdTe cell .....	11
Figure 1-9 Cross-section of CIGS cell.....	12
Figure 1-10 Circuit representation of a solar cell .....	14
Figure 1-11 A highly browned EVA encapsulation on a crystalline cell [29].....	16
Figure 1-12 An example of layers of a photovoltaic module [34].....	17
Figure 1-13 Encapsulation of a PV module [35] .....	17
Figure 1-14 Failure modes of PV modules caused by packaging material and detection methods.....	18
Figure 1-15 Visible corrosion at the edge of the cell.....	20
Figure 1-16 Discoloured solar cell [47] .....	21
Figure 1-17 Haziness that could be seen at the edge of the cell .....	22
Figure 1-18 Delaminated photovoltaic module [47].....	23
Figure 1-19 A PV module with bubbles on the back side [39].....	24
Figure 1-20 AR coating oxidation through the center of the cell .....	25
Figure 1-21 Severely broken glass on a polycrystalline PV module [59].....	26
Figure 1-22 Hot spot formation .....	27
Figure 1-23 Busbars help prevent the cracked cell producing lower current (a)crack removing the part of the cell from the circuit (b).....	28
Figure 1-24 Ambient Temperature Efficiency Relation .....	32
Figure 1-25 Electric Field for the Layers of CdTe Cells .....	34

Figure 1-26 Efficiency vs Time at Different Temperatures for a CdTe Cell .....	34
Figure 1-27 Effect of Cu Addition .....	35
Figure 1-28 Suggested Mechanism of Cu Diffusion.....	35
Figure 1-29 CIGS Cross - Section.....	36
Figure 1-30 Single diode model of a PV cell .....	37
Figure 1-31 Spectral distribution of a commercial Xenon lamp.....	51
Figure 1-32 Spectral distributions of a commercial Xenon lamp with different filters .....	52
Figure 1-33 Spectral distribution of UV – A&B lamps and sunlight.....	53
Figure 1-34 UV – A vs Sunlight behind the glass.....	54
Figure 1-35 Spectral distribution of a commercial metal halide lamp with the sunlight spectrum .....	55
Figure 2-1 Data Acquisition Flowchart.....	58
Figure 2-2 HOBO Weather Station .....	60
Figure 2-3 HOBO U30 Data Logger .....	60
Figure 2-4 Silicon Pyranometer S – LIB – M003 .....	62
Figure 2-5 Rain Gauge Smart Sensor.....	63
Figure 2-6 Temperature and RH Smart Sensor .....	63
Figure 2-7 Wind Direction Smart Sensor.....	64
Figure 2-8 Wind Speed Smart Sensor .....	65
Figure 2-9 Wind Speed & Direction Sensor Combined.....	66
Figure 2-10 Devices Tab Screenshot .....	67
Figure 2-11 An Overview of Graphs.....	67
Figure 2-12 Latest Conditions Pane .....	68
Figure 2-13 Latest Data Pane .....	68
Figure 2-14 A Sample .dtf File View from HOBOWare .....	69
Figure 2-15 Latest Connections Tab .....	69
Figure 2-16 Device Information Pane.....	70
Figure 2-17 Device Configuration Menu .....	70
Figure 2-18 Launch Configuration Menu .....	71
Figure 2-19 Readout Configuration Menu .....	72

Figure 2-20 Go to Alarms Menu.....	72
Figure 2-21 Daystar MT 5.....	73
Figure 2-22 Load and Control Units of Daystar MT5 .....	74
Figure 2-23 Web Server for MT5 .....	75
Figure 2-24 Settings Menu and Average Interval .....	76
Figure 2-25 Peak Power Setting.....	76
Figure 2-26 FTP Server Screen for MT – 5 .....	77
Figure 2-27 Index of .mtd and .xml Files.....	77
Figure 2-28 StellarNet Blue -Wave Spectrometer .....	78
Figure 2-29 Screenshot from SpectraWiz. Episodic Data Capture with Two Different Spectrometers .....	78
Figure 2-30 UVN Spectra of Sunlight .....	79
Figure 2-31 Entrance Screen for FTP Server.....	81
Figure 2-32 Datascreen in the FTP Server.....	81
Figure 2-33 HOBO Folder and Files.....	82
Figure 2-34 All panels in the station .....	82
Figure 2-35 Daystar MT – 5 load (below) and control unit (top) .....	83
Figure 3-1 The patented light soaking design [114] .....	86
Figure 3-2 Side and Top view of LID Station .....	86
Figure 3-3 Spectral Distribution for Xe Flash Lamp [115] .....	87
Figure 3-4 Spectral Distribution of a Metal Halide Lamp [116] .....	88
Figure 3-5 Picture of the Chassis with the cards installed .....	89
Figure 3-6 Picture of the single light source and the starter .....	91
Figure 3-7 Single light source intensity distributions - intensity measurements are in terms of $w/m^2$ and grid data are in terms of cm. ....	92
Figure 3-8 Various orientations of the 9 lamps considered .....	93
Figure 3-9 Distribution at 45 cm lamp separation and 50 cm between the lamps and the panels.....	95
Figure 3-10 Average intensity as a function of separation - inverse square behavior	96
Figure 3-11 The Final Construction of the Light Soaking Stat.....	98
Figure 4-1 Shutter Design.....	101

Figure 4-2 Reference Temperature Data throughout 2010 – 2013 .....	102
Figure 4-3 Reference Solar Irradiation Data throughout 2010 – 2013 .....	103
Figure 4-4 Temperature Data Comparison.....	104
Figure 4-5 Pressure Data Comparison .....	104
Figure 4-6 Relative Humidity Data Comparison .....	105
Figure 4-7 Wind Speed Data Comparison .....	106
Figure 4-8 Wind Direction Data Comparison .....	107
Figure 4-9 Solar Irradiance Data Comparison .....	108
Figure 4-10 Solar Irradiance Data Comparison for Below Region.....	109
Figure 4-11 Solar Irradiance Data Comparison for Above Region .....	110
Figure 4-12 Corrected HOBO Irradiance vs. Reference .....	111
Figure 4-13 Solar Zenith Angle .....	116
Figure 4-14 Tilt Correction Factors by Time of day, colored by month.....	117
Figure 4-15 Maximum Power vs. Short Circuit Current for Installed Panels.....	120
Figure 4-16 Maximum Power vs. Open Circuit Voltage for Installed Panels .....	121
Figure 4-17 Maximum Power vs Fill Factor for Installed Panels .....	121
Figure 4-18 Maximum Power vs Series Resistance for Installed Panels .....	122
Figure 4-19 Maximum Power vs Shunt Resistance for Installed Panels .....	123
Figure 4-20 Performance Ratio Comparison .....	123
Figure 4-21 Performance Ratio vs Temperature for Installed Panels .....	126
Figure 4-22 Performance Ratio vs Relative Humidity for Installed Panels.....	127
Figure 4-23 Performance Ratio vs Pressure for Installed Panels .....	127
Figure 4-24 Light Intensity as a Function of Time at 47 cm Table to Lamp Separation .....	128
Figure 4-25 Typical Contour Plots.....	129
Figure 4-26 Temperature vs Time Plot for Different Points in the LID Station.....	131
Figure 4-27 Time Period when the Cooling Fans are Turned off .....	131
Figure 4-28 I- V Curve under Different Illuminations for 1 Cell Module.....	132
Figure 4-29 I - V Curve under Different Illuminations for 4 Cell Module.....	133
Figure 4-30 Voc Change for 4 Cell Module .....	133
Figure 4-31 Voc Temperature Relationship for 4 Cell Module .....	134



## LIST OF TABLES

Table 1-1: Main categorization for PV technologies [3] .....	1
Table 1-2 Crystal Grain Sizes of Common PV Technologies .....	3
Table 1-3 Summary of key characteristics of commercial PV modules .....	13
Table 1-4 Physical Degradation Modes Breakdown [65] .....	29
Table 1-5 Thin-film failure modes and mechanisms [66].....	30
Table 1-6 STC, SOC and NOC Definitions .....	39
Table 1-7 Summary of Outdoor Station Findings .....	48
Table 0-1 List of Installed Solar Modules.....	84
Table 3-1 Summary of the simulation results .....	97
Table 4-1 Summary for Correction Values of Meteorological Parameters .....	111
Table 4-2 Summary of Data Points.....	119
Table 4-3 Grouping Radiation Levels.....	119
Table 4-4 Statistical Comparison of Panel Performance Ratios .....	125
Table 4-5 Summary Statistics for Light Intensity Distribution.....	130



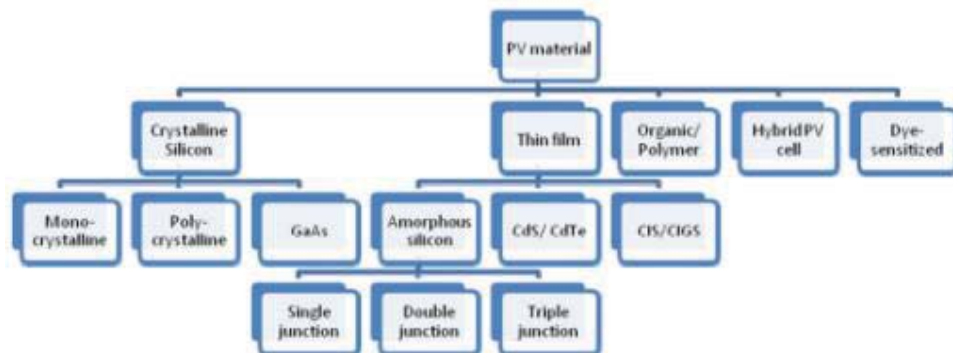
# CHAPTER 1

## LITERATURE SURVEY AND BACKGROUND

### 1.1. Different Photovoltaic Technologies

Photovoltaics are used in several different markets namely, satellites, telecommunications, cathodic protections which requires DC voltages for the corrosion prevention purposes for metals, water pumping and treatment in remote regions, solar home systems, energy need in remote houses, consumer products like battery chargers with certain power needs as well as grid connected power supply systems.[1] Photovoltaic technologies could be categorized like Table 1-1 below. Crystalline silicon and thin film technologies are the most widely used modules while there are other applications like organic/polymer, hybrid and dye-sensitized solar cells. Therefore, photovoltaic technologies can be categorized under three main groups: [2]

**Table 1-1:** Main categorization for PV technologies [3]



### **1.1.1. Crystalline silicon**

Crystalline silicon (c-Si) modules occupy 85-90% of the global PV market [4]. Crystalline silicon is the most commonly used technology for commercial applications. It has advantages of having a very well known standardized processing and having an abundant source of feedstock silicon. The main disadvantages for crystalline silicon technology are the need for high purity, therefore expensive silicon and having a competition in terms of feedstock with the electronics industry. Basically, crystalline solar cells have many different types varying from non-crystalline to multi crystalline technologies. The main categorization could be summarized as below;

Current commercial single crystal solar modules have conversions around 14 to 20% and their efficiency is expected to rise up to 23% until 2020. [5]

There are three main industries that are related to the crystalline silicon solar cell and module production:

- Metallurgical and chemical silicon production plants
- Ingot and wafer fabrication facilities for crystalline solar cell (mono and poly)
- Solar cell and module production facilities

The cost division for the crystalline solar cell modules could be roughly divided to 50% for silicon substrate, 20% for processing the cell and 30% for the processing of the module. Therefore, the price of the silicon remains as the most important cost parameter for the PV industry. [6]

The main differences between these technologies are the crystal grain size and different techniques that are used for growing the crystals.

**Table 1-2** Crystal Grain Sizes of Common PV Technologies

Crystal Type	Symbol	Crystal Grain Size	Common Growth Technique
Single crystal	sc-Si	>10 cm	Czochralski (Cz) Float-Zone (FZ)
Multicrystalline	mc-Si	10 cm	Cast, Spherical, Sheet, Ribbon
Polycrystalline	pc-Si	1 μm – 1 mm	Evaporation, CVD, sputtering

Manufacture of c-Si modules involve steps including growing ingots of silicon, slicing the ingots into wafers for the formation of solar cells, establishing the connections between cells and making the necessary encapsulation for the cells to form a complete module with reasonable voltage and current values.

Figure 1-1 Figure 1.1 shows the main steps mentioned above for the production of a crystalline solar module. [7]



**Figure 1-1** Basic Flowchart for Crystalline PV Cell Production [8]

Three types of silicon are mainly used in this procedure: single crystalline silicon (sc-Si), multi crystalline silicon (mc-Si) and ribbon sheet crystal (c-Si). [9]

#### 1.1.1.1. Single crystal silicon

Single (mono) crystalline cell modules constitute the 80% of the PV market. Single crystalline silicon is produced by crystal growth techniques. Solar cells with the reasonable performance parameters are generally produced by using silicon. Silicon has an indirect band gap of 1.1eV having indirect band gap causes silicon to have low light absorption, but this problem could be overcome by using a silicon with several hundred microns thickness and purifying it for reducing the defects in the crystal structure for decreasing rate of recombination therefore allowing minority carriers penetrate to the depletion region without high losses. [10]

Single crystalline silicon cells have some advantages. By using this technology, efficiencies around 20% could be achieved. [11] Single crystal cells are mainly produced for electronics industry. On the other hand, they require a high purity feed stock (around 99.9% pure silicon). Along with the production method and feedstock qualities, single crystal modules require higher cost for production with a slower process line. In addition to that, feedstock is wasted in a greater rate because of the circular shape of the cells and that also leads to lower packing density in panels. In single crystal form, all atoms are arranged in the same pattern. There are two commercial production techniques for single crystal silicon cells:

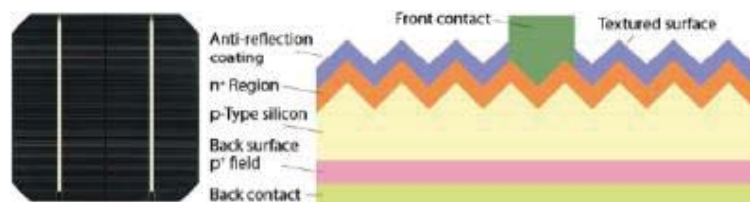


**Figure 1-2** Mono crystalline solar cell (left) and simplified cross-section of a mono crystalline solar cell (right)[6]

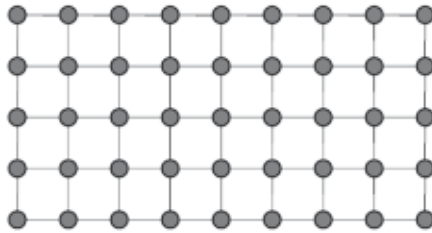


**Figure 1-3** Single crystal pattern

**1.1.1.1.1. Czochralski Growth (CZ):**

Most of the single crystal silicon cells are manufactured by CZ Growth Technique. It provides lower quality silicon than FZ with oxygen and carbon on the cell. However, it is cheaper compared to the FZ Growth and produces cylinders and circular wafers. In CZ Growth, pure silicon is melted in a quartz crucible under vacuum or inert gas environment and a seed crystal is dipped into the melt. After this, the seed is slowly taken out by slowly rotating in order to make the crystallization over the seed by the molten silicon. By adjusting the temperature, rotation and pulling rate, ingot size could be altered. One big crystal is formed as ingot and it has high purity and very few defects. The crystal does not include any boundaries since it is purely one crystal with only one orientation shown above. However, the crystal includes oxygen contaminated from the quartz crucible.

**1.1.1.1.2. Float Zone Method (FZ):**

The production is made on the cylindrical poly silicon rod. This special rod contains a seed in its lower end. A heating rod circling the rod starts to melt the silicon as it starts melting at the bottom moving towards the top. A single solid ingot is formed in the down region. Impurities stays in the molten part, therefore this method creates very high purity and low number of defects.

After the crystal growth process, the ingots are cut into thin wafers having width of 300  $\mu\text{m}$ . the cutting procedure is made by two main techniques:

- Wire sawing
- Diamond blade sawing

#### 1.1.1.2. Multi crystal silicon

Multicrystalline silicon solar cells are manufactured using two different methods. The first one is the ribbon silicon. In ribbon silicon technique, two filaments of graphite are put in a crucible with molten silicon in it. Then, the molten silicon is grown horizontally through capillary action between the filaments. This yields into a sheet of multicrystalline wafer. The thickness of the multicrystalline wafer could be adjusted by changing the width of the filament and the pulling speed. In addition to that, this method is cheaper than growing single crystal growth techniques and less silicon is wasted thanks to the change in the sawing methods (no circular shape is needed). On the other hand, produced multicrystalline cells have lower efficiencies compared to the single crystal cells because of the higher rate of defects and irregular surface structure characteristics.

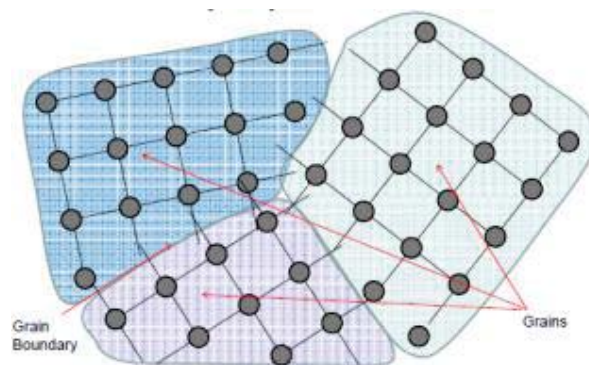


**Figure 1-4** Structure of Polycrystalline Cell



Poly & Multi Silicon is the second method for multicrystalline growth. Crystal growth is done in a large rectangular crucible by melting the silicon material. The molten material is slowly cooled with the control of temperature and direction of the cooling. Impurities in the molten material tend to place themselves on the edges since the edges cool slower. After the cooling is done, the edges are cut and etched off. These big blocks are then sliced into smaller blocks and then to the wafers.



**Figure 1-5** Polycrystalline silicon solar cell

Multicrystalline silicon solar cells have crystal grains with different sizes. They are cheaper to manufacture and processed faster than single crystal silicon cells. However, they are less efficient than mono crystalline cells due to the grain boundaries which cause electrical losses. The efficiency of the multicrystalline solar cells is expected to reach up to 21% in the long term and crystalline modules are expected to remain as the dominant technology until at least 2020. [12] The use of hydrogen is very important during the processing of the multicrystalline cells because hydrogen passivates the grain boundaries that cause electrical losses in the device. This procedure is mostly done by the technique called PECVD (plasma enhanced chemical vapor deposition) for the deposition of silicon nitride, which uses hydrogen, instead of silicon dioxide. Multicrystalline silicon cells generally have efficiencies 2-3% less than commercial silicon cells, however the cost of manufacturing multicrystalline cells are 20% less than single crystalline cells. [13]

There are several techniques to remove avoid impurities in the multicrystalline solar cell structure. One of them is the use of phosphorus getterings to bring the mobile impurities to the surface. [14] In addition to that, immobile point defects could be deactivated by the use of hydrogen passivation because atomic hydrogen could diffuse into the silicon material even at low temperatures. [15] In PECVD, silicon nitride antireflection coating is done using silane ( $\text{SiH}_4$ ) or ammonia ( $\text{NH}_3$ ) as the gas source. These gases work as the hydrogen source for the diffusion of hydrogen into the wafer. [16] Efficiencies of commercial multicrystalline silicon solar cells are between 14-19%. [17]

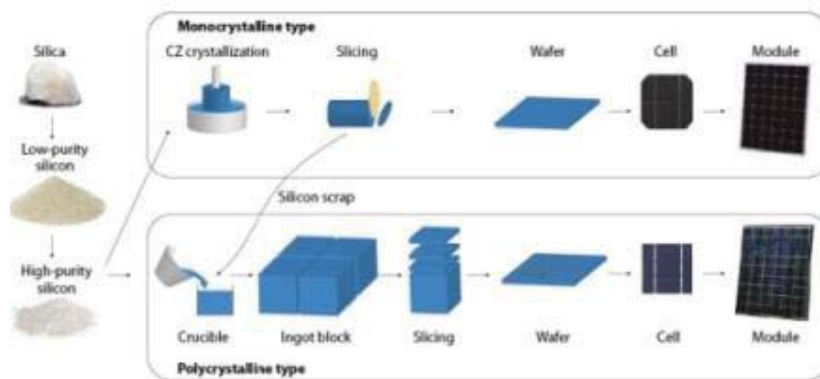


**Figure 1-6** Crystalline Silicon Cell Production Steps Overview[6]

The main difference between single and multi crystalline solar modules comes from the crystal growth step. Silicon that is purified by using several procedures are melted around  $1400^{\circ}\text{C}$  and a small crystal is cooled to be used as the seed for the crystal growth. When the seed is pulled out, it starts to solidify at the interface with the melt. If the pulling procedure is slow enough, the newly formed silicon atoms could arrange themselves according to the crystal structure of the seed. This form is a

single-crystal silicon ingot. On the other hand, silicon ingots could be produced by controlling the cooling rate of molten silicon while pouring it into a container. Ingots produced using this method could still be used in the making of a solar cell, but could not have the same quality with the previous mentioned crystal growth method. Basically, what obtained after the process are many little crystals or grains that are packed randomly instead of one large single crystal. Therefore, this is called multi crystalline silicon which also shows difference in the specialties like crystallization rate, ingot size and area. These ingots are then cut into wafers to form by using various different methods. [18]

### **1.1.2. Thin film**

Thin film solar cells are uses 1-10 microns of semiconductor instead of 200-300 microns as in crystalline types. Thin films are produced by the deposition of the semiconductor onto a cheaper glass substrate. One of the main advantages over crystalline solar cells is cost reduction in production of the cell thanks to use of cheap glass and less semiconductor material. However, the technology is more difficult in terms of producing good quality films that resulting in lower efficiencies compared to the crystalline solar cells.

There are three main categories of solar cells under thin film technology:

#### **1.1.2.1. Amorphous silicon**

Amorphous silicon cells are made by evaporating silicon onto a glass. Therefore, the orientation of the atoms becomes more random than the crystalline cells. Silicon has more unbounded hydrogen atoms and these unbounded electrons easily attract the impurities that result a decrease in the electrical performance of the cell. In order to deactivate the formed dangling bond, hydrogen is added to the material. Silane ( $\text{SiH}_4$ ) as the silicon source for the cell provides deposited hydrogen amount of ~%10. Hydrogenated silicon behaves totally differently than the pure silicon since its bandgap increases from 1.1 to 1.7 with improved electronic properties. However, this amount of hydrogen causes cell to lose some of its performance right after the sunlight exposure. [16]

For a-Si technology, cell efficiencies are around 13% while the module efficiency is around 6-8%. [15]

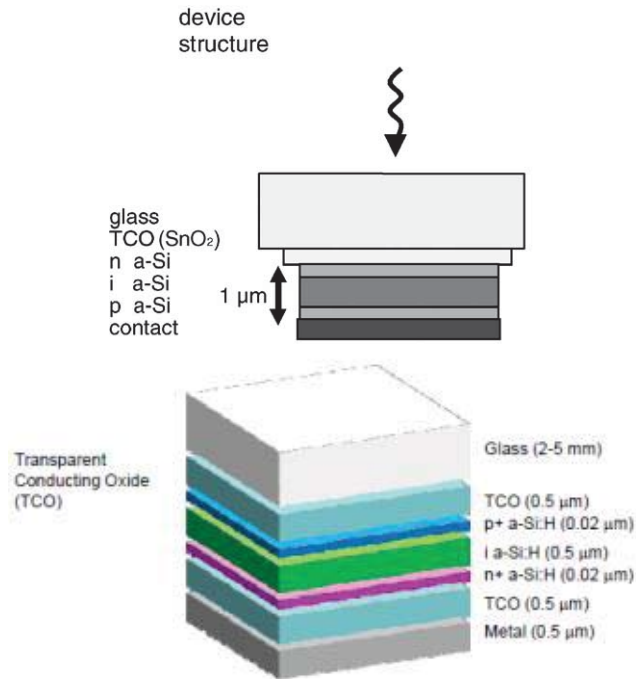


**Figure 1-7** Cross-section of a-Si solar cell

a-Si technology have some advantages like ability to absorb both low and high intensity light. In addition to that, a-Si cells cost less than crystalline cells because of the lower use of semiconductor material and using cheap glass as the surface for the deposition. Lastly, high temperatures do not affect the a-Si cell performance drastically. On the other hand, a-Si modules have lower efficiency compared to crystal technology and material degradation occurs after the long period of use. One other disadvantage of a-Si solar cells is the hazardous gases that are required for production. These gases create problem after the lifetime of the cell is over, in the termination and recycle procedure.

### 1.1.2.2. Cadmium telluride (CdTe)

p-type part of the cell is made by Cadmium and Telluride and n-type part is made by Cadmium Sulfide. CdTe technology offers high efficiencies for thin film technologies (over 16%). However, manufacturing requires high processing temperatures and the module itself becomes unstable and easily degraded. As mentioned above, toxicity is another problem for this technology. Cadmium is a poisonous element and the disposal of the module is not cost effective. In addition to that, CdTe cells are vulnerable to water penetration which causes degradation in cell's electrical performance.

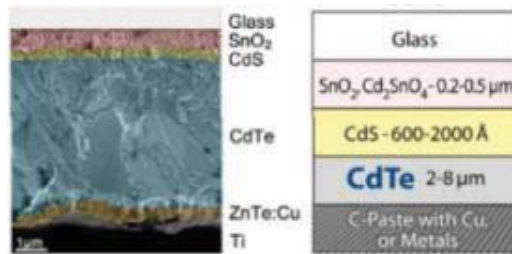
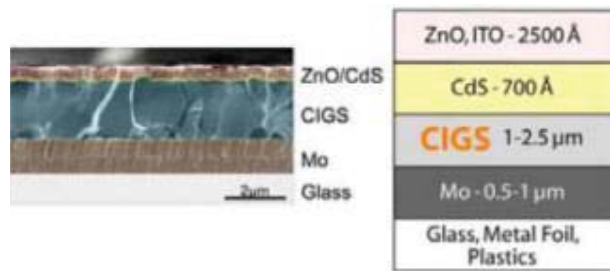


Figure 1-8 Cross-section of CdTe cell

### 1.1.2.3. Copper Indium Gallium Diselenide (CIGS)

CIGS modules have extremely good light absorption rates (99% of the light is absorbed in the first micron of the cell). That is because the elements used in the technology are the optimal ones for PV applications in terms of their absorption coefficients. Especially, the addition of Ga increases the light absorption band gap in the solar spectrum. Performance of CIGS modules does not degrade over time and it provides the highest efficiency values among the thin film technologies (19%).



**Figure 1-9** Cross-section of CIGS cell

CIGS modules have the advantage of high efficiency, but Gallium and Indium are the scarce and expensive elements. Another drawback is that the production procedure requires high vacuum applications.

#### 1.1.2.4. Group III-V

Group III-V cells are produced from the compounds of III and V group elements on the periodic table. This technology is mostly used in the electronics industry and space applications. They have very high efficiencies, but the production cost is very high too. They can also create multi-junction cells in order to increase the efficiency further. Gallium Arsenide (GaAs) and Indium Phosphide (InP) are the single junction III-V cells. Best efficiency is around 27.6% in this single junction technology. These cells have very high efficiencies and low weights and in addition to these, they are durable to the damage that could be done by the cosmic radiation. However, they are very expensive to produce and require materials that are not very abundant. Group III-V cells are also used in creating multi-junction solar modules. Multi-junction cells are basically the p-n junctions put on top of each other. Each junction has different band gap energies, so different regions of the solar spectrum are absorbed in each junction. Like GaAs and InP modules, multi-junction cells are very expensive to produce and offer high efficiencies up to 35.2%. They are used widely in extra terrestrial applications.

**Table 1-3** Summary of key characteristics of commercial PV modules

<b>Technology</b>	<b>Material thickness (<math>\mu\text{m}</math>)</b>	<b>Area (<math>\text{m}^2</math>)</b>	<b>Efficiency (%)</b>	<b>Surface area (<math>\text{m}^2</math>)</b>
Mono – c – Si	200	1.4 – 1.7 (typical)	14 – 20	~7
Multi – c – Si	160	1.4 – 1.7 (typical) 2.5 (up to)	11 – 15	~8
a – Si	1	~1.5	4 – 8	~15
a – Si / $\mu\text{c}$ – Si	2	~1.4	7 – 9	~12
CdTe	~1 – 3	~0.6 – 1	10 – 11	~10
CIGS	~2	~0.6 – 1	7 – 12	~10

## **1.2. Panel Degradation Mechanisms**

### **1.2.1. Overview for Common Degradation Modes**

Serving life of a photovoltaic module mostly depend on the stability and durability to corrosion of the construction parts of the cell itself since there are no moving parts on a photovoltaic solar cell by default. The guaranteed lifetime of a solar module could be around 20-25 years depending on the technology; however there are different failure modes and degradation mechanisms that could decrease the lifetime of the module. In most cases, these conditions that could decrease the performance and lifetime of the cells result from temperature and water ingress into the module.

There are degradation and failure modes of PV modules that could cause a gradual decrease in performance or a permanent overall loss in the performance of the

module for a long time. Gradual decrease in the performance of the module could be caused by;

- Increase in  $R_s$  due to decreased adherence of contacts or corrosion. The cause is usually water vapor.
- Decrease in  $R_{sh}$  due to metal migration through the p-n junction
- Damaging of the antireflection coating.

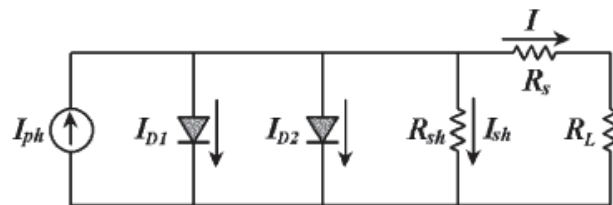


**Figure 1-10** Circuit representation of a solar cell

$I_{ph}$ : photogenerated current

$R_{sh}$ : shunt resistance

$R_s$ : series resistance

$R_L$ : load resistance

$I_{sh}$ : shunt current

The source of the series resistance could be resistances in the termination points of junction box, resistances in connection between the cells, busbars or in emitter regions. Series resistance decreases the voltage of the PV cell causing a decrease in the general performance of the module. During the manufacturing and the design process of the module, series resistance is decreased to a minimum level. However, thermal cycling conditions in the outdoor environment causes series resistances to a slow increase. [19]



Shunt resistance creates highly conductive regions in the solar cell, especially on the edges.

Shunt resistance results in shunt current whose value is very different from the intended load. This affects the cell performance badly especially at low intensity of light. The main reason behind the shunt resistance is the defects in the crystal structure of the cell or the impurities near the junctions. Shunt resistance problem in thin film solar cells occurs after long time of exposure to light. [20]. If the number of shunts increases in the cell, this leads to the increased effective shunt currents and decreased shunt resistances. [21]

A photovoltaic module could under perform because of several reasons. It could be due to shading of the module, or just a part of the cell by an object depending on the position of the sun during the day. The front surface of the module, which actually absorbs the sunlight, could be blocked by soiling and this may cause up to 10% of performance loss on the average. In a multi module system, failure of one module could happen or the interconnection between the modules could fail, however these cause reversible power reductions.

When one module is considered, there could be short circuits at cell interconnections. This is a common failure mode for thin film cells as the top and back contact is very close to each other and this increases the chance of short circuits through pin holes or from the damaged parts of the cell.

Another commonly observed failure mode is the open circuited cells due to the cracking in the module. This may be due to several reasons such as;

- Thermal stress
- Damaged parts during the manufacture and assembly of the module.

These are called latent cracks because they can not be detected during the quality control tests and failure occurs after some time. A cell could still operate after cracking thanks to the interconnect cell busbars which are the parts of the cell to protect the rigidity. Thermal stress and wind loading could cause interconnect open circuit failures. There could be open circuits in the junction box and bus wiring parts

of the module. In module scale, the open circuits could be due to manufacturing defects. After the module is exposed to outdoor conditions, the insulation material could degrade. This results in the delamination, cracks or corrosions. There could be serious cracks of the front glass of the module due to handling issues, harsh outdoor conditions like strong wind, heavy rain or snow and mostly hail. Delamination problem could occur mostly due to the weakening of the bond strength. The cause to the weakening could be the physical conditions like weather or photothermal aging and stress by moisture which causes irregular expansions on the structure of the parts of the cells and module. Hot spots could occur after the mismatch, cracks or shading happens meaning the high temperature gradients around the certain regions of the cell or between the cells. Bypass diodes are used to avoid the overheating problem. UV light could cause encapsulant material to lose its concentration and rigidity as the aging happens. Encapsulant failure could happen although UV absorbers and some encapsulant stabilizers could increase the lifetime of the encapsulant material. Leaching and diffusion could cause the encapsulation material to degrade and EVA browning because of the acetic acid formation could cause the performance of arrays of modules gradually, especially in concentrating systems. [22] [23] EVA browning issue is a problem that has been observed since 1980s. However, what is responsible for this issue has not been solved until 1994. [24] [23] [25] [26]

In 1994, indoor tests showed that glasses which contain cerium oxide prevent EVA browning since the glass does not let UV lights below 350 nm pass into the cell. [27] [28]

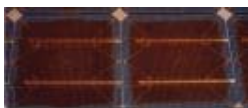


**Figure 1-11** A highly browned EVA encapsulation on a crystalline cell [29]

When the cell or module is exposed to UV light, it causes corrosion in solder bonds and electrical contacts. [30] [31] [32] This also increases the leakage current. [33]

A PV cell consists of materials of four different kinds in general: glass, metals, polymers and semiconductor. Front cover of a PV cell is made of glass while the frame is generally metal, encapsulation material is a polymer and the solar cell itself consists of a semiconductor. Back sheet of the module is often a polymer or glass. Junction box could be a metal or polymer while cables, string connectors consist of metals.

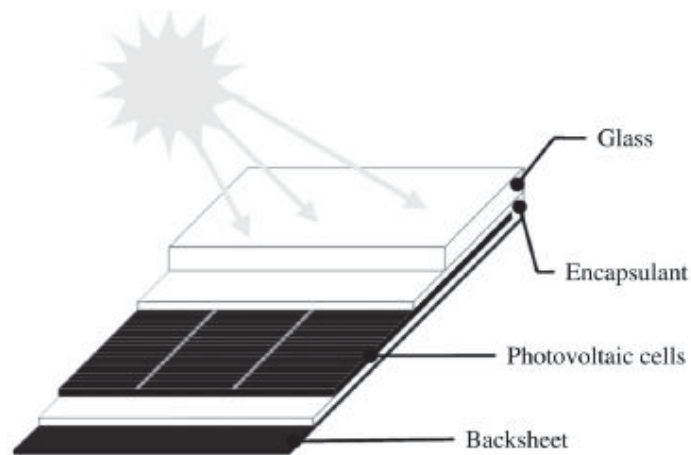


**Figure 1-12** An example of layers of a photovoltaic module [34]

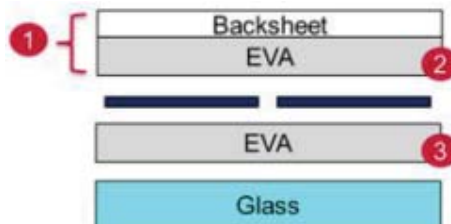


**Figure 1-13** Encapsulation of a PV module [35]

Mostly observed physical failure modes could be categorized as [36]:

- Encapsulant and back sheet browning or yellowing
- Delamination of encapsulant and backsheet
- Bubbling
- Busbar oxidation
- Busbar discoloration
- Connection corrosion
- Back sheet cracking
- Formation of hot spots and regions
- Breakage of cells
- Micro cracks

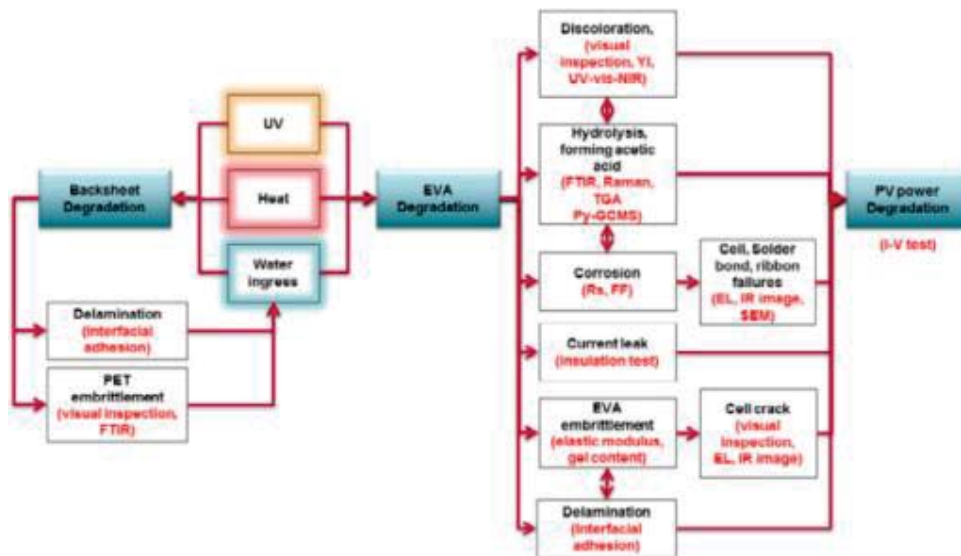


**Figure 1-14** Failure modes of PV modules caused by packaging material and detection methods

In almost all cases, the main cause of the physical degradation is temperature, humidity, water penetration or UV light intensity.

### **1.2.2. Physical Degradation Modes**

Lanoy and Procaccia (2005) described the degradation as the gradual deterioration of the characteristics of a component or of a system which may affect its ability to operate within the limits of acceptability criteria and which are caused by the operating conditions. When a PV module degrades, it still could operate, but not in the optimal values. After the module degraded for a certain rate (around 20%), module performance could create problems (Charki et. al, 2012). Numerically, a PV module is counted as degraded if it performs 80% of its initial power value. (Wohlgemuth et. al 2005). Physical degradation on PV modules could be categorized under four main subtitles[37]:

#### **1.2.2.1. Corrosion**

The main cause behind the corrosion is the moisture. [38]

Corrosion badly affects the metallic parts of the module causing the leakage currents. It also harms the adhesive surface between the metallic frame and the cell itself. [39]

According the accelerated tests that Wohlgemuth and Kurtz conducted, after 1000 h of exposure to 85% humidity and temperature of 85°C, corrosion started to be visible to the eye. Wohlgemuth et al. at 2005 also claimed that the corrosion is the most common way of physical degradation mode in solar modules. Many other scientists in the literature proved that the corrosion is the most commonly encountered degradation mode along with the discoloration and the main reason behind this phenomenon is said to be the sodium in the structure of the cell that could interact with the moisture content. [40]

It is also indicated that the faster forms of corrosion could be due to the oxygen between the silicon junctions of the crystalline modules. [41]

Especially in humid and hot geographies, it is even more important to avoid the moisture penetrate into the cell because there happens to be faster diffusion of water

into the ethylene vinyl acetate (EVA) and it could decrease the lifetime of the cell significantly. It is also suggested in the literature that the only way to avoid this faster penetration is sealing the cell by using gaskets with low diffusivity thanks to the big amount of dessicant in them. [38]



**Figure 1-15** Visible corrosion at the edge of the cell

#### **1.2.2.2. Discoloration**

Discoloration results in degradation in Ethylene Vinyl Acetate (EVA) or adhesive material between the glass and the PV cells. It is basically the color change generally to yellow or brown. This change affects the transmitted light into the cell and decreases the module power. [42]

The most effective cause for this kind of EVA degradation is found to be the UV lights with water at high temperatures ( $>50^{\circ}\text{C}$ ). Discoloration could be seen at the different regions of the cell due to the different characteristics of the polymer material. This also proves that the discoloration phenomenon is resulted from the material of encapsulation instead of EVA itself. [43]

In an experimental work, which include artificial radiation exposure of a solar module in order to investigate the UV effects on the degradation (between 280 nm and 380 nm wavelengths) under  $4000 \text{ W/m}^2$ . A very fast degradation in PV cell performance is observed. In addition to that, a discolouring of EVA layer causing PV

performance loss is seen after 400h of exposure time. When the conditions are changed to 1000 W/m<sup>2</sup> and 500 h, the same effects are not seen on the UV region. [44]

Another experimental study shows that for the UV region, the discoloration only occurs under 15 kWh/m<sup>2</sup> global irradiation between the wavelengths of 280 and 385 nm at 60 °C temperature. [45]

Discoloration of the cell has been studied experimentally and it is found that detrimental effect on short-circuit current is around 6-8% for the partial discoloration and up to 13% for the total discoloration. Maximum power of the module is also decreased around 5%. [46] [30] [33]



**Figure 1-16** Discoloured solar cell [47]

### **1.2.2.3. Glass soiling:**

Glass soiling is another physical degradation mode that could be seen by naked eye as a darkening or haziness on the cell surface, mostly on the low edges of PV module. Glass soiling is not the accumulation of dirt on the surface of the module. It is more

related to the particles from air, accumulation of the remains of rain water or the ion exchange between the glass and hydrogen ions in the water. [48]

The glass soiling could worsen under the polluted air conditions along with the use of frames since they could allow some water to accumulate on them. This results in a loss in optical performance (low optical transmittance) of the cell.



**Figure 1-17** Haziness that could be seen at the edge of the cell

#### **1.2.2.4. Delamination**

This degradation mode occurs between the cell and the front glass or encapsulating material. Delamination mainly has two degrading effects. Firstly, it allows light to reflect more and water to penetrate in higher amounts into the cell. [39] Delamination is stated to be more harmful if it occurs at the edges of the module because it could both cause power loss and electrical risks for the whole installation. [49] Delamination problem also occurs more in humid and hot climatic conditions and it could cause metal corrosion problems due to the moisture penetration. It is also claimed that the delamination occurs because of the accumulated salt and penetrated moisture into the cell and the connection between them is formed by the hydrofluoric acid formed by the tin oxide and fluorine both of which are present in the structure of the PV cell. [50]





**Figure 1-18** Delaminated photovoltaic module [47]

#### **1.2.2.4.1. Front- side delamination:**

A white milky color could be observed at the cell perimeter and the interconnection ribbons. This problem is generally caused by the delamination of EVA and is originated by the chemical reaction between anti – reflective coating and additive materials in the encapsulant. The region of the occurrence of this degradation is almost always at the same points namely; around cell busbars and perimeter of the cell mostly due to these places having lower thicknesses than other parts of the module. [51]

#### **1.2.2.4.2. Front grid and AR coating:**

The loss of adhesives between the cell and the encapsulant could cause oxidation and corrosion on anti – reflective layer as well as metallic parts of the cell. The degradation on the AR coating could be observed as a darkening on the central region of the cell due to the oxidation. The darkening starts at the center and moves towards the edges as could be seen in the Figure 1-20 below. Anti-reflective coating is used to decrease the reflectivity of the silicon along with the texturing. At the highest intensity of solar spectrum 600 nm, reflection rate of the silicon is 35%. Texturing and anti-reflective coating (AR) decreases this rate around 23%. [52] Open circuit voltage and short circuit current increase as the rate of reflectivity decreases. This increases the overall power of the cell significantly. AR coatings are transparent

and generally made of oxides. The degradation in AR coatings could result in decreased current, therefore decreased power because it absorbs less photons and could be caused by the inter-diffusion from the contents of the emitter region. Degradation in AR coating could be visibly observed as the brightened color of the cell or by measuring the open circuit voltage and short circuit current. [53]

#### **1.2.2.4.3. Bubbles:**

This mode of degradation has the similarity with the delamination in EVA, but in bubbling the degradation occurs in a smaller area and causes the surface swelling along with the loss of adhesive material as in delamination. The main cause for the bubbles to form is the chemical reactions happening in the cell resulting in gas emission and those gases accumulate in the cell. Bubbles could be formed on the back of the module making it difficult for cells to dissipate the heat on them, therefore resulting in overheating and decreasing their performance and lifetime. Figure 1-19 below shows a monocrystalline PV cell with bubbles formed on the back side. [54]

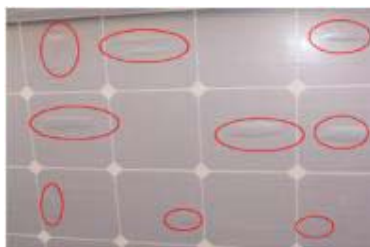


**Figure 1-19** A PV module with bubbles on the back side [39]

Bubbles frequently appear towards the center of the cell because they are mainly caused by the lack of adhesion which is caused by the overheating. If the bubbles are formed on the front side of the cell, they block the radiation absorbed by the cell and causes increased reflection of the light which reduces the power of the cell. [39]



**Figure 1-20** AR coating oxidation through the center of the cell

The reason could be explained with the humidity accumulation since EVA is a copolymer that could allow the diffusion of water vapour and oxygen very easily. Therefore, it also could let the oxidation move around in an easier way. [51]

It is also suggested in the literature that ‘breathable’ parts like edges are less affected by acidic acid because the humidity could escape to the outside of the cell easily in those areas. [55]

#### **1.2.2.5. Breakage and cracking cells**

Breakage of the cell is an important degradation mode. It could occur during the transportation, maintenance or installation of the cell. [45]

Cells could still function for a long time without any problems despite the cracks on them, but there could always be electrical shock and water ingress risks after the breaks occurred. Cell breakage may not be a degradation mode that could drastically decrease the performance of the cell by itself, however it is mostly followed by the corrosion, discoloration and delamination and they could cause severe power cuts. [56]

In order to cut the production costs and raw material saving, PV manufacturers are altering the thickness and the surface of the cell recently. For instance, cell thickness

is reduced under 200  $\mu\text{m}$  from 300  $\mu\text{m}$  and in some cases, it could be manufactured under 100  $\mu\text{m}$ . also, the dimensions of the surface of the cell are increased to 210 mm for both sides. [57] This renewals decreases production cost of the cells, but increases the risk of breaks. Generally, these breaks could not be seen by naked eye unless there is high damage on the module, optical methods are used to detect them.

#### **1.2.2.6. Potential Induced Degradation (PID)**

Cells are connected in series to form modules with the necessary amount of voltage that could reach up to several hundreds. Normally, all the metallic parts in the PV module are grounded in order to avoid electrical shocks, but it is possible to have some leaking electrons from the parts of the module because of the potential difference between the structure and PV module itself and bad insulation between the structure and the layers of the cell. The performance of the PV cell degrades by this inside polarization. This is known as Potential Induced Degradation (PID) and it causes a gradual performance cut in the module in time because of the induced electrical current in the module. [58]



**Figure 1-21** Severely broken glass on a polycrystalline PV module [59]

Experimental works show that PID is more commonly encountered in humid environments too along with the corrosion and discoloration meaning that leaked current increases with the increased humidity. [60]

### 1.2.2.7. Hot spots

This failure mode results in very high temperatures in a small area in the module that could cause damage and performance loss or failure in the module. Hot spots are mainly caused by the failures or mismatch of the cells, shadowing or the problems in the interconnections between the cells of a module. [61] Short circuits cause cells to have negative and reversed value of the actual cell. This leads to a load in the connected cells in series and makes that cell with the defect be more vulnerable for the formation of hot spots. [62]

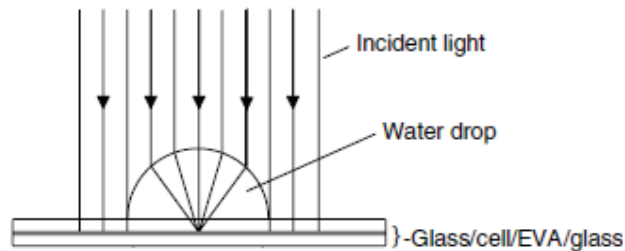


**Figure 1-22 Hot spot formation**

### 1.2.2.8. Mismatched Cells

Many other degradation modes could result in mismatched cells like AR coating degradation, manufacturing defects, cracking or shadowing of the cell, encapsulant deterioration. Cell mismatching is harmful for the cell lifetime and performance because in a series connected cell system, if one of the cells produces lower current than the other cells in the module, other cells act to reverse bias the defected cell. This causes the degraded cell to dissipate power in the mode of heat. Busbars in the cell structure are used to avoid this situation. [63]

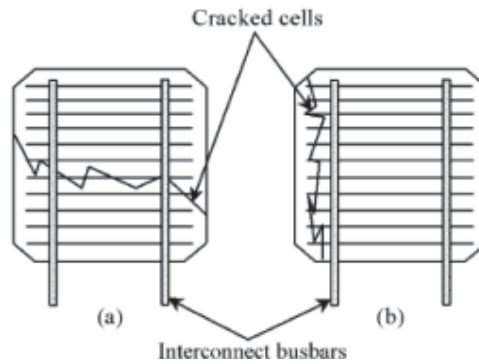


**Figure 1-23** Busbars help prevent the cracked cell producing lower current (a) crack removing the part of the cell from the circuit (b)

High temperatures in the mismatched cells could cause delamination over  $150^{\circ}\text{C}$ . [63] Mismatched cells could cause cell breakdown if the reverse bias rate is higher than the highest voltage that the cell could endure. In addition to that, hot spots on a cell in the module not only decrease the efficiency, but also affects fill factor badly due to lowering the open circuit voltage and short circuit current. Bypass diodes are used to avoid permanent hot spot formation. Mismatched cells could be observed by visual observation, temperature monitoring of the cells and the module or by I-V curve measurements.

#### 1.2.2.9. Temperature Induced Degradation

Power of a PV module at standard test conditions ( $1000 \text{ W/m}^2$  irradiance and  $T_{\text{Cell}} = 25^{\circ}\text{C}$  and Air mass 1.5 global spectrum) is one of the most important specialty. However, when the module is operating at outdoor conditions, 15% of the incident energy could be converted to the electricity. The remaining energy is mainly converted to heat or reflected back from the glass surface or from the cell. Therefore, an average value of the temperature for a module is almost always higher from  $25^{\circ}\text{C}$ . higher temperatures make the bandgap of the cell decrease which allows longer

wavelength photons to be absorbed. Also, minority carrier lifetime increases by this temperature increase and this will give a boost to the short circuit current of the module. On the other hand, this will decrease the saturation current of the module exponentially. [64]

Consequently, open circuit voltage of the cell decreases. Since the decrease of open circuit voltage is exponential, therefore higher than the increase in short circuit current, overall efficiency and fill factor is going to be diminished with the increased temperature. [21]

Statistics show that the physical degradation on crystalline PV cells could be broken down as in the Table 1.4.

**Table 1-4 Physical Degradation Modes Breakdown [65]**

<b>Physical Degradation Mode</b>	<b>Percent (%)</b>
Delamination	42
Corrosion	19
Breaking	19
Discoloration	12
Ribbon Crack	8

**Table 1-5** Thin-film failure modes and mechanisms [66]

<b>Failure Modes</b>	<b>Effect on I-V curve</b>	<b>Possible failure mechanisms</b>
1. Cell Degradation		
a. Main junction: increased recombination	Loss in fill factor, $I_{SC}$ and $V_{OC}$	Diffusion of dopants, impurities etc. Electromigration
b. Back barrier, loss of ohmic contact (CdTe)	Roll-over, cross-over of dark and light I-V, higher $R_{Series}$	Diffusion of dopants, impurities etc. Corrosion, oxidation Electromigration
c. Shunting	$R_{Shunt}$ decreases	Diffusion of metals, impurities etc.
d. Series; ZnO, Al	$R_{Series}$ increases	Corrosion, diffusion
e. De-adhesion $SnO_2$ from soda-lime glass	$I_{SC}$ decreases and $R_{Series}$ increases	Na ion migration to $SnO_2$ /glass interface
f. De-adhesion of back metal contact	$I_{SC}$ decreases	Lamination stresses
2. Module degradation		
Interconnect degradation		
a. Interconnect resistance; ZnO:Al/Mo or Mo, Al interconnect	$R_{Series}$ increases	Corrosion, electromigration
b. Shunting; Mo across isolation scribe	$R_{Shunt}$ decreases	Corrosion, electromigration
Busbar degradation	$R_{Series}$ increases or open circuit	Corrosion, electromigration
Solder joint	$R_{Series}$ increases or open circuit	Fatigue, coarsening (alloy segregation)



**Table 1.5 (cont'd)**

<b>Failure Modes</b>	<b>Effect on I-V curve</b>	<b>Possible failure mechanisms</b>
Encapsulation failure		
a. Delamination	Loss in fill-factor, $I_{SC}$ , and possible open circuit	Surface contamination, UV degradation, hydrolysis of silane/glass bond, warped glass, ‘dinged’ glass edges, thermal expansion mismatch
b. Loss of hermetic seal		
c. Glass breakage		
d. Loss of high-potential isolation		

### **1.2.3. Light Induced Degradation**

This degradation mode is also known as the Staebler – Wronski effect which is a very common problem that is encountered in a-Si cells. [67] When the module is exposed to light, electron hole pairs are produced and recombined. The energy produced during this recombination process could break the weak Si-Si bonds in the structure of the cell causing meta - stable defect sites. These defects deteriorates the PV cell material therefore causes performance cut in the module. [68] Light induced degradation could be observed by periodic measurements of the  $I_{SC}$  and  $V_{OC}$ . [53]

In amorphous silicon technology, light induced degradation could cause ~10 – 30% efficiency loss in the first several hundred hours of light soaking. According to Staebler – Wronski effect (SWE), conductivity (both dark and photoconductivity) of hydrogenated amorphous silicon decreases when it is exposed to light. However, it

could be reversed by annealing over 150 °C. Mechanism of the SWE could be summarized as the recombination – induced breaking of weak Si – Si bonds by optically excited carriers after thermalization resulting in defect centers that lower career lifetime.

Literature has many proposed mechanism for the SWE, however exact mechanism could not still been understood thoroughly. However, it is proven that the SWE is not affected by the impurities. [69] The degradation occurs in the bulk material with a contribution from the surface.[70] The accelerated test of the effect is proven to be possible by using high intensity pulsed light at the standard operating temperature. [71] Effect of the annealing process is explained with hydrogen diffusion.

a – Si shows different performance degradation rates in different seasons generally based on the mean temperature of the day. [72] Studies show that light soaking in warm temperatures also known as warm – soaking (around 50°C) allows higher stabilized efficiencies.

Modules that are installed in regions with higher temperature show have higher efficiencies. [73]

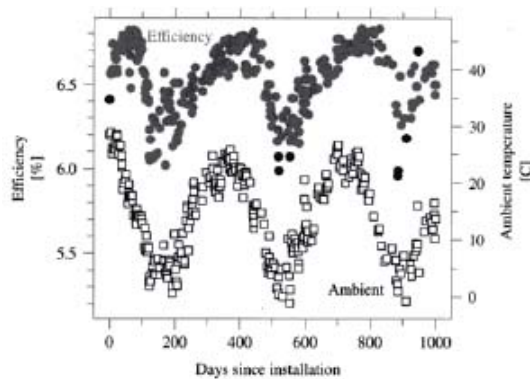


**Figure 1-24** Ambient Temperature Efficiency Relation

This 10 – 15 % change is mainly due to the annealing on the defects caused by SWE. Therefore, temperature is an important parameter for the degradation due to light soaking and the stabilized efficiency of the cell depends on the temperature during light – soaking atmosphere. [74]

Mostly observed degradation mechanisms in other thin film technologies are on CdTe and CIGs cells. In CdTe cells, the degradation is related with the copper in the cell. Since the p – type CdTe could not be contacted with the metal, copper is added to the structure before making the contact. [75] [76] Copper in the structure could affect the electrical properties of CdTe cell dramatically because the copper is very mobile in the structure and it can move to the grain boundaries of the cell to create recombination centers near the p – n junction region. Therefore, even low amounts of copper could decrease the electrical properties of the cell. In addition to that, the electric field causing the applied voltage either external or in the cell could make copper ions move towards the front contact and it is known from the literature from the experiments of the accelerated aging tests that the CdTe degradation is affected by the open – circuit conditions like this. [77] Also, it is known that the impurity diffusion and change in doping material (Cu in this case) could cause instabilities in the performance of the cell. [78] [79]

In CdTe technology, the cell structure could be summarized as TCO /n – CdS / p – CdTe / back – contact . [80] The main problem for CdTe modules is the back sheet metallization and it requires high work function for ohmic contact. Studies show that Te – rich interfacial layer could be beneficial to lower the metallization. [81] [82]

Using Cu is beneficial; however its high diffusivity causes stability problems. Studies show that high temperatures increase the rate of degradation in the cell and the module for CdTe technology. [83] Tests on CdTe cells manufactured with different recipes show no significant difference in efficiency at light soaking. Therefore, it is stated that for the accurate determination of the efficiency, long term test are needed (at least >5000 hours of light soaking). [77]

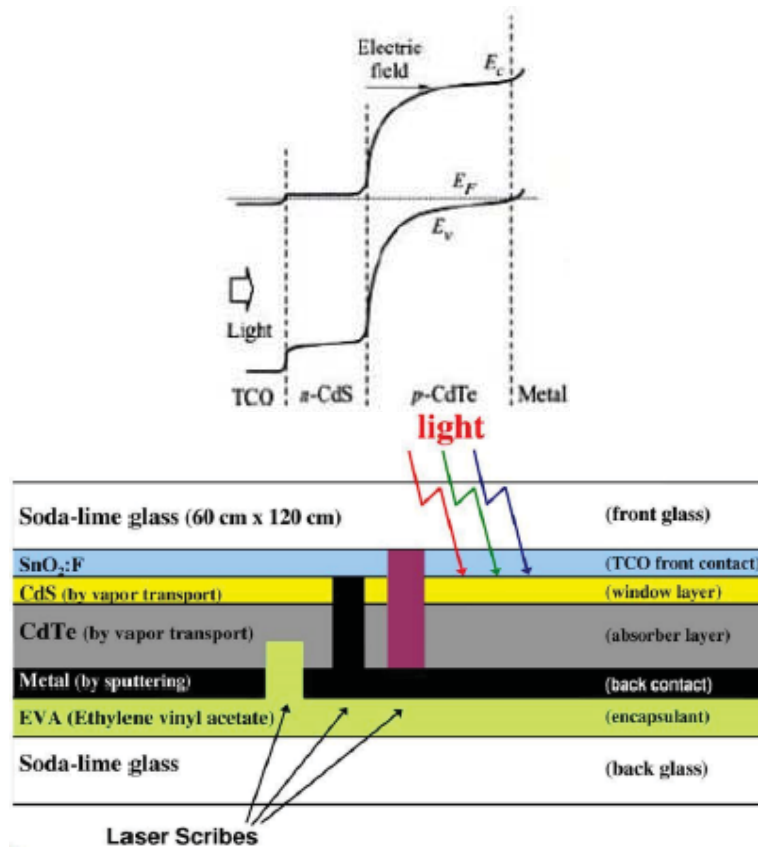


Figure 1-25 Electric Field for the Layers of CdTe Cells

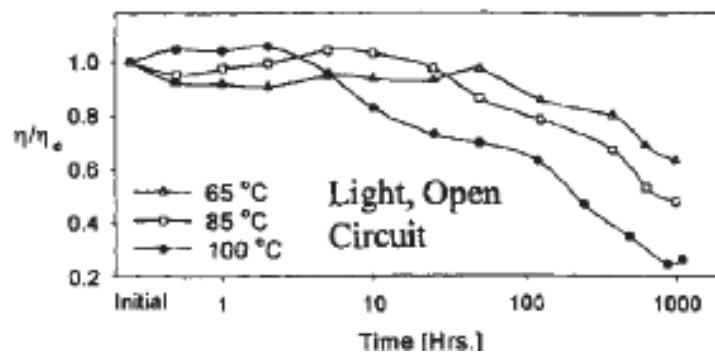
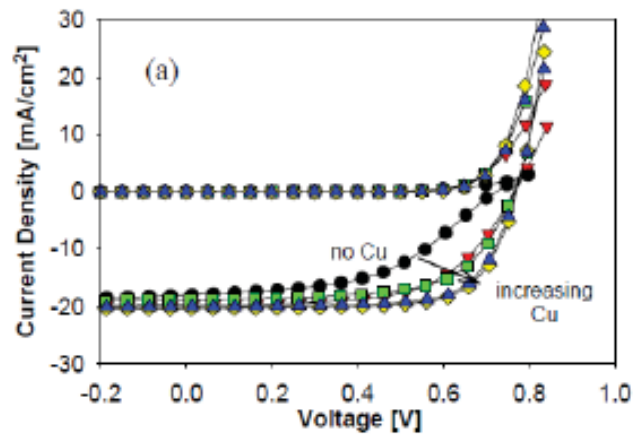


Figure 1-26 Efficiency vs Time at Different Temperatures for a CdTe Cell

Back contact in CdTe technology could create reverse polarization resulting degradation in performance. Cu is added to lower this polarization and increase I and V performance. [84]



**Figure 1-27** Effect of Cu Addition

At high temperatures, Cu at the back side is lost and diffused through the cell and this causes decrease in fill factor of the module.

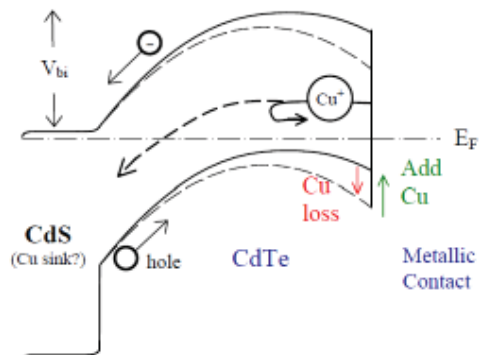


**Figure 1-28** Suggested Mechanism of Cu Diffusion

For CIGS technology, due to its flexible structure, copper is said not to affect the stability of the cells. [85] More importantly, heat tests shows that humidity is a more obvious cause for the performance degradation ( $V_{OC}$  and FF reduction) since it causes an increase in the deep acceptor states concentration in the CIGS absorber. [86]. In CIGS technology, there are two different configurations for the deposition of the cell.

CIGS modules are typically formed in substrate configuration. When they are formed in superstrate form, undesired CdS diffusion could be a problem during the deposition process.

In reversible metastability conditions for CIGS cells, annealing at 80 °C doubling the decrease in the conductivity in dark when compared to the conductivity at room temperature. [87] When the cells are exposed to light, initial state is provided again.  $V_{OC}$  of CIGS cells could shift reversibly with light exposure. Light exposure could increase  $V_{OC}$  by 5% and this effect could be fastened by increasing the temperature. [88]

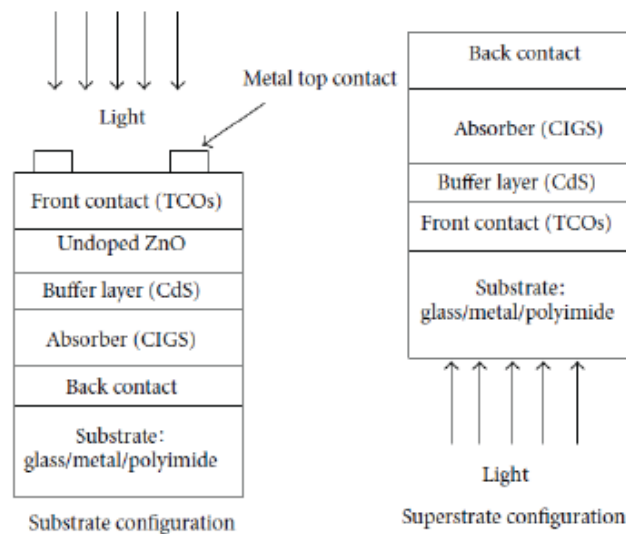


**Figure 1-29** CIGS Cross - Section

Other degradation causes could be categorized as the effect of Ga content on the cell stability and donor type defects. [89] [90] According to the simulation, thinner cells show reduced LID degradation. [91]

### 1.3. Performance Characterization Studies – Outdoor Testing Stations

#### 1.3.1. PV Module I – V Characteristics

A solar cell could be modeled as a single diode with all the internal resistances in the system.

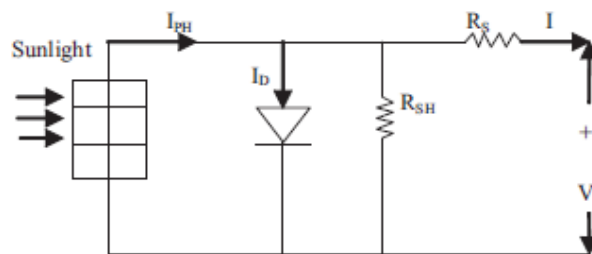


**Figure 1-30** Single diode model of a PV cell

Dark and light I – V curve measurements are made to understand the electrical performances of a solar module. The dark I – V measurements result in:

$$I_D = I_0[\exp(qV / kT) - 1] \quad (1.1)$$

$I_D$  represents the dark current as  $I_0$  is reverse saturation current,  $q$  is the charge of the electron,  $k$  is Boltzmann constant and  $T$  is the temperature.

In illuminated conditions, the characteristic equation for the solar cell becomes:

$$I = I_{PH} - I_0[\exp(qV / kT) - 1] \quad (1.2)$$

$I_{PH}$  represents the current under that the light has produced,  $a$  represents the diode factor.

the above equation is valid for a solar cell, but not for a complete module since a solar module consists of 28 to 36 solar cells connected in series. Therefore, different parameters and variables should be added into these equations in order for solar module to be represented better. [92]

Therefore, the diode approach should be modified. Characteristics of a solar module could be understood in a better way with the equations below:

$$I = I_{PH} - I_D - \frac{V + IR_S}{R_{SH}} \quad (1.3)$$

$$I = I_{PH} - I_0 \exp \frac{q(V + IR_S)}{kT} - 1 - \frac{V + IR_S}{R_{SH}} \quad (1.4)$$

By the help of this equations, the main characteristics of a PV module like short circuit current ( $I_{SC}$ ), open circuit voltage ( $V_{OC}$ ), maximum power ( $P_{MAX}$ ), fill factor (FF) and efficiency are determined.

PV modules are rated with their  $P_{MAX}$  values in the market and this value is found under the standart test conditions abbreviated as STC which is known as testing under  $1000 \text{ W/m}^2$  solar radiation,  $25^\circ\text{C}$  of module temperature and at air mass 1.5g. Determination of this  $P_{MAX}$  value is known as the characterization of the PV module and this procedure is done with the solar simulators. After the characterization, PV module is labeled with the  $V_{OC}$ ,  $I_{SC}$ ,  $V_{MAX}$ ,  $I_{MAX}$  and  $P_{MAX}$ .

However, these STC parameters are not very similar to the real conditions that the solar module will mostly be exposed. The sun will not always provide  $1000 \text{ W/m}^2$  and the module will probably have a temperature of higher than  $25^\circ\text{C}$  because of the weather conditions and outdoor factors. Consequently, a solar module will almost



always perform below the labeled values of power, voltage and current. Therefore, other test conditions are used to have more realistic perspective about the module. These are standard operating conditions (SOC) and nominal operating conditions (NOC). These two approaches use nominal operating cell temperature (NOCT) concept. NOCT is defined as the open circuited cell that is exposed to irradiation of  $800 \text{ W/m}^2$ ,  $20 \text{ }^\circ\text{C}$  and  $1\text{m/s}$  wind speed. Under these parameters, NOCT value is around  $40$  to  $50 \text{ }^\circ\text{C}$ . Three different approaches are tabulated below:

**Table 1-6** STC, SOC and NOC Definitions

Conditions	Standard Test Conditions (STC)	Standard Operating Conditions (SOC)	Nominal Operating Conditions (NOC)
Irradiation ( $\text{W/m}^2$ )	1000	1000	800
Temperature ( $^\circ\text{C}$ )	25	NOCT	NOCT
Wind speed (m/s)	-	1	1

There are various factors that are affecting the performances of the solar modules. Studies show that these factors could be categorized under five subtopics namely the technology of PV module, temperature, irradiation, tilt angle and others.

### **1.3.2. Effect of the type of PV technology**

The main factor that is changing the performance of a PV module in terms of the technology is the efficiency. Mono crystalline PV modules have higher efficiencies (around  $15 - 18\%$ ) compared to the other commercialized technologies such as poly

crystalline and thin film cells, but mono crystalline PV modules are more complicated to produce and causing high costs. On the other hand, poly crystalline modules are easier to produce with a cheaper price and having lower efficiencies around 8 to 12%. [93] [94]

Amorphous silicon cells have efficiencies around 5 – 7% while CdTe and CIS technologies provide efficiencies of 16 and 20%. [95] [96]

Technology creates the basis and the upper limits for the efficiency of the solar module; therefore it is always the major affecting factor.

### **1.3.3. Ambient temperature**

The performance of the module is dependent to its temperature, but the module temperature is also dependent to the ambient temperature. Module temperature is higher than the ambient temperature because the glass frame of the module absorbs the infrared part of the sunlight and encloses the heat. This increase in module temperature decreases the band gap of the cell. [92]

This increases the  $I_{SC}$  of the cell, but decreases  $V_{OC}$  and the decrease in  $V_{OC}$  overcomes the increase and affecting the power negatively. Therefore, the power of the module decreases if the operating temperature of the module increases. Monocrystalline PV cells are affected greater than the other technologies. Studies show that 15 % of a performance cut could be seen on monocrystalline modules as this figure is around 5% in amorphous PV cells. [97]

Increasing temperature decreases efficiency and power to minimum at stagnation temperature and it could also create physical problems like hot spots, degradation in wires or encapsulant. [98]

### **1.3.4. Solar Irradiation**

Solar irradiation has a linear relationship with the power of the module. Higher solar irradiation provides more incident photons for to activate the electrons in the structure of the solar cell meaning more electricity production. However, studies also show that different PV technologies have different responses to increasing irradiation.

For instance; Eikelboom and Jansen states that monocrystalline modules show no power cut under outdoor irradiation. However, CIS and amorphous silicon cells show major degradation in terms of power at STC. The study was made with nine different types of PV modules. The final results also show that thin film technology modules perform better under low irradiation. [99]

### **1.3.5. Tilt Angle**

The performance of a PV module depends on the radiation amount that it is receiving during the day time and this amount is dependent on the tilt angle and orientation of the solar module. [100] [101]

The orientation of the solar module is generally the south for the places in Northern hemisphere and north in the Southern hemisphere. However, tilt angle is dependent on where the module is installed and must be optimized accordingly. There are different methods for optimizing the tilt angle from computational calculations to tracking devices for the best orientation during the daytime. [102]

Each of them differs in terms of the site that PV modules are installed.

### **1.3.6. Others**

Four factors mentioned above have significant effects on performance. However, the variables in the other section are still affecting the power of the module, but in a lower extent. Other factors could be like accumulation of the dust, humidity, wind.

### **1.3.7. Evaluation of the PV Performance**

In order to standardize the quality of PV modules, it is needed to develop some parameters that are universally acceptable and representing the specialties of the modules thoroughly. Therefore, International Electro – technical Commission has developed these mentioned parameters in order to rate and analyze the performances of the solar cells under different operation conditions with different technologies. [103]

These standardized parameters are needed for three main reasons:

- A set of parameter is needed to label and express the modules operating with different technologies and at different geographies, times of the year and designs on the same basis.
- These parameters should also express the losses on the module.
- Decided parameters should also help designers for validating the models for system characterization of a single module or an array of modules.

There are mainly four parameters that could be used for the evaluation of the PV module performance:

#### 1.3.7.1. Final yield (YF)

Final yield defines the ratio of total energy that is produced by the system during a specified time interval to the rated power generation. Rated power generation implies the amount of energy that the system could produce under STC. To formulate:

$$Y_F = E / P_{PV,Rated} \quad (1.5)$$

E stands for the amount of energy that is produced by the system in a specified time interval and  $P_{PV,Rated}$  is for rated power.

#### 1.3.7.2. Reference Yield (YR)

Reference yield is denoted as solar radiation divided by the reference solar radiation. The time interval is the same for the two radiation units.

$$Y_R = H_t / G \quad (1.6)$$

$H_t$ : total solar radiation (kW h/m<sup>2</sup>)

G: reference irradiance (1 kW/m<sup>2</sup>)

### 1.3.7.3. Performance Ratio

Performance ratio is calculated by dividing the final yield to the reference yield. This property is a dimensionless variable that is expressing the normalized performance of the solar module. In addition to that, it gives information about the rate of losses in the module therefore widely used in the long term evaluation of the solar cells. Generally, decreasing values of performance ratio along the years makes it possible to see the degradation rate on the system.

$$PR = \frac{Y_F}{Y_R} \quad (1.7)$$

### 1.3.7.4. PVUSA Rating

PVUSA rating method is used to calculate the performance of the PV module by regressing the meteorological data from the site that the system is located. The data is calculated at the PVUSA Test Conditions (PTC) which are 1000 W/m<sup>2</sup> irradiance, 20°C temperature and wind speed of 1 m/s. In PVUSA, the power output depends on those three variables.

$$P = E A + BxE + CxT_a + DxW_s \quad (1.8)$$

P: the power output in kW

E: amount of irradiance in W/m<sup>2</sup>

T<sub>a</sub>: ambient temperature in °C

W<sub>s</sub>: wind speed in m/s

A & D are the regression data calculated from the experimental data

### 1.3.7.5. Capacity Factor (CF)

Capacity factor is the ratio of the annual power production amount ( $E_{AC,a}$ ) to the full rated power amount of the system ( $P_{PV,rated}$ ) for the same period of time.

$$CF = \frac{E_{AC,a}}{P_{PV,rated} \times 8760} \quad (1.9)$$

### 1.3.7.6. System Efficiency

System efficiency is defined as the produced energy divided by the irradiation amount multiplied with the module area for a specified period of time (a month for the formula below).

$$\eta_{sys,m} = \frac{E_{AC,D}}{H_t \times A_a} \quad (1.10)$$

$\eta_{sys,m}$  stands for the monthly efficiency

$E_{AC,D}$  stands for the energy produced by the system

$H_t$  stands for the amount of irradiance

$A_a$  stands for the module area [104]

### 1.3.8. Outdoor Studies

The outdoor studies aiming to monitor PV technologies over long period of time in order to characterize the performance and degradation modes are listed below:

- In the first study, Ayompe et al. measured the performance of a roof PV system in Ireland, Dublin for eleven months from November 2008 and October 2009. The PV system consists of monocrystalline silicon modules with peak power value of 215 watt each and 17.2% efficiency. Performances of the PV cells are monitored on monthly and yearly basis along with the seasonal variations. The annual final yield value is calculated as 2.4 kWh / kWp-d. [105]

- Work of Emmanuel et al. monitored a PV system on grid with a 171.36 kWp power at Crete, Greece. The PV system is monitored for a year's time starting from 2002 and the power loss modes resulting from temperature, soiling, grid based problems are also calculated in this study. The final yield is reported as between 1.96 and 5.07 h/d and performance ratio is changed around 58 to 73% resulting in an average PR of 67.36%. [106]

- Work of Pietruszko et al. consists of 20 double junction thin film modules with a total power of 1 kWp panels installed at Warsaw, Poland in 2000. The performance of the system is evaluated one year later and the after eight years' operation in 2008. It is indicated that the system provided power value of 830 kWh for the first year's operation which is more than the expected power of the computer simulation in the study. The performance ratio of the system is changing between 0.6 and 0.8 in the first year. For the first three years' operation, performance ratio values are ranging from 0.52 to 0.6, showing a decreasing trend because of the thin film stabilization issue. This work also includes the effects of meteorological parameters and irradiance, temperature and tilt angle with an AC and DC voltage analysis. [107] [108]

- Soa et al. monitored and evaluated the performance of four arrays of 3 kW grid connected PV system consisting of two multicrystalline and two monocrystalline groups. The PV arrays are monitored for one year and the system is also simulated with PVSYST software by using the measured data. Performance ratio values are ranging between 76.8 and 78.1% for third and fourth arrays. However, there is performance loss of 14% because of degradation in the modules and mismatch between sub arrays in first and second arrays even though all are installed in the same way. Final simulation depending on the measured values showed that the whole system performance could be improved up to 13%. [109]

- Sharma and Chandel worked on a PV on grid system of 190 kWp capacity located in India for one year's time. The range or final yield, reference yield and performance ratio are 1.45 – 2.84 kWh/kWp-d, 2.29 – 3.53 kWh/kWp-d, 55 – 83%

respectively. Performance ratio in the average of nine years is found to be 74%. It is also stated in the publication that the tilt angle must be optimized for better power production. [110]

- Makrides et al. established outdoor stations at three different locations Cyprus, Nicosia and Stuttgart. These systems have 13 different kinds of PV technologies with a grid connection and capacity of 1 kWp. Power production values for the Cyprus, Stuttgart and Nicosia are 1600 – 1700, 1194, 1580 kWh/kWp, respectively. Power amount is higher in the system located in Cyprus because of the average irradiance amount of Cyprus is more than Stuttgart and Nicosia. In addition to that, the highest ambient temperature between three locations is at the Cyprus climate (module temperature is around 60°C). This study reveals that the PV modules having a lower maximum power to temperature coefficient ratio ( $P_{MPP} \% / K$ ) are producing higher performances in terms energy production postulating loss of heat from the modules in hot climates as an important parameter on module performance. [111]

- Adhikari et al. tested a 45 moduled system of a total power of 2.88 kWp in a residential place in Bangkok, Thailand. The PV system consists of 4 arrays with a total area of 45.2 m<sup>2</sup>. The system is tested for one year's time between 1998 and 1999 and recorded output power values, efficiency of the system, reference and final yield along with the array yield and performance ratio. Final yield for the system is found to be 1166 kWh/kWp and the highest yield value is found at June as 129 kWh/kWp with the total system efficiency of 5.4%. [112]

- Ruther et al. studied on a 2kWp double junction a – Si building integrated photo voltaic (BIPV) grid connected system in Brazil. Performance ratio of the system is found as 82% for AC and 92% for DC after 5 years of operation. It is indicated in this study that after the evaluation of performance, it is seen that once the stabilization period is over for a – Si solar modules, the performance becomes independent from the operating temperature. Therefore, it is more convenient to use this kind of a system in warm climates for better performance. [113]



Studies above show that there are many parameters like geography, technology, system design, orientation that could differ PV systems and arrays from each other and performance evaluation parameters like performance ratio (PR) or final yield ( $Y_F$ ) are very useful to put them into a common basis for comparison. In addition to that, performance evaluation parameters make it possible to observe the effects of degradation and aging losses numerically. Those measurements and metrics also provide information on which degradation mode (other than time) could be dominant in the system. It is also clear that the PV modules individually should be tracked since they are the most important parts of this integrated systems along with their utilities for power production and degradation modes should be fully understand in order to increase the cell, module and system life and efficiency.

**Table 1-7** Summary of Outdoor Station Findings

Location	Syst. Cap / Type	Technology	Duration	Results
Dublin, Ireland	1.72 kWp / /grid con.	Mono crystalline silicon (m-c Si)	1 Year	PR = 81.5% $Y_F = 2.4$ h/d
Island of Crete, Greece	171.36 kWp/grid con.	Polycrystalline silicon (p - c - Si)	1 Year	PR = 67.36% $Y_F = 1.96$ to 5.07 h/d
Warsaw - Wawer, Poland	1 kWp / grid connected	Double junction amorphous thin film silicon (a-Si)	1 Year and after 8 Years	PR = 80% to
FDTC, South Korea	Four 3 kWp / grid connected	m - c - Si and p - c - Si	1 Year	13% improvement on PV performance
India	190 kWp / grid connected	p - c - Si	1 Year	PR = 74% after 9 years.
Germany	1 kWp / grid connected	m - c - Si p - c - Si a - Si, HIT CdTe, CIS	1 Year	Power Values: 1600 - 1700 kWh/kWp 1194 kWh/kWp 1580 kW/h
Bangkok, Thailand	2.88 kWp / grid connected	a - Si	1 Year	PR = 73% and $Y_F = 3.2$ h/d
Brazil	2 kWp / grid connected	Double junction a - Si	5 Years	PR over 60 months is 82%

#### **1.4. Accelerated Testing in Light Soaking Station**

The main logic behind the accelerated testing for PV modules is the need for quicker data and judgments than the real – time tests. In an outdoor station, the modules are tested every day with periodical data measurements under the real weather conditions for a long time, generally not less than one year because the amount of time is basically needed to see the trends of the equipment for different weather conditions and seasonal effects along with the varying spectral conditions depending on the time for the day. In addition to that, when the physical degradation is the thing to check, it is an important test atmosphere to see if PV modules or cells are durable to the geographical and environmental conditions on a specific area. Also, the indication of the rate of degradation is another subject that provides satisfactory and real data from an outdoor station. Accelerated tests, on the other hand are the simulated atmospheres of the outdoor environments. Devices with the artificial light sources are commonly used to accelerate the light induced degradation on the PV module. These light sources could vary from filtered long arc xenon, fluorescent, metal halide lamps and carbon arc. In some studies, mercury vapor and tungsten lamps could also be used for light soaking testing. Accelerated testing procedure is also named as artificial weathering.

Accelerated testing has some advantages over outdoor real – time operations. For instance; light soaking tests could be continuously conducted under the same conditions without considering the day – night cycles, seasonal variations or change of weather conditions that happen unavoidably in real time testing. The parameters like temperature, humidity or water exposure limits could be pushed over the realistic limits in accelerated tests. For a light soaking station, depending on the power and orientation of the lamps in the system, PV modules could be exposed to energies multiple times more than a PV module would be exposed in a sunny day. The accelerated test environment also provides repeatability and reproducibility in terms of the experimentation and this is not possible in outdoor testing. Therefore, effects of some factors could be observed individually under certain conditions.

Regarding the light sources, each type has its own advantages and drawbacks. Stability of the power that is provided and the resemblance of the light source to the actual sunlight are the most important factors when the quality is concerned.

#### **1.4.1. Xenon Arc Lamps:**

This type of lamps is first developed in 1954 and Xenon arc lamp could simulate sunlight (UV + visible) with the most accuracy among the other lamps. Xenon arc lamps are generally preferred when the test is wanted to be conducted under the natural sunlight conditions. The filtering is done for the change of spectral distribution of the lamp according to the designed experiment. Xenon arc lamps are mainly used in the textile, paint, polymer and automotive industries. Two types of instruments are mostly used with xenon arc lamps. One is air – cooled and the other one is water – cooled devices. The type of cooling does not have much effect on the spectral distribution, but they are important in terms of the design of the device and optical filtering of the light. As all lamps do, xenon lights emit light and heat together while radiating. Therefore, cooling is an important design parameter for the accelerated test stations with xenon arc lamps because the filter, the lamp, the samples that are measured or the other components of the equipment should be protected from overheating, damages or degradation that could be caused by the heat. This is why the two systems are called water cooled and air cooled equipments. Neither of the cooling systems affects the spectral distribution and power amount of the lamps. They are just for the cooling purposes.

Test equipment could have vertical or horizontal platforms for sample placing depending on the need. Large scale equipments have two – tier and three – tier inclined specimen racks in order to provide uniform irradiation distribution. The racks rotate continuously around the xenon arc lamp to establish better uniformity for irradiance, temperature, even humidity.

Xenon lamps have the closest spectral distribution to the natural sunlight in the UV and visible range. On the other hand, in the infrared region it has significant variations. Therefore, the xenon lamp system contains filters that could be designed

according to the test and sample requirements. Generally, water cooled lamps are surrounded by two cylindrical optical filters. In this design, cooling water flow between the inner and outer filters of the cylinder. This provides cooling and elimination of some infrared region radiation since water has the ability to absorb radiation over 1200 nm. In case of a need for more infrared absorption, some additional special filters could be used in this system.

In the air cooled system, one or more xenon lamps are surrounded by flat air filters in both inner and outer region. This time flowing air just filters and cools the system. In order to have the desired spectral distribution for filters, different materials could be used for the inner and outer glasses of the filters. These materials could vary from quartz, borosilicate glass, high borate borosilicate type – s glass, lime glass or coated infrared absorbing quartz (CIRA) for water cooled systems. Spectral distributions of two different commercial xenon lamps are shown below.

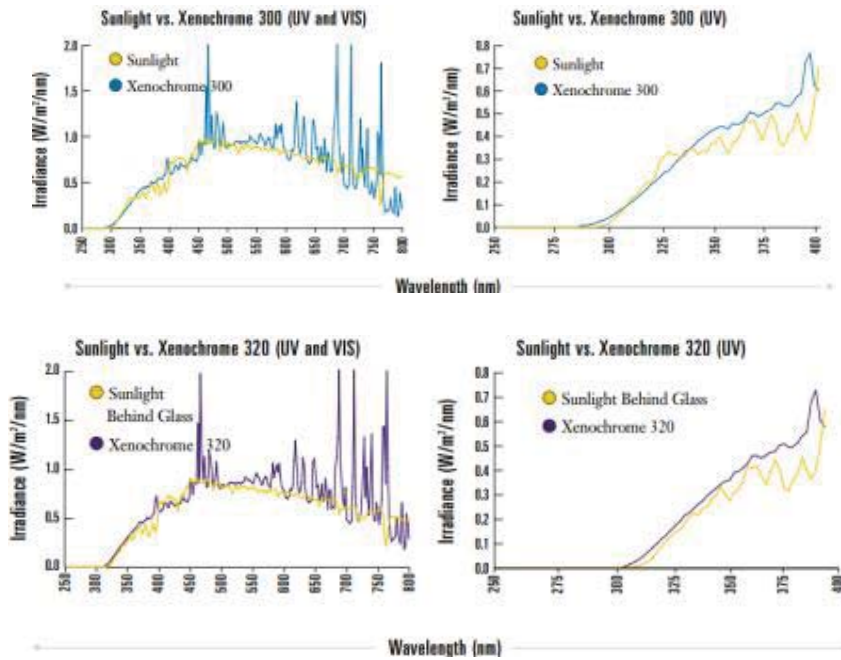


**Figure 1-31** Spectral distribution of a commercial Xenon lamp

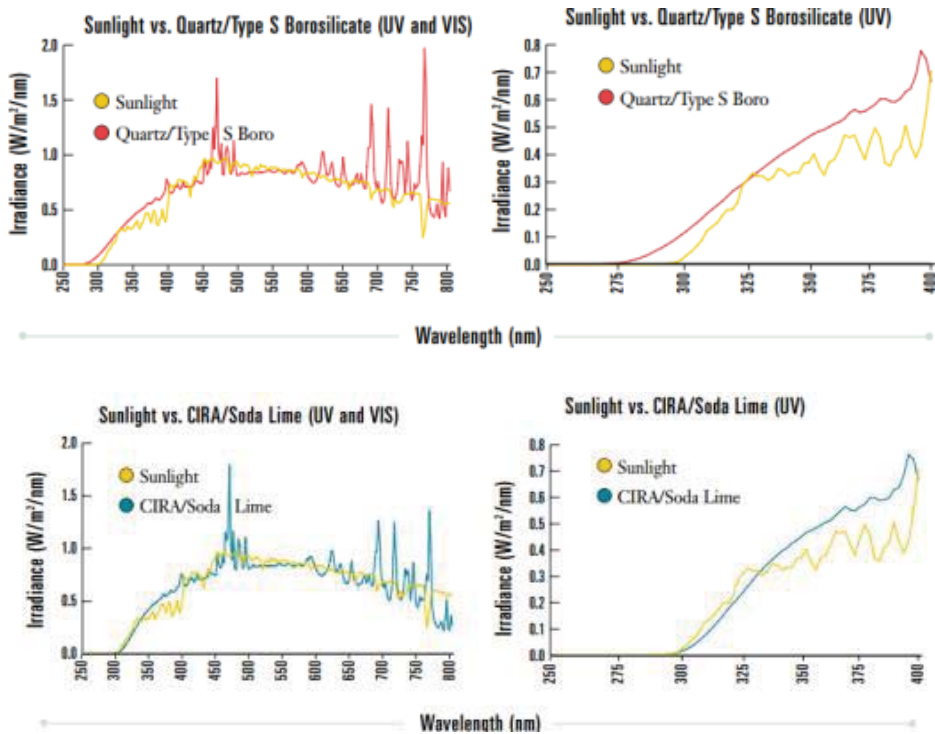


**Figure 1-32** Spectral distributions of a commercial Xenon lamp with different filters

Optical filtering makes it possible to control both spectral distribution and irradiance amount for the lamp. A micro processor helps control radiant exposure. Water cooled xenon lamps usually control the radiation at narrow wavelengths around 340 and 420 nm. Narrow band interference filters are used for this purposes and the power of the lamp is controlled by a wattage and photodetector. On the other hand, air cooled xenon lamp systems usually use broad band UV irradiance which is around 300 to 400 nm.

#### 1.4.2. Fluorescent UV Lamps and Devices:

This kind of lamps have the same physical qualities with the ones that commonly used in residential purposes, but the spectral properties of these lamps are altered to use in light soaking systems. There are different kind of fluorescent UV lamps in

terms of their spectral interval and properties. One of them is fluorescent UV – B lamps having a peak wavelength of 313 nm. Most of the energy of this lamp is maintained between 280 to 360 nm, shorter wavelengths than the natural sunlight. UV – B based test always reports stability values between real and accelerated testing values since there is high amount of short wavelength UV energy and low amount of long UV and visible radiation in UV – B lamps. This changes the light induced degradation mechanism on the samples from outdoor test very much. Secondly, there are fluorescence black lights also known as UV – A type lamps. These lamps have the emission range of 340 – 370 nm and at 340 nm, the irradiance is similar to natural sunlight behavior under 325 nm. Tests using fluorescent lamps are widely used in light soaking practices; however test times are long compared to other technologies and to compare between the UV – A and UV – B type lamps, tests using UV – A lamps even last longer. However, not emitting radiation below the cut – on of natural sunlight improves the correlation with outdoor tests for UV – A lamps. Fluorescent lamps could be useful in terms of the ranking of materials under certain conditions, but it is not very convenient to use them for outdoor test correlation or performance monitoring. They are mostly used in screening tests to identify formulation errors by testing the samples in harsh conditions. A commercial UV – A and UV – B lamp wavelength distribution could be seen below:

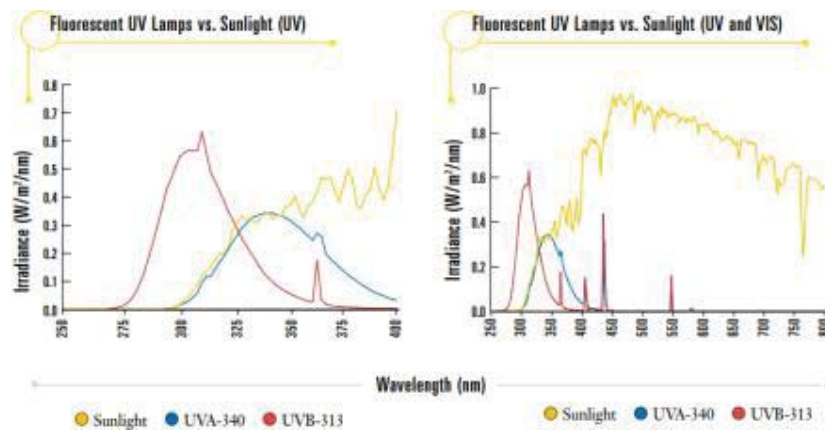


**Figure 1-33** Spectral distribution of UV – A&B lamps and sunlight

Below figure shows how the spectral distribution of a commercial UV – A lamp resembles with the sunlight behind glass at low wavelengths. Green line represents the commercial UV – A lamp while the yellow belongs to the sunlight behind the glass.

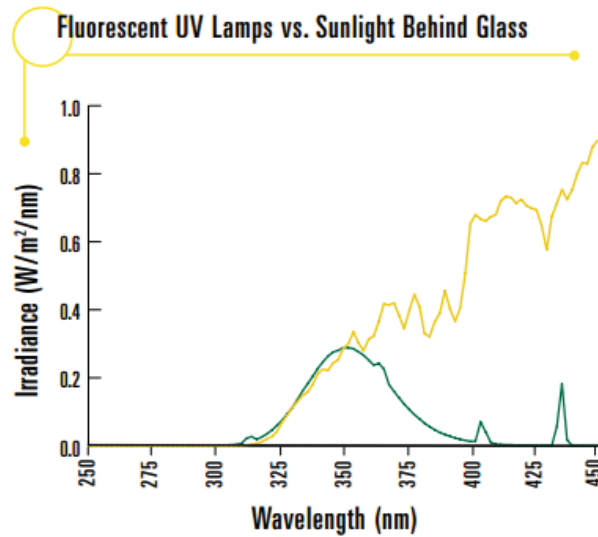


Figure 1-34 UV – A vs Sunlight behind the glass

### 1.4.3. Metal Halide Lamps

Metal halide lamps are known for the full spectrum tests for solar simulators. The most widely used areas are aging tests for both weathering and thermal applications. Metal halide lamps do not have a continuous spectrum. Instead, they are the cumulative of many individual spectrum lights that will provide a total continuum over the wide spectrum. This is due to the rare earth metals like holmium, thulium placed in the arc plasma of the lamp. These metals react with halogens and form halides. Cumulative spectrum of the metal halide lamp resembles very much to the natural sunlight. However, they have to be stabilized and controlled carefully because variations could change this cumulative behavior drastically. Metal halide lamps are known as discharged lamps. They have many different versions, but only



some of them are suitable for solar applications and daylight simulation. The most important characteristics of the metal halide technology are the spectrum resemblance with the natural light, stable irradiance which are very important for a solar system.

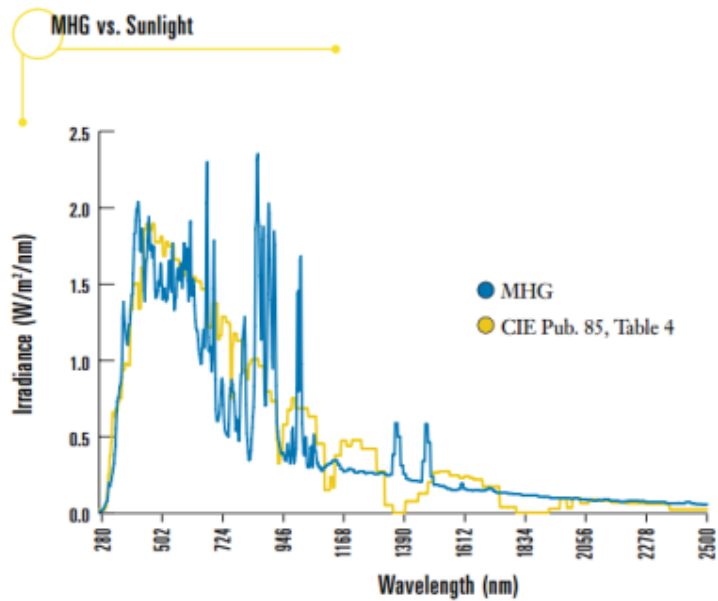


**Figure 1-35** Spectral distribution of a commercial metal halide lamp with the sunlight spectrum



## CHAPTER 2

### EXPERIMENTAL SETUP

The experimental setup in this study aims to establish a test station that can continuously monitor and measure the performance characteristics of installed commercial solar panels and simultaneously measure the outdoor conditions such as ambient temperature, pressure, humidity, wind direction and speed, solar radiation amount along with the solar spectrum of the sun during the day. For this purpose, the test station includes an I-V curve tracer for monitoring the performances of the installed commercial solar modules, an outdoor weather station for the continuous measurements of the weather parameters, mentioned above a solar spectrophotometer for the spectral distribution of the sun and the installed solar modules as they are the interests of all the performance characterization. The weather station and the I – V curve tracer have their own ftp like web servers which could be reached in and out of campus from where internet connection is available in order to store, manage and instantly visualize the data they have been saving during the study. On the other hand, spectrophotometer does not have its own web server, but it is connected to a laptop that can be reached remotely any time and operating for 24 hours for saving the spectral data continuously.

Each equipment in the test station acquires different sets of data with the specified conditions. Weather station collects the weather data such as ambient temperature, pressure, solar radiation amount, humidity, amount of rain and wind speed and direction. These are the values that changes according to the atmospheric conditions during the day and night time. I – V curve tracer collects data from solar modules installed as two different types. The first one is the I – V curves, showing the instant

measurements of performances of the modules with a specified time interval that could be altered according to the measurements that are aimed to be done. Second one is the performance data which shows the overall performances of the solar modules during the day when they are performing at their best also known as peak power mode. Spectrophotometer is also operating all day to collect and save the solar spectrum data continuously with the specified conditions.

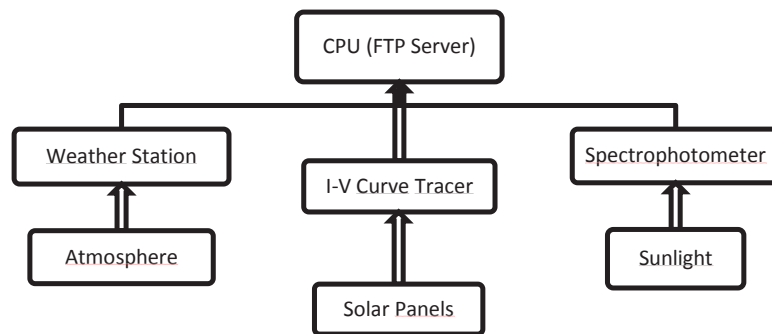


**Figure 2-1** Data Acquisition Flowchart

As it can be seen from the flowchart, all collected data is stored in a computer that can be reached from anywhere inside or outside the campus via file transfer protocol, known as FTP server with an encrypted username and password. Actually, all of the equipments except for the spectrophotometer have its own internal memory. However, in order to keep the data safe from possible memory losses, low memory conditions or unknown errors, data is also saved in different computers and in an external memory that is updated by the new data periodically. Software called Auto FTP Manager makes it possible to acquire the data automatically from internal servers to the computers in desired time intervals with or without leaving the original files in the server according to the selection of the user. Therefore, all the data could be stored in multiple places as soon as they are put into the internal servers. That creates confidence to prevent data from getting lost due to errors, electricity cut offs

or other unknown reasons. To sum up, there are three different kinds of data from I – V curve tracer, weather station and spectrophotometer and these data are gathered in one computer along with the web servers of the equipments themselves.

After giving an overview of the test station and the data acquisition procedure, more detailed information on equipments could be useful for better understanding of the experimental setup.

## **2.1. HOBO U30 Station**

HOBO U30 Station is a tool that makes it possible to gather instantaneous information about weather parameters that could affect the performance and operation of solar modules of all types. Ethernet stands for the method for reaching the internet service of the equipment as HOBO also has GSM and wireless connecting type models. HOBO U20 Station has different sensors that are used for gathering different types of data from the atmosphere. Up to 15 channels of data can be recorded and monitored remotely via web server HOBOLink. The data could be viewed and edited via HOBOLink server specific to the station. The station that is used in this study only has a direct internet connection with an Ethernet cable. 10 smart sensors of any type could be installed to the station in order to measure different parameters. In this study, installed sensors could measure temperature, solar radiation, pressure, humidity, wind speed and direction and the amount of rain.

### **2.1.1. U30 Station Components**

#### **2.1.1.1. HOBO U30 Ethernet Data Logger**

The data logger could be thought as the main board of the station since all the sensor slots and connection tools are inside the logger. It contains 15 channels to connect smart sensors for measurement. The logger has its own battery for power need of the system. This battery could be charged either by solar modules or AC power. There are different slots for both of these energy sources. In addition to that, it has an Ethernet cable slot to reach the HOBOLink server with periodic intervals that is set by the user either by connecting HOBOLink via Internet or to the logger by a USB cable.



Figure 2-2 HOBO Weather Station

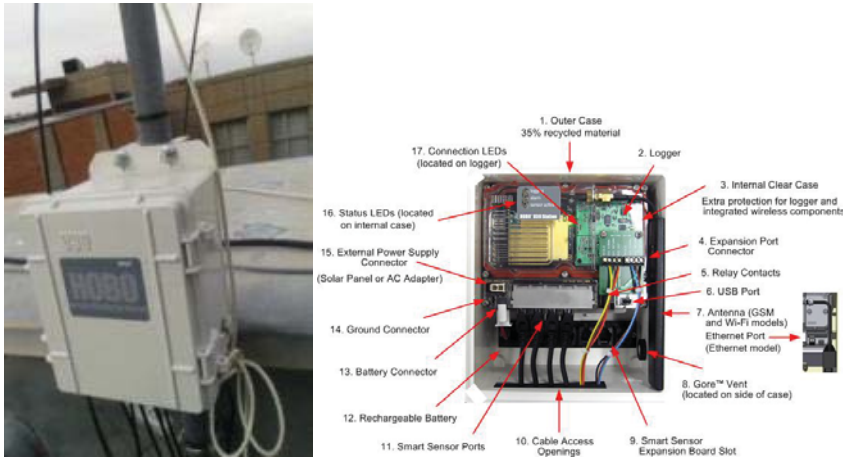


Figure 2-3 HOBO U30 Data Logger

### **2.1.1.2. Solar Radiation Sensor (Silicon Pyranometer) S – LIB – M003**

Solar radiation sensor is a silicon pyranometer designed to take measurements at outdoor conditions. All calibration parameters are stored inside the sensor. Therefore, no additional programming or calibration is needed in order to operate the sensor. Solar radiation sensor and all other measuring devices in this weather station are designed in this manner. Because of this plug and measure specialties, they are called smart sensors. As soon as the sensor is plugged into the slots in the HOBO U30 Data Logger, they start acquiring data for the specified interval and automatically send this data to HOBOLink server.

The silicon pyranometer has a measuring range of 0 – 1280 kW/m<sup>2</sup> over a spectral range of 300 to 1100 nm with a resolution of 1.25 W/m<sup>2</sup>. It can operate in rough outdoor conditions like -40 to 75 °C temperature with an accuracy of ± 10 W/m<sup>2</sup> or ±5%, whichever is greater in sunlight. The small cap (level) that is visible in the figure is used for balancing purposes which makes sure that the pyranometer is taking the sunlight perpendicularly in the specified conditions. After balancing, the level should be removed from the sensor. The silicon pyranometer supports data measurement averaging. When this specialty is used, this means that data is sampled more than it is logged. These sampled values are averaged and the value is stored as the measured value. For instance, if 10 minutes is chosen as the logging interval and 1 minute is chosen for the sampling interval, this means that pyranometer is going to average ten values of samples to store as the measured value. This specialty is useful when decreasing the noise in the data especially when there are fluctuations in the data taken (e.g. a partly cloudy day).

### **2.1.1.3. Rain Gauge Smart Sensor S – RGA – M002**

As all the other smart sensors, rain gauge can also operate as soon as it is plugged into one of the smart sensor slots. It can measure 0 to 12.7 cm per hour with a calibration accuracy of ±1% at up to 20 mm/hour. The rain gauge do not require calibration in the beginning since it is calibrated in the factory before it is used, however it may need an annual calibration by sending to the factory for re – calibration procedure or could also be field calibrated. For field calibration, a known

flow rate is passed through the rain gauge sensor and the results are monitored. It also has an operating temperature of 0 – 50 °C and -40 – 75 °C as survival temperature. The rain gauge is simply a tipping bucket that measures the water amount in the specified time interval. A tipping bucket is basically a funnel that collects the rain drops in a see –saw like container. When a pre – set amount of rain is collected, one arm of the lever tips and as the water pours out from the drain hole in the mechanism, an electrical signal is sent via the other lever. The rain gauge smart sensor measures rainfall by counting the number of tips per recorded measurement, up to 4000 tips per logging interval which corresponds to 40 inches or 80 cm of rain.



**Figure 2-4 Silicon Pyranometer S – LIB – M003**

#### **2.1.1.4. Temperature and Relative Humidity (RH) Smart Sensor (S – THB – M00x)**

All sensor parameters are stored inside the smart sensor, therefore temperature and relative humidity smart sensor does not need any configuration or programming before it is being used. It has a measurement range of -40 °C – 75 °C with an accuracy of  $\pm 0.21^{\circ}\text{C}$  from  $0^{\circ}\text{C}$  to  $50^{\circ}\text{C}$ . This sensor has a resolution of  $0.02^{\circ}\text{C}$  and  $0.1\%$  RH at  $25^{\circ}\text{C}$ . However, if the sensor is exposed to conditions below  $-20^{\circ}\text{C}$  or



above 95% RH, sensor error could increase additional 1%. For best results, the temperature and relative humidity smart sensor is used with a protective enclosure that can be shown in the Figure 6, otherwise exposure to direct solar radiation could increase the errors for the temperature and the relative humidity values significantly.



**Figure 2-5** Rain Gauge Smart Sensor



**Figure 2-6** Temperature and RH Smart Sensor

#### **2.1.1.5. Wind Direction Smart Sensor S – WDA – M003**

Wind direction smart sensor is another plug and play sensor for measuring wind direction data in degrees. Since it needs to be very durable for the wind, it has a stainless steel skeleton with a thin surface. It basically calculates a unit vector average of the wind direction and provides data in degrees. It has a 0 – 355 degrees measurement range (5 degrees dead band) and  $\pm 5$  degrees accuracy and 1.4 degrees resolution. It can be durable up to 54 m/s wind speed and can operate between -40 – 70 °C temperatures. As the method of measurement, unit vector averaging is used since a normal averaging method will provide high error rate. For example, three measurements of 350, 11 and 12 degrees (all winds are from the north) would result in 126 degrees which will indicate southeast direction incorrectly. However, in unit vector averaging the vector components for each measurement are calculated for every three seconds. Then, the direction values are averaged and combined to calculate the average wind direction for the specified logging interval. If the logging interval is lower than 3 seconds, same sensor reading is going to be recorded until a new 3 second average is calculated. For instance, if the sensor is logging at a 1 second interval, the sensor will report the same wind direction (its calculated average) for three samples before calculating and reporting a new value for another three samples.



**Figure 2-7** Wind Direction Smart Sensor

#### **2.1.1.6. Wind Speed Smart Sensor S – WMA – M003**

Wind speed smart sensor could measure wind speed from 0 to 45 m/s. It has a threshold value of 1 m/s and the sensor could endure up to 54 m/s. This sensor is also like the other smart sensors and has its parameters stored in itself and this can automatically communicate to the logger without additional configuration and programming. It has an accuracy of  $\pm 1.1$  m/s with a resolution of 0.38 m/s. Wind speed measurements are averaged over the logging interval or a 3 second timeframe (whichever is greater). If the sensor is set to log faster than 3 seconds, the same sensor reading will be recorded until a new 3 second average is calculated. For instance, for a 1 second logging interval, the sensor would display the same value for 3 seconds before calculating a new value. Gust speed value is the highest three – second wind recorded during the logging interval.



**Figure 2-8** Wind Speed Smart Sensor

#### **2.1.2. HOBOLink**

HOBOLink is web – based software that works with the HOBO Remote Monitoring System. HOBOLink provides services like accessing historical data for each smart sensor or station if there is more than one, setting up alarms for unwanted situations

or controlling purposes and makes it possible to intervene to the station and smart sensors remotely. HOBOLink has a very simple interface that leads the user to the device directly by a main menu supported by the all browsers. It has a username and password login window for the security purposes and alarms for warning the user for unwanted situations like low memory, sensor errors or missed connections.



**Figure 2-9** Wind Speed & Direction Sensor Combined

When username and password information is provided, HOBOLink welcomes the user with the Devices tab which is used for reaching the station that is installed for remote control. Figure 2-10 shows a typical Devices tab screenshot. After the weather station of interest is clicked, the graphs for all the smart sensors' measurements and some other tabs used for configuration can be viewed.



**Figure 2-10** Devices Tab Screenshot



**Figure 2-11** An Overview of Graphs

This screen has different panes and tabs used for different purposes. The graphs of the different smart sensors could be viewed from the graph screen. At upper left side, one can easily view the recent situation of the smart sensors. If there are errors or alarms that are activated, it could be instantly viewed from the upper left area. It is also possible to label the smart sensors as desired.

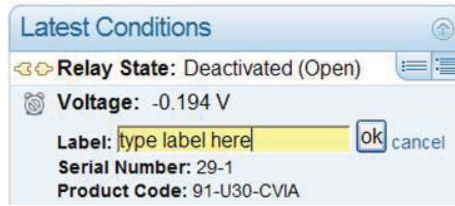


**Figure 2-12** Latest Conditions Pane

At left center, the memory of the logger can be seen. HOBO U30 station stores the weather data in two different forms. One is the .csv format which makes it possible for the softwares like Notepad and MS Excel to view and sort the data directly. The other format is called .dtf which could be only viewed by the software of the HOBO U30 station called HOBOWare. These data files could be directly downloaded by clicking on them.



**Figure 2-13** Latest Data Pane

Between this data pane and the upper left area, there is a pane named Latest Connections. This pane shows the last time the logger is connected to the HOBOLink server.

Below this pane, there is another one called Device Information which shows the status of the logger, its memory conditions and the amount of battery remaining at

the moment of the last connection along with important information like serial number of the device and its nickname at the server.

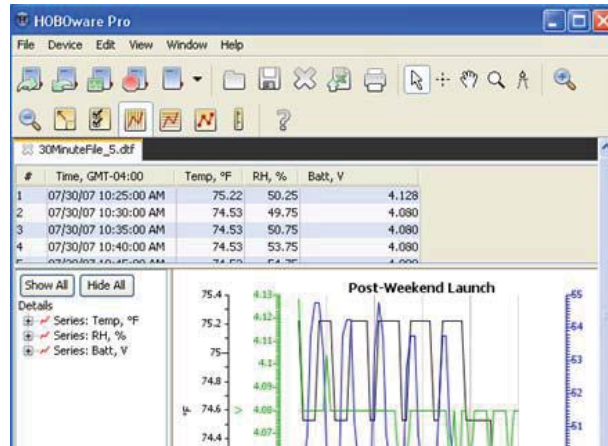


**Figure 2-14** A Sample .dtf File View from HOBOWare



**Figure 2-15** Latest Connections Tab

At the bottom of the page, there are 4 different menus namely Device Configuration, Launch Configuration, Readout Configuration and Go to Alarms.

Device Configuration lets the user change the name of the device and the time zone it belongs to while Launch Configuration lets the user change logging and sampling

interval with some extra features like the option to relaunch the logger every time it connects to HOBOLink.

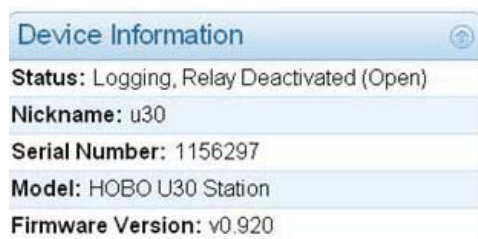


**Figure 2-16** Device Information Pane

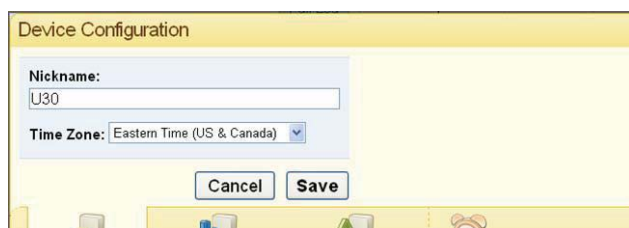


**Figure 2-17** Device Configuration Menu

Readout Configuration mainly lets the user change the connection interval which is the time interval the logger periodically connects and sends the data to the HOBOLink server via Internet. The user can also shift to night mode for low number of connections for the night time to save from battery and memory. Lastly, the option



to save the data as a text file rather along with .dtf files is also present under this menu.

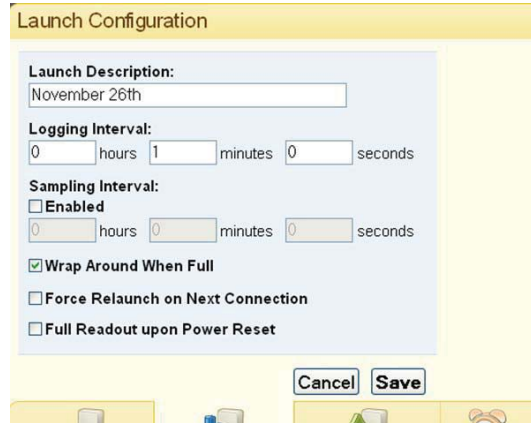


**Figure 2-18** Launch Configuration Menu

Go to Alarms menu is an important one since the user can set alarms for different purposes like missed connections, low battery alerts and sensor failures or for control purposes (e.g. warning the user when solar radiation drops down under some specified value). When an alarm is triggered, an informatory e-mail is automatically sent to the e-mail address specified by the user or additional actions can be conducted, so this makes it possible to intervene an unplanned situation as fast as possible.

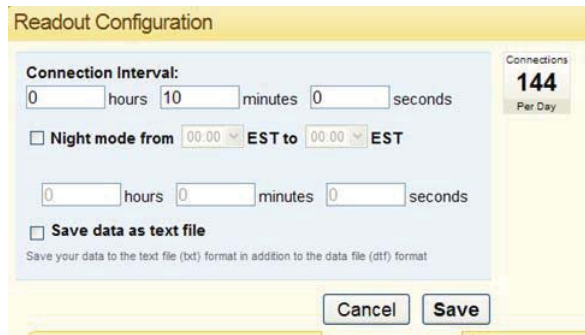


**Figure 2-19** Readout Configuration Menu

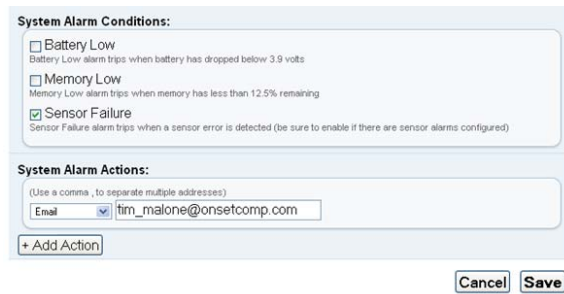


**Figure 2-20** Go to Alarms Menu

Normally, the logger connects HOBOLink in the specified connection intervals during the day (e.g. every 2 hours), but one can manually establish a random connection via USB cable directly from the logger to a PC or laptop. It is also possible to relaunch or readout from the logger manually too. Any change that has been made on the logger via HOBOLink takes place next time it connects to the HOBOLink server. Therefore, it is important to select an optimum connection interval.

## 2.2. Daystar Multi – Tracer

Multi – Tracer is the tool for measuring the performances of the multiple solar modules installed in this station. The multi – tracer has slots for 16 solar modules with different power capacities. Daystar MT5 model is used in this study as the multi – tracer. MT 5 can collect I – V curve data in user defined intervals. It also gives  $I_{SC}$  and  $V_{OC}$  values, however they are never the exactly correct because there are losses due to wiring from PV modules and loads. Therefore, using cables with different lengths or sizes can affect the system to have more or less wiring resistance. Daystar MT 5 is also an Ethernet connected device and it also has its own ftp server with a specific IP address. A separate file is created for each day's data. Average values for all channel and auxiliary input data are stored in this file. The multi – tracer could power track PV modules to within 0.2% of their maximum power.



**Figure 2-21** Daystar MT 5

Daystar MT 5 consists of two different parts. The above part is the control unit and the below part is the load unit. The control unit operates the load unit and has 8

voltage inputs and 24 thermocouple inputs. In fact, Daystar MT 5 is an electronic load that independently controls the operating point and dissipates the power that is produced by PV modules. Load unit provides an electrical load and data acquisition and has 16 slots for PV modules with different peak powers. The multi – tracer dissipate the power that is produced by PV modules as heat and needs to be in a place that is very well cooled or ventilated. Therefore, it is placed in a box that is specifically designed with fans in itself for cooling purposes. Fans of the system can reach up to a very loud noise, so it is kept in a closed enclosure to reduce the noise.

The MT5 collects two types of data:

- Continuous performance under load
- I – V curves

These data is stored within the internal memory of the multi – tracer. These data files are accessible through the ftp server of the device. Since the equipment is working under a big electrical load, grounding is a very important issue. For this study, the multi – tracer is grounded with an available grounding wire in order to prevent high electrical loads.



**Figure 2-22** Load and Control Units of Daystar MT5

MT 5 system is designed for starting measurements automatically. However, there are many different customizations that could be done via web server. Web server has a simplistic design showing module power parameters, temperature values if any thermocouple is installed and other auxiliaries' values (e.g.pyranometers) on main page.

The system continuously collects performances of PV modules under load conditions and it also collects I – V curves at specified intervals. Therefore, averaging interval under the settings menu is an important parameter to set because it specifies how much time the device will wait before averaging the data. For example, if this value is 10 minutes, then the MT5 is going to average data for 10 minutes before writing these average values to the data file.

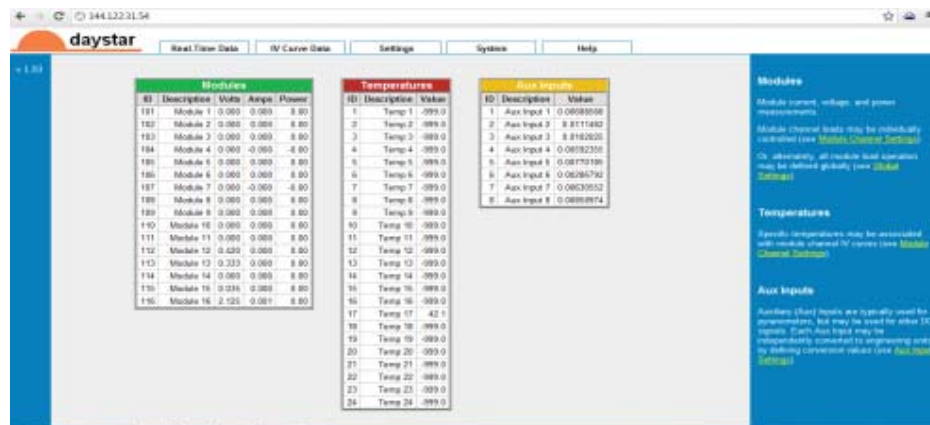
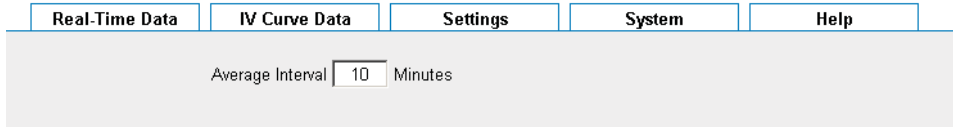


Figure 2-23 Web Server for MT5



**Figure 2-24** Settings Menu and Average Interval

These data are stored as the Multi Tracer Data (.mtd). This is a text file containing all the performance data in tab – delimited form. The MT5 automatically creates a new file for every day and automatically stores the new data on this newly created file. Another important setting is the load configuration. Each PV module load operates independently. There are three different load modes:

- Off mode
- Peak power track
- Fixed voltage

In this study, peak power track mode is used. In this mode, the MT5 changes the load in order for the PV module to operate near its peak power value. Each module could be set to operate at peak power mode or from the global tab under the settings menu; all modules could be set to work on peak power mode too.



**Figure 2-25** Peak Power Setting

Second data type is the I – V curve data. I – V curve trace could also be tracked one by one or for all modules at once as the performance data. From the settings menu, the time interval for the I – V curves could be arranged. Each I – V curve is stored under an .xml file. With the label showing the time and date with the module label or slot number. Both data files (.mtd & .xml) are stored in the ftp server and could be reached and downloaded with the username and password defined by the user. Those files are either viewed by the software provided with the MT5 (IVPC 3) or with a software like MS Excel.

### Index of /





Name	Size	Date Modified
 curves/		8/5/13 5:00:00 PM
 lost+found/		10/17/11 12:00:00 AM
 mounted	0 B	10/17/11 12:00:00 AM
 mtd/		8/5/13 9:00:00 PM

Figure 2-26 FTP Server Screen for MT – 5

































Index of /curves/			Index of /mtd/		
Name	Size	Date Modified	Name	Size	Date Modified
 [parent directory]			 [parent directory]		
 101_12022011_164446.xml	12.4 kB	12/2/11 12:00:00 AM	 mt06122013.mtd	63.5 kB	6/12/13 8:50:00 PM
 101_12062011_101626.xml	24.2 kB	12/6/11 12:00:00 AM	 mt06132013.mtd	157 kB	6/13/13 8:50:00 PM
 101_12062011_101726.xml	24.0 kB	12/6/11 12:00:00 AM	 mt06142013.mtd	157 kB	6/14/13 8:50:00 PM
 101_12062011_102843.xml	24.1 kB	12/6/11 12:00:00 AM	 mt06152013.mtd	157 kB	6/15/13 8:50:00 PM
 101_12062011_102932.xml	23.7 kB	12/6/11 12:00:00 AM	 mt06162013.mtd	157 kB	6/16/13 8:50:00 PM
 101_12062011_103028.xml	23.8 kB	12/6/11 12:00:00 AM	 mt06172013.mtd	157 kB	6/17/13 8:50:00 PM
 101_12062011_103319.xml	24.2 kB	12/6/11 12:00:00 AM	 mt06182013.mtd	157 kB	6/18/13 8:50:00 PM
 107_01022013_160001.xml	23.1 kB	1/2/13 12:00:00 AM	 mt06192013.mtd	157 kB	6/19/13 8:50:00 PM
 107_01032013_080001.xml	21.2 kB	1/3/13 12:00:00 AM	 mt06202013.mtd	157 kB	6/20/13 8:50:00 PM
 107_01032013_100001.xml	23.0 kB	1/3/13 12:00:00 AM	 mt06212013.mtd	157 kB	6/21/13 8:50:00 PM
 107_01032013_120001.xml	23.1 kB	1/3/13 12:00:00 AM	 mt06222013.mtd	157 kB	6/22/13 8:50:00 PM
 107_01032013_140001.xml	23.2 kB	1/3/13 12:00:00 AM	 mt06232013.mtd	157 kB	6/23/13 8:50:00 PM
 107_01032013_160001.xml	22.9 kB	1/3/13 12:00:00 AM	 mt06242013.mtd	157 kB	6/24/13 8:50:00 PM
 107_01042013_080001.xml	19.8 kB	1/4/13 12:00:00 AM	 mt06252013.mtd	157 kB	6/25/13 8:50:00 PM
 107_01042013_100001.xml	23.1 kB	1/4/13 12:00:00 AM	 mt06262013.mtd	157 kB	6/26/13 8:50:00 PM

Figure 2-27 Index of .mtd and .xml Files

### 2.3. StellarNet Blue – Wave Spectrometer

StellarNet Blue – Wave Spectrometer is a fiber optic coupled instrument that is used in order to measure the spectral distribution of the sunlight continuously. Unlike the other equipments in this system, StellarNet Blue – Wave Spectrometer does not have a direct web server to store data or reach the equipment remotely. However, it could do continuous data storing in the episodic data capture mode when connected to a laptop or PC. It has a mode called episodic data capture which makes it possible to store the spectral distribution in the range of 200 – 1150 nm continuously or in a user defined time interval.



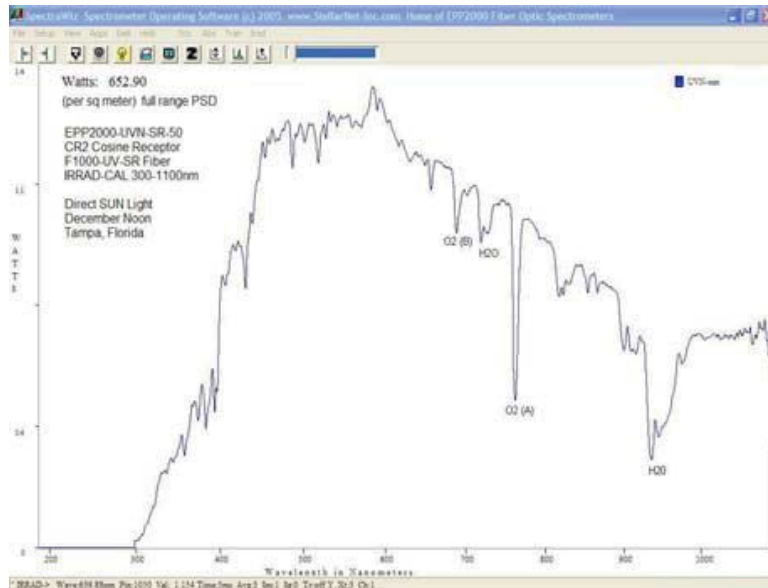
Figure 2-28 StellarNet Blue -Wave Spectrometer



Figure 2-29 Screenshot from SpectraWiz. Episodic Data Capture with Two Different Spectrometers



In this study, Team Viewer software is used to reach the laptop that is working to store the data for spectrometer remotely. StellarNet Blue – Wave Spectrometer could be connected via USB to a PC or a laptop. SpectraWiz is the name of the software that is used for operating the spectrophotometer.



**Figure 2-30** UVN Spectra of Sunlight

SpectraWiz shows the episode number at upper right and the value for the x and y axis in the upper left. In continuous mode, spectrometer could get real –time measurements with user defined integration time and resolution. Data stored could be viewed and edited in MS Excel via the help of a small software package named as SwDemo. This software converts the SpectraWiz files into xml files. Different integration time and resolution trials give interesting results about the spectral distribution and its visualization. This equipment is also planning to be used for the

calibration of the lamps that are going to be used for the designed light soaking station.

#### **2.4. FTP Server**

There are three main sources for the data in this system. The first one is coming from HOBO weather station, secondly Daystar MT – 5 collects and stores solar module performance data on its memory and over its built – in web server and solar spectrum data is directly connected to a computer to save the data continuously which is not a very well working system for it since the equipment is more suitable for short length data collection in laboratory. However, data from those three sources are gathered and stored in a main computer and that computer is also designed as an FTP server which means that the data could be reachable from anywhere via Internet connection when the username and password information are known. Therefore, this system enables all sources of data to be stored in one place and works as a live server that is updated continuously. Future work of this study includes an establishment of an automated daily, monthly or yearly report generating algorithm on this server to make the visualization and analysis of performance, weather and spectral data easier and more efficient. This reports is planning to be visible on a specific domain on the Internet to be reached from anywhere with the connection for data analysis and observation purposes. ftp://144.122.31.53 is the URL of the web server for the data. When the URL is entered to any web browser, username and password screen is welcoming the user for authentication. After logging in the server with the username and password, the user could view, change or download the data stored in the server.

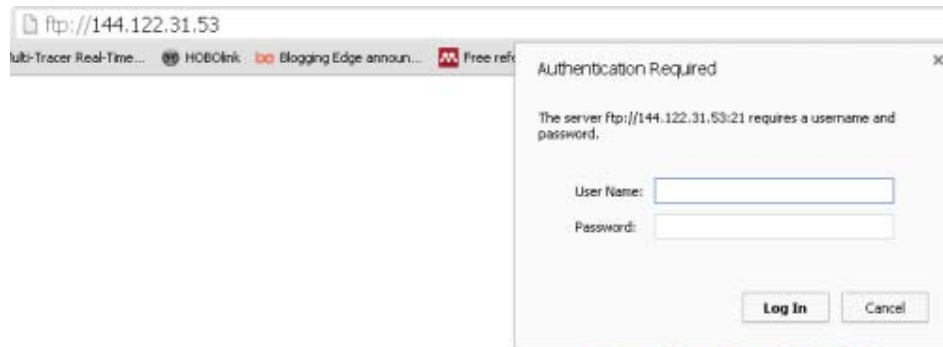


**Figure 2-31** Entrance Screen for FTP Server

All data tagged according to the date could be found under the folders of the server.



**Figure 2-32** Datascreen in the FTP Server

Name	Size	Date Modified
[parent directory]		
Every_Minute_2014_01_31_12_53_26.UTC.xlsx	4.0 kB	1/31/14 2:54:00 PM
Every_Minute_2014_01_31_13_03_26.UTC.xlsx	4.0 kB	1/31/14 3:03:00 PM
Every_Minute_2014_01_31_13_13_26.UTC.xlsx	4.0 kB	1/31/14 3:13:00 PM
Every_Minute_2014_01_31_13_23_26.UTC.xlsx	4.0 kB	1/31/14 3:23:00 PM

**Figure 2-33** HOBO Folder and Files

### 2.5. Solar Module List and Justifications

There are 9 solar modules that are installed in our test station. All of them are labeled and connected to the Daystar MT – 5 I – V curve tracer for the daily performance and I – V curve measurements.

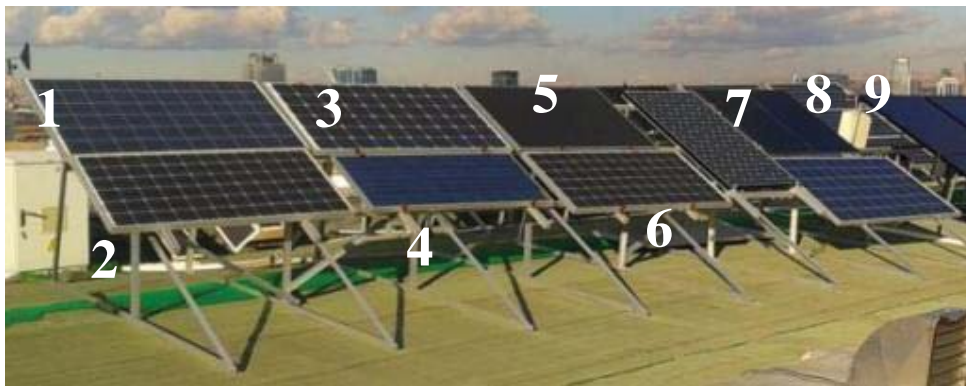


**Figure 2-34** All panels in the station



**Figure 2-35** Daystar MT – 5 load (below) and control unit (top)

Nomenclatures of the tables are listed below;

$P_{MAX}$ : Maximum Power

$I_{MP}$ : Current at Maximum Power Point

$V_{MP}$ : Voltage at Maximum Power Point

$I_{SC}$ : Short Circuit Current

$V_{OC}$ : Open Circuit Voltage

### **2.5.1. Solar Modules List**

Solar modules list is shown in Table 2-1.

**Table 2-1** List of Installed Solar Modules

<b>Brand</b>	<b>Tech.</b>	<b>P<sub>MAX</sub></b> <b>(W)</b>	<b>I<sub>MP</sub></b> <b>(A)</b>	<b>V<sub>MP</sub></b> <b>(V)</b>	<b>I<sub>SC</sub></b> <b>(A)</b>	<b>V<sub>OC</sub></b> <b>(V)</b>	<b>T Coeff.</b> <b>P<sub>max</sub></b> <b>(%/°K)</b>	<b>T Coeff.</b> <b>V<sub>oc</sub></b> <b>(%/°K)</b>	<b>T Coeff.</b> <b>I<sub>sc</sub></b> <b>(%/°K)</b>	<b>#</b> <b>of</b> <b>Cells</b>
Chiner New Energy CR 240	Polycrystal Silicon	240	7.96	30.2	8.7	36.6	-0.55	-0.36	0.03	60
Chiner New Energy CR 160	Monocrystal Silicon	160	4.58	35	5.06	43.7	-0.55	-0.36	0.03	72
Isofotón ISF – 240	Monocrystal Silicon	240	7.94	30.3	8.45	37.1	-0.464	-0.323	0.042	60
SolarA S520P36 (SM520S)	Polycrystal Silicon	130	7.3	17.8	8.18	21.7	-0.45	-0.36	0.025	36
Sharp NA – F128G5	A.Thin Film Silicon	128	2.82	45.4	3.45	59.8	-0.24	-0.3	0.07	180
Chiner New Energy CR 160	Monocrystal Silicon	160	4.58	35	5.06	43.7	-0.55	-0.36	0.03	72
Sanyo HIP – 230 HDE1	Monocrystal HIT	230	6.71	34.3	7.22	42.3	-0.3	-0.25	0.03	60

## CHAPTER 3

### LIGHT SOAKING STATION DESIGN

#### 3.1. Overview of the Design

In addition to building an outdoor panel testing facility, a secondary purpose of this project is to put together a light soaking station in which panels can be tested and characterized under controlled conditions. By comparing the performance and degradation behaviour of the panels on the outdoor test station vs. the light soaking station, one can put together protocols for accelerated testing of panels – thereby reducing the time taken to characterize the stabilized or long term efficiency of produced panels.

The design of our light soaking station needs to satisfy cost vs. performance constraints. On the one hand, we need to deliver a solar spectrum and intensity that is as close to solar radiation as possible on a relatively large area (at least 1m by 1m) while keeping costs to a minimum level. Our design is based upon the patent named “Light Soaking System and Test Method for Solar Cells” [114]. Numbers on the figures are the component codes in the related patent.

#### 3.2. Choice of the Light Source

The first decision that needs to be made in the design is to choose the type of light source. Xe arc lamps are the most suitable choice as far as the solar spectrum is concerned. As shown in Figure 3-3, the spectral distribution from these types of lamps show a good overlap to the solar spectra as measured on the surface of the earth. The match can be made even better when specific filters are used to filter out some of the unmatched peaks. However this is a very expensive solution for our

application. A 1000W Xe arc lamp can easily cost above \$1000, let alone any equipment to filter out the undesired peaks.

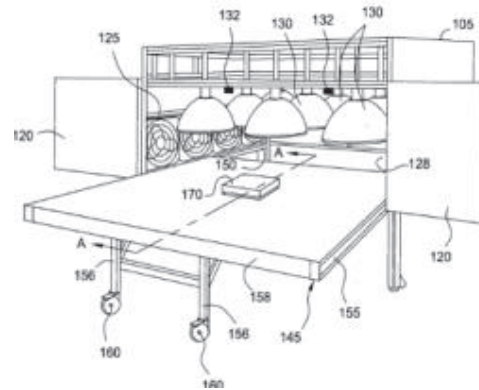


**Figure 3-1** The patented light soaking design [114]

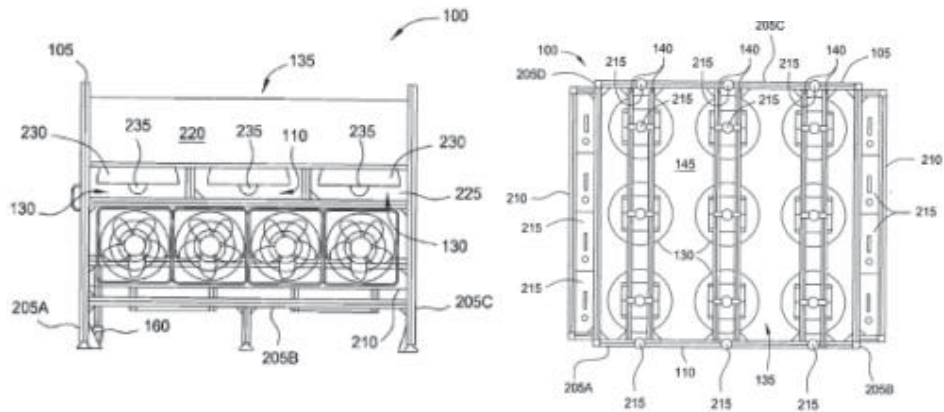


**Figure 3-2** Side and Top view of LID Station



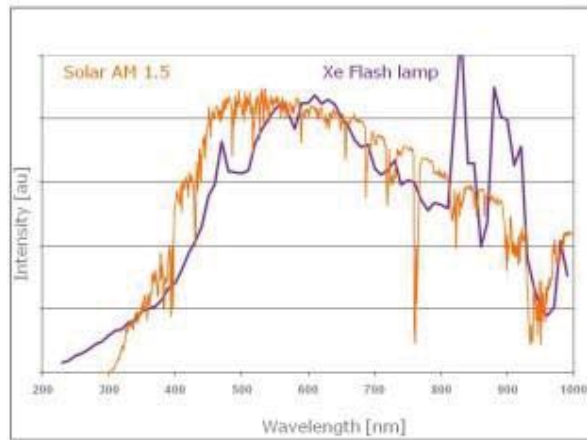


**Figure 3-3** Spectral Distribution for Xe Flash Lamp [115]

The next light source type that can be considered are Metal-halide lamps. The spectral distribution of this type of light source is shown in Figure 3-4. As one can see, the distribution contains multiple peaks that are not present in natural sunlight. On the cost side however, there is an order of magnitude decrease, where a 1000W metal-halide lamp, including the housing and related starter electronics costs around \$100. In fact metal halide lamps are what are used frequently in stadium and street lighting.

Since we envision using 9 of these 1000W light sources for our station's design – the light source costs would be around \$10000 for the better matched Xe-arc lamps and around \$1000 for the cheaper metal-halide light sources. This is the justification for the use of metal-halide lamps.

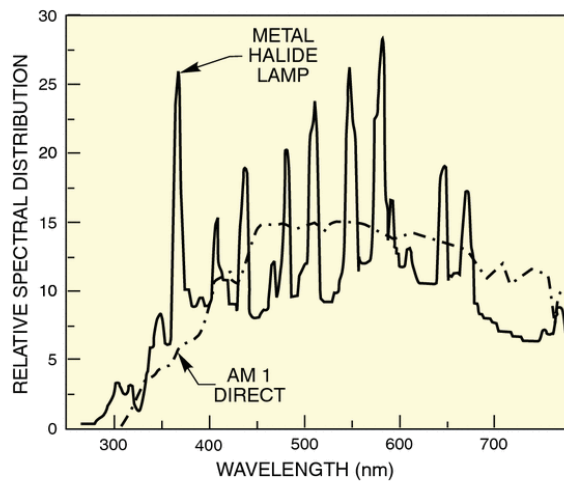


**Figure 3-4** Spectral Distribution of a Metal Halide Lamp [116]

### 3.3. Choice of Instrumentation

In addition to aging the panels under the light, the light soaking station also needs to have the capability to monitor panel performance as well as ambient conditions. This functionality can be delivered by a piece of equipment that is similar to the DayStar Multi-tracer which was utilized in the outdoor test station. However with a cost of around \$50000, this highly capable option is again out of reach due to cost constraints.

Instead, we propose to deliver the same capability using modules supplied by National Instruments combined by a PC and LabView software. The main module in such a set-up is a 4 quadrant power supply that will enable light and dark IV measurements, namely a NI PXI-4130. This power supply can deliver -20 to +20V with a maximum current of 2A. This range can be extended by using multiple NI PXI-4130 modules if needed. This power supply is coupled to a NI PXI-2527, a high voltage multiplexer module that is capable of switching a single input to 16 outputs.

This combination allows for NI PXI-4130 to be used to capture IV curves for 16 panels – the measurements cannot be simultaneous but rather successive. The environmental conditions can be monitored through a NI PXI-6220, which is a high speed analog input module. A total of 16 channels can be connected to this analog input module which can include panel or ambient temperatures through thermocouples or other suitable temperature sensors as well as light intensity through standard cells or pyranometers. These three modules are enclosed in a NI PXIe-1073 chassis and connected to the PC through a PCI-express interface. This set-up is pictured in Figure 3-5.



**Figure 3-5** Picture of the Chassis with the cards installed

The PC used is an HP brand machine with an Intel I3 family processor with 8GB of RAM and a 500GB hard-disk. Combined with an academic license for LabVIEW 10 software, the total cost of the monitoring system is around \$12000. The LabVIEW code has been put together in house.

### **3.4. Lamp Configuration and Station Housing Design**

Once the aforementioned choices are made, the next problem to be addressed is how to configure the multiple light sources and how to design the enclosure and auxiliary equipment to deliver as uniform intensity as possible with controlled ambient conditions. The most significant issue to address besides light intensity distribution is

the temperature of the panels that are being aged. The multiple 1000W sources will be delivering a significant thermal energy to the station and if not removed, the panel temperatures will increase beyond limits that are appropriate for characterization purposes. The cooling in the system will be achieved by using 10 fans that are 20cm in diameter. These will be arranged in a very similar fashion to what is used to cool computer cases – that is one set of fans will be drawing in air from the outside and a second set will be exhausting from the opposite side. This will provide for a fresh air circulation within the enclosure and by positioning the panels in this air flow, convective cooling will cause the panel temperatures to be maintained at appropriate levels, despite radiative heating from the light sources. If this approach fails to deliver enough cooling, the next option is to equip the panel holding plate with an active cooling mechanism that should also deliver a conductive cooling mechanism to the panels. This will require an additional temperature controlled bath and a recirculating pump. However this would also provide the capability to actively adjust panel temperatures during testing.

The light source configuration was decided and characterized in two steps. We begin by characterizing the distribution from a single light source. Then we use this set of measurements as the basis of a model that evaluates the additive light from multiple sources. Based on the results of this model, we finalize our housing design – incorporating a mechanism for adjusting the light source to panel distance. This adjustable distance will be fine-tuned upon construction of the equipment as the model predictions may not be perfect. Furthermore being able to adjust the separation will let us run aging tests at intensity conditions that are higher or lower than the standard  $1000\text{W}/\text{m}^2$  as well as allowing us to bring the panels closer slightly as the light bulbs age over time. These activities will be summarized in the upcoming sections.

### 3.4.1. Single Light Source Characterization

We chose to use 1000W light sources from the GE company – along with the bulb housing and required starter components. These are pictured in Figure 3-6.

As one can see – this is the type of light source that is used to light sport fields and parking lots. The light source itself is actually a very small – in the shape of a cylinder that is approximately 10mm long with a diameter of around 3-5mm. The reflector is in the shape of a rectangle with 365x393mm. The reflector edges are at an angle of 30° on the long edge and 23° on the short edge. Due to this asymmetry, one needs to make a choice on how to orient the multiple lamps to deliver an intensity distribution that is as uniform as possible.



**Figure 3-6** Picture of the single light source and the starter

We chose to characterize the distributions from the light source at distances of 50cm, 100cm, 150cm and 200cm. Due to the angles of the edges, the light intensity drops very sharply to zero when one moves outside of the zone of direct exposure to the source. Therefore the spacing of the grid needed to be adjusted according to the distance to the light source in order to be able to characterize the lamp as accurately as possible for the subsequent modeling activity. This is reflected in the grid definition appearing in

Figure 3-7 below. Light intensity are measured by a KIMO SL 100 Solarimeter – which utilizes a standard polycrystalline reference cell for capturing the light intensity [117]

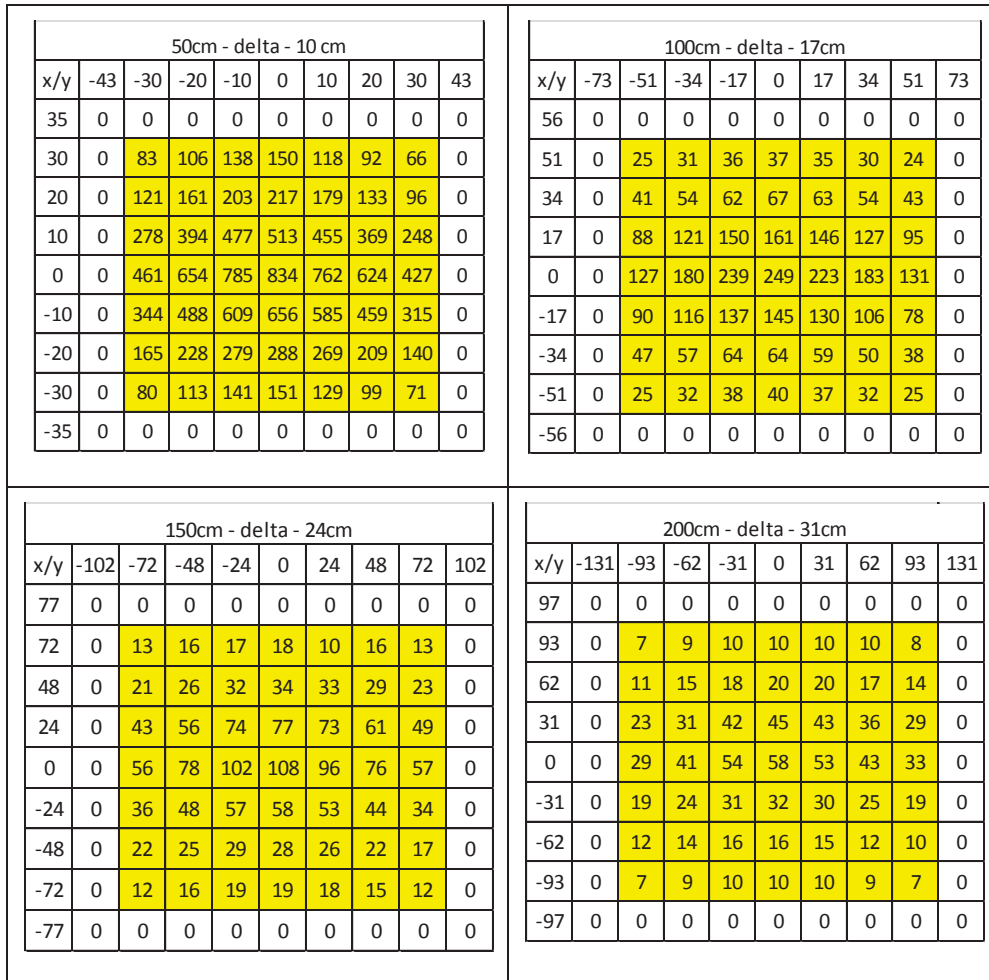


**Figure 3-7** Single light source intensity distributions - intensity measurements are in terms of  $w/m^2$  and grid data are in terms of cm.

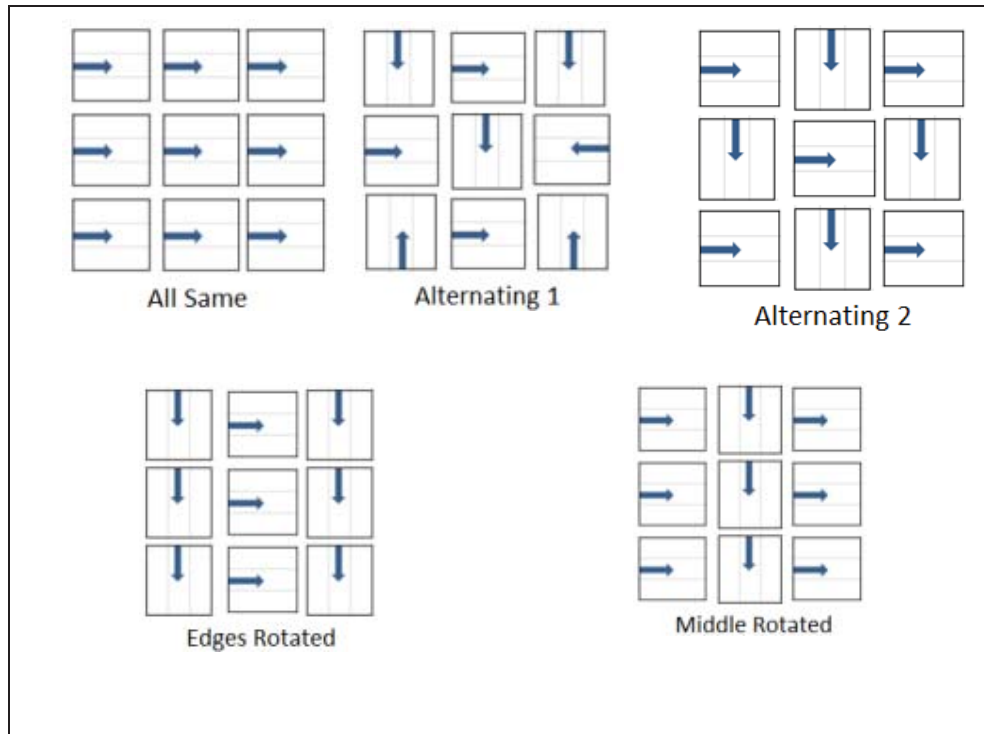


**Figure 3-8** Various orientations of the 9 lamps considered

### 3.4.2. Multiple Light Source Modeling

The single source data are then supplied to a MATLAB code that can arrange multiple light sources in various orientations then predict the combined distribution based on the assumption that multiple light sources are purely additive, with no interactions or reflections from external walls. This simple approach is deemed appropriate for making preliminary design decisions. The code appears in and very simple in logic. It takes in the single light source distribution and the desired combination of 9 light sources. Then appropriately shifts and rotates the single light source intensity distribution according to orientation and location, finally adding up all the correctly shifted and rotated single source distributions. In our evaluation, we considered the orientations appearing in

Figure 3-8 below where the arrow represents the location of the light bulb. These five combinations cover all possibilities of systematically placing the lamps to capture the effects of the asymmetry of the individual sources.

An additional variable that needs consideration is the spacing between the light bulbs. If all light sources are placed right next to each other with no space in between, we can get a spacing of 40cm between the centers of each bulb. However one may be able to extend this further and evaluate its impact on uniformity and intensity. Therefore this spacing was simulated at two additional levels to the 40cm minimum, namely at 45cm and 50cm.

The typical results for the combinations appearing in Figure 3.8 are shown in Figure 3.9 below in terms of contour plots where the light intensity is highest for red and successively drops to orange, yellow and blue at the lowest levels. As one can easily appreciate, the configurations different than the two alternating options provide regions of very low and very high intensity right next to each other due to the asymmetric nature of the rectangular lamp housings with the different edge slopes. Therefore the choice of orientation should definitely be one of the alternating options.

This summary shows that the alternating options are no different than each other. Both deliver at least 1.5X better uniformity than their counterparts for the other orientation options. The rotated options deliver slightly higher average power but this does not justify the uniformity degradation. Furthermore the lamp separation delivers an optimum for the 45cm option. As the lamps are further separated or brought closer together, the uniformity of ~11% is degraded. This optimal comes at a cost of reduced overall intensity as compared to the lamps that are closer but the additional uniformity justifies this loss. Furthermore the minimum separation of 40cm may cause difficulties when trying to build the support structure for the lamp housings. So this additional 5cm would actually make the design and construction easier. Based on these findings, our final design is configuration is fixed as the alternating 1 configuration with 45cm separation between the lamp centers.



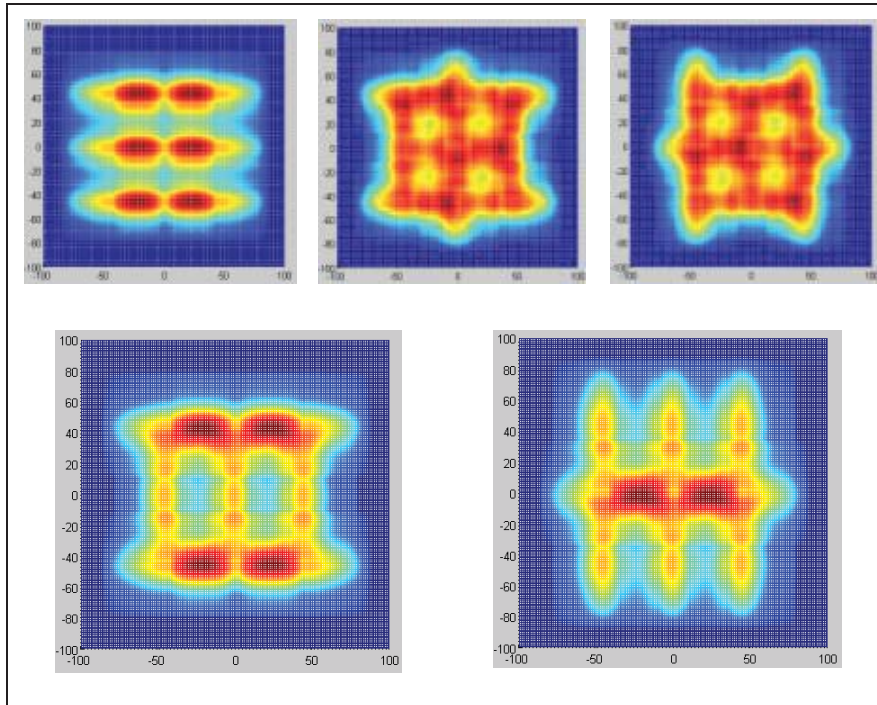


**Figure 3-9** Distribution at 45 cm lamp separation and 50 cm between the lamps and the panels

At 50 cm light source to panel separation, we project to get an overall intensity of  $777 \text{ W/m}^2$  averaged over an area of 1m by 1m. This will be slightly closer to the  $1000 \text{ W/m}^2$  standard in a  $80 \times 80 \text{ cm}$  square in the middle – however still not quite there. Thus the table needs to be located closer than 50cm to the lamps. When the data for 100 cm, 150 cm and 200 cm are evaluated in a similar fashion and one uses the inverse square law to predict at lower values than 50 cm – one can predict a separation of 42 cm for an intensity of  $1000 \text{ W/m}^2$  for the given configuration – based on the correlation of

Figure 3-10. Therefore the decision is made to place the bottom of the 20 cm diameter fans at 50 cm away from the light sources so that the table can be adjusted between 30 and 50 cm while still being in the direct path of the air circulation.

### 3.5. Finalized Design and Equipment

Based upon the decisions made using the data generated by the model of the previous sections, the light soaking station was built in the METU Chemical Engineering Department's machine shop. Several angles are pictures in

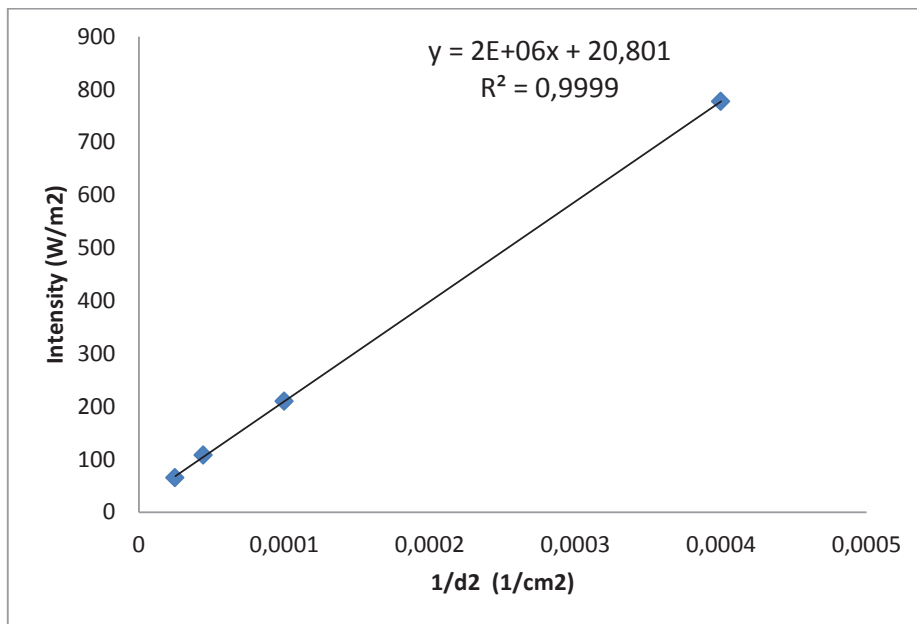


**Figure 3-10** Average intensity as a function of separation - inverse square behavior

**Table 3-1 Summary of the simulation results**

#	Lamp Orientation	Table Height (cm)	Lamp Separation (cm)	Mean (W/m <sup>2</sup> )	Sigma	% Sigma
1	All Same	50	40	922	204	22.1
2	All Same	50	45	777	209	26.9
3	All Same	50	50	652	215	33.0
4	Altern 1	50	40	922	129	14.0
5	Altern 1	50	45	777	87	11.2
6	Altern 1	50	50	625	112	17.9
7	Altern 2	50	40	922	129	14.0
8	Altern 2	50	45	777	87	11.2
9	Altern 2	50	50	625	113	18.1
10	Edges Rotated	50	40	952	221	23.2
11	Edges Rotated	50	45	797	193	24.2
12	Edges Rotated	50	50	627	183	29.2
13	Middle Rotated	50	40	892	238	26.7
14	Middle Rotated	50	45	757	186	24.6
15	Middle Rotated	50	50	623	181	29.1



**Figure 3-11** The Final Construction of the Light Soaking Station

Figure 3-11 below. One can see here all the features mentioned in the previous sections. 5 fans on one side take in the air and the 5 fans on the opposite side exhaust. Each fan has a capacity of circulating  $300\text{m}^3$  of air per hour. There are two handles on either side of the table for a total of four support points. These rods can be manually adjusted to move the table between 30cm and 62cm away from the light source. They can be made longer to bring the table even closer but then the table is beyond the region where air is circulated and this could cause cooling problems. The starters are placed on two shelves on two sides of the enclosure. The table dimensions are 135 cm by 135 cm. The 9 light sources used are all independently controlled, meaning that any combination can be turned on or off as desired.

## CHAPTER 4

### RESULTS AND ANALYSIS

#### 4.1. PV Performance Monitoring Station Analysis

##### 4.1.1. Data Integrity Issues

There were several issues which had to be dealt with in order to improve the quality and the continuity of the data generated by the performance monitoring station. These are going to be outlined in more detail under two separate headings below – one related to unforeseen fault issues and the other a more fundamental design issue while setting-up the measurements.

##### 4.1.1.1. Missing Data and Corrupt Sensor Problems

As will be apparent in the upcoming trend analyses, there will be periods of no measurements. These are mostly due to specific sensor problems related to the weather monitoring station. In particular there were problems with the pyranometer used to measure solar irradiation – which was later resolved by providing adequate electrical grounding to the module to discharge static electricity build-up, particularly during windy conditions.

There was also another fault by the Daystar equipment in which the continuous writing of the IV curves to the system's hard drive – resulting in the loss of PV performance data for a certain time period.

All of these shortcomings were addressed during this study and the system is currently reliably collecting and archiving data.

#### **4.1.1.2. Design Upgrade for Spectrophotometer (Shutter Arrangement)**

Spectrophotometer was an important part of the outdoor test station since it was going to provide spectral distribution of the sunlight in a continuous manner, therefore makes it possible to compare and correlate the power data and I – V curve measurements of the panels with different technologies and there could be a link between the degradation modes and mechanism with the spectral distribution of the sunlight, for instance different technologies could absorb different regions of the spectrum causing different degradations in the molecular structure. However, the nature of the equipment and the software are not very suitable for outdoor and continuous data acquisition and the other alternatives that are designed for this purposes mentioned above are very disadvantageous financially. The main problem with the measurements is the need for taking periodical dark measurements for calibrating the device. This does not seem practical and possible when the spectrophotometer is operating in an outdoor environment with 24 hours of operation since it is mainly designed for instant data capturing in a laboratory environment for the experiments not lasting more than a day. Taking these periodic dark measurements will not be feasible when the nature of a remote outdoor station is concerned; therefore a shutter design is made to make this possible. A shutter with a simple motor is designed to close the upper side of the sensor to prevent contact with the sunlight in a desired interval or manually. Below, one can see the design of the shutter with its components.

#### **4.1.2. Trend Analysis on Historical Climatic Data**

We have solar irradiation (and meteorological data) from the installed HOBO Weather Station since April 2012 and reference meteorological data obtained from Turkey Meteorological Data Archive and Management System (TÜMAS) between the years of 2010 and 2013. There are a few periods where data is missing in HOBO Weather Station. These are mainly due to the radiation sensor failure periods as mentioned.

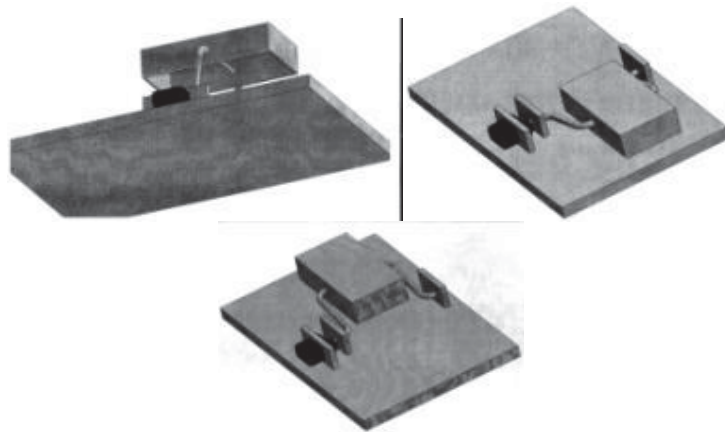


**Figure 4-1** Shutter Design

Figure 4-2 and Figure 4-3 shows the distribution of the temperature and solar irradiation data throughout the years of 2010 – 2013 in Ankara region respectively, based upon the meteorological monitoring station located in Ankara. Specific location is 39.97 North latitude and 32.86 East longitude. In comparison to the METU weather monitoring station located at 39.89 North latitude and 32.78 East longitude. The latitude of the two locations is 891 m and 914m respectively. The distance between the two stations is approximately 17 km. Therefore, this proximity of the reference meteorological station gives us a change to calibrate and confirm identical measurements taken at our stations.

The impact of seasonal variations could be clearly seen when the official data is investigated. The variation with respect to the seasons is quite predictable over the course of 4 years that we have the data for.

There are two shortcomings related to meteorological data usage from this official source. One is that this data is available only on an hourly basis whereas we capture performance data from our panels on a minutely basis. Furthermore, although the proximity of the two locations allows us to compare the average measurements over a long period of time – individual measurements are still likely to be different due to location specific, instantaneous atmospheric conditions such as could cover.

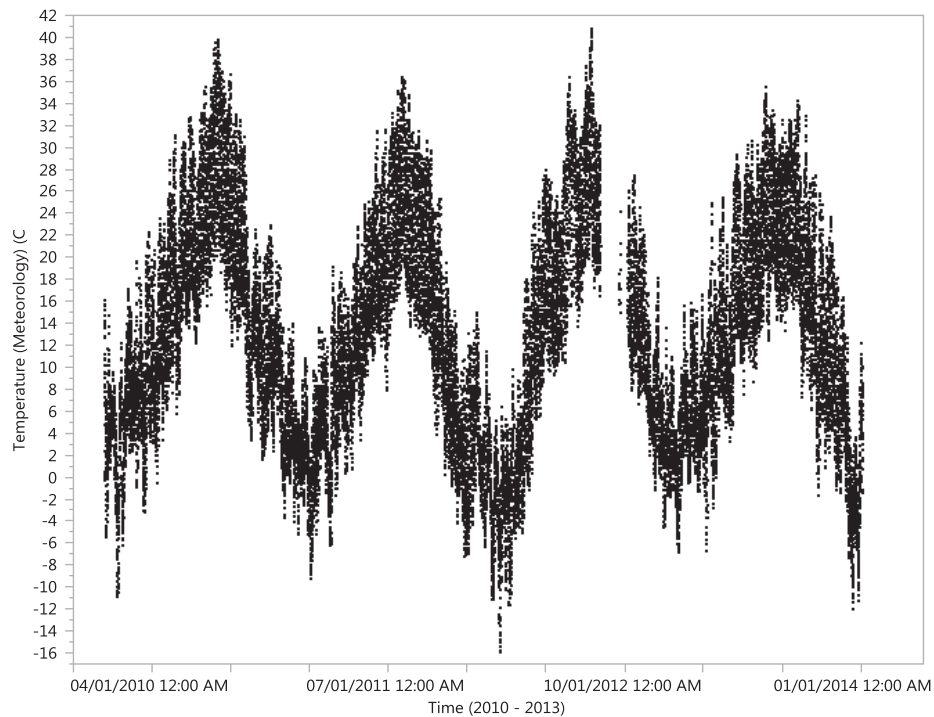


**Figure 4-2** Reference Temperature Data throughout 2010 – 2013

Therefore we need to establish the validity of the for HOBO data, by direct comparison to their counterparts from the TÜMAS database, which is the system that collects and stores meteorological data from the reference stations. Correction factors are calculated for HOBO data where appropriate.

The data comparison is simply plotting the data that belong to the same period in time against each other to see if there is a strong correlation. In order to do that, the data from HOBO and reference are taken and formatted to fit on to each other since there are gaps in the timeline of the data collection because of the errors in the HOBO system. In addition to that, the data taken from TÜMAS has hourly values of the parameters while HOBO Weather Station measures and records data with the intervals of ten minutes. Therefore, summary table and data merging tools of JMP



software is used to merge the data belonging to the same year, month, day, hour and minutes. Lastly, time correction is made since TÜMAS values are in terms of Greenwich Mean Time (GMT) while HOBO records measurements according to the local time – so daylight savings time need to be considered. After this fitting procedure, all parameters are readily compared with the reference values.

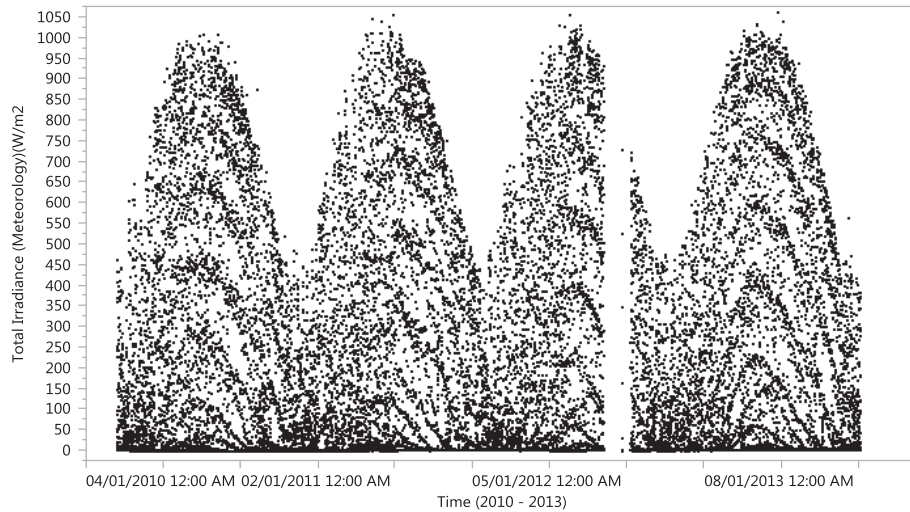


**Figure 4-3** Reference Solar Irradiation Data throughout 2010 – 2013

The temperature comparison is shown in Figure 4-4. After the comparison of the data, the following equation is found with  $R^2$  value of 0.98.

$$Temp\ HOBO = 1.3756009 + 0.9546787 \cdot Temp\ Reference \quad (4.1)$$

Temperature value is in °C. The small intercept and the value of the slope close to unity indicate that the HOBO measurements are within 5% of the reference meteorological data – which is a reasonable fit.

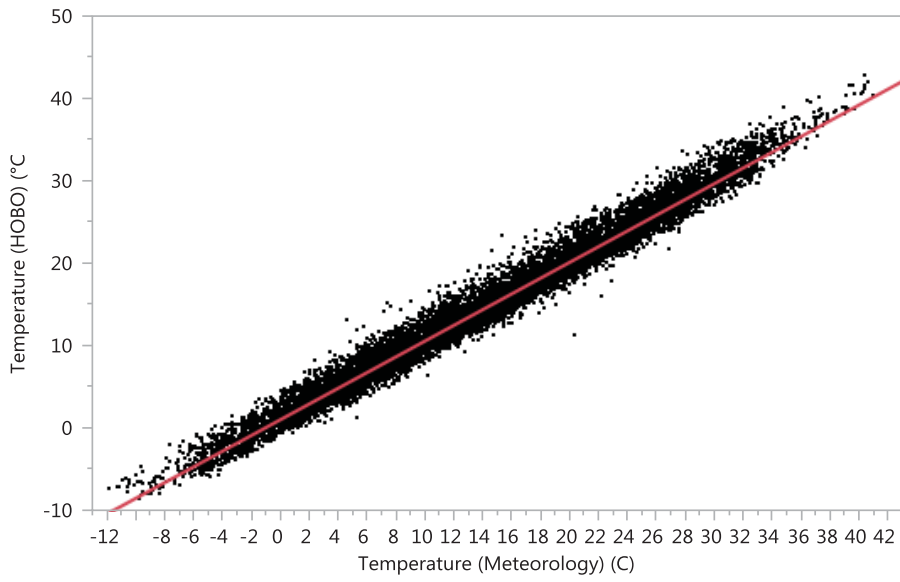


**Figure 4-4** Temperature Data Comparison

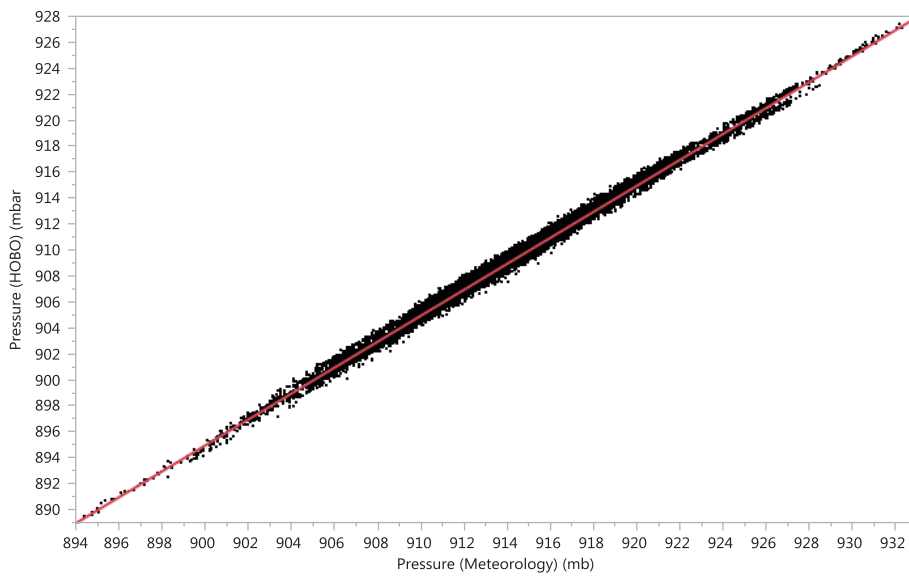


**Figure 4-5** Pressure Data Comparison

The pressure correlation is demonstrated in Figure 4-5. This comparison indicates a correlation coefficient,  $R^2$  of 0.99.

$$Pressure_{HOBO} = -4.381457 + 0.9994373 \cdot Pressure_{Ref} \quad (4.2)$$

Pressure value is in mbar. The pressure data from our weather monitoring station is almost in complete agreement with the reference data.

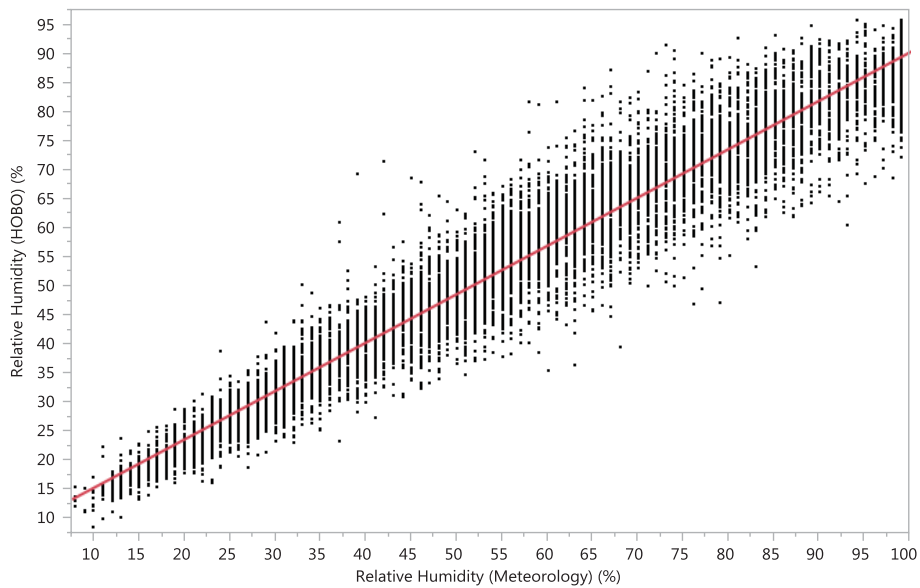


**Figure 4-6** Relative Humidity Data Comparison

As shown in Figure 4-6, the correlation of RH is much worse in comparison with the pressure and temperature measurements outlined above. The value of  $R^2$  is 0.94.

$$Rel.Hum. \text{ HOBO} = 7.3141599 + 0.8306818 \cdot Relative \text{ Hum. } Ref \quad (4.3)$$

Relative humidity value is in (%). There is quite a significant off-set between the two sources – but the trend is identical. So impact of RH on panel performance can be evaluated, even though the absolute value of the variable may not necessarily very accurate. There should not be this much discrepancy in RH values simply due to the location difference between where the reference and our measurements are made.

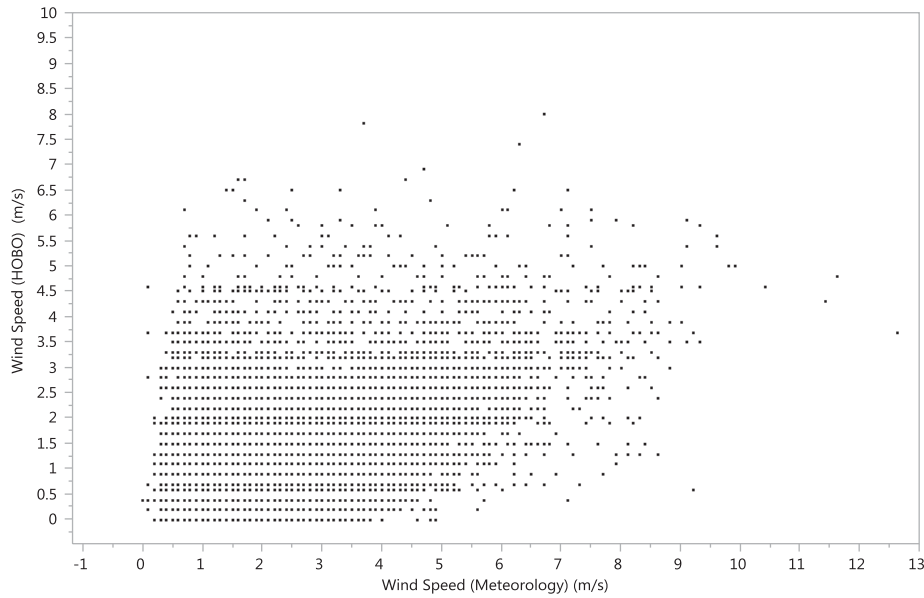


**Figure 4-7** Wind Speed Data Comparison

Wind speed and direction data do not show strong correlations at all – shown in Figure 4-7 and Figure 4-8. This could be due to two weather stations being in different locations which could have different wind amounts when the speed is concerned – wind being a much more local variable that can be impacted by

geological features and man-made structures. In addition to that the range of measurements, in particular of wind speed, is very narrow. We are most likely sampling a lot of points at the lower end of our instrument's range. As we sample higher wind speeds, the trend may become more apparent.

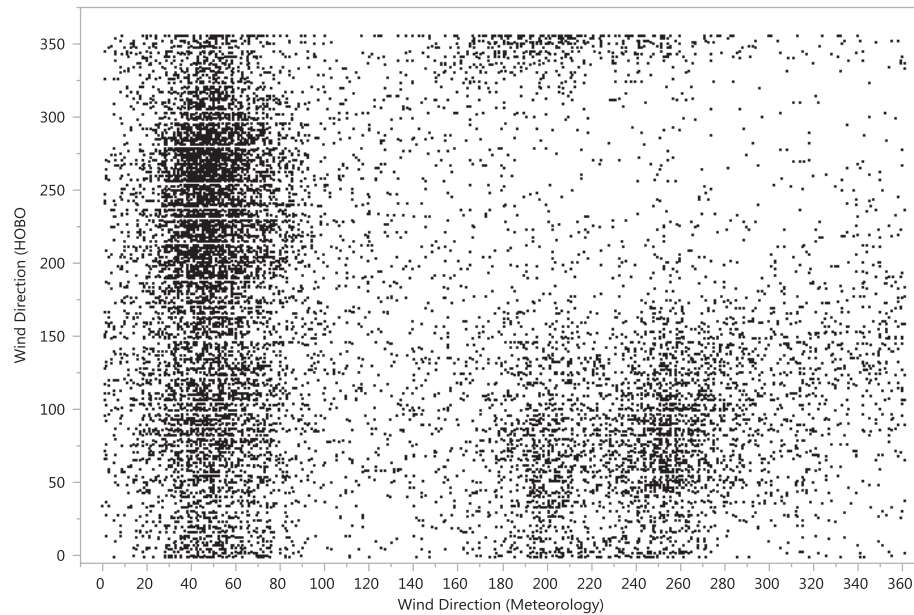


**Figure 4-8** Wind Direction Data Comparison

The aforementioned data are of secondary importance when solar panel performance is considered. Solar panel power production is a very strong function of irradiation and therefore this is perhaps the most important parameter that we need to calibrate. The plot of the HOBO irradiance measurements vs. the references are shown in Figure 4-9.

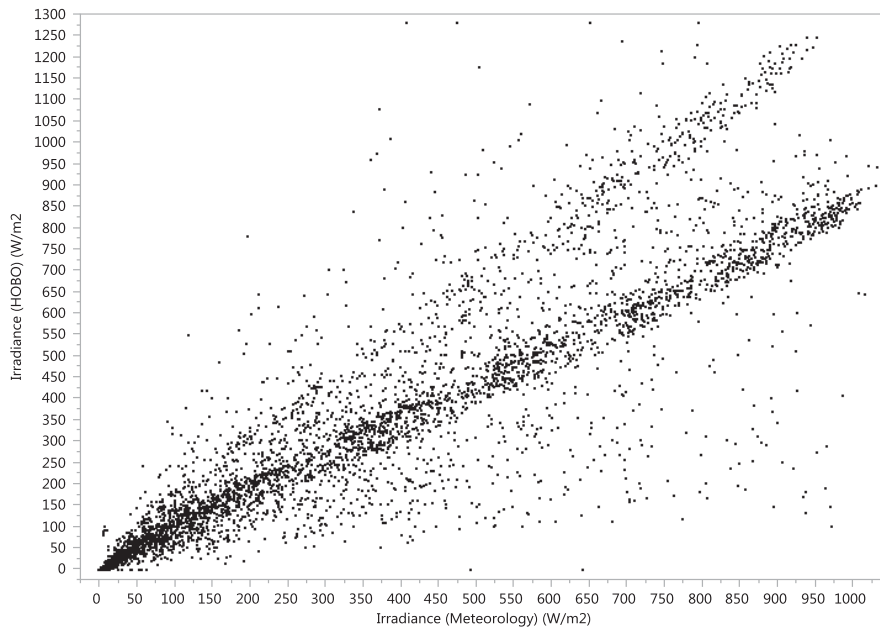


**Figure 4-9** Solar Irradiance Data Comparison

When the solar irradiance data is investigated, it could be seen that two different regions exist. The above region shows higher values for HOBO measurements in terms of the reference irradiance while the below region which contain more data seem to show a more even correlation between HOBO and reference values. Furthermore it is seen that the group of data points belonging to the above region all come from a specific time period towards the end of the summer of 2013, ending with a complete sensor failure which resulted in replacement and repairs. Therefore, it is decided to take these two regions separately to find the related correction factors for HOBO measurements.

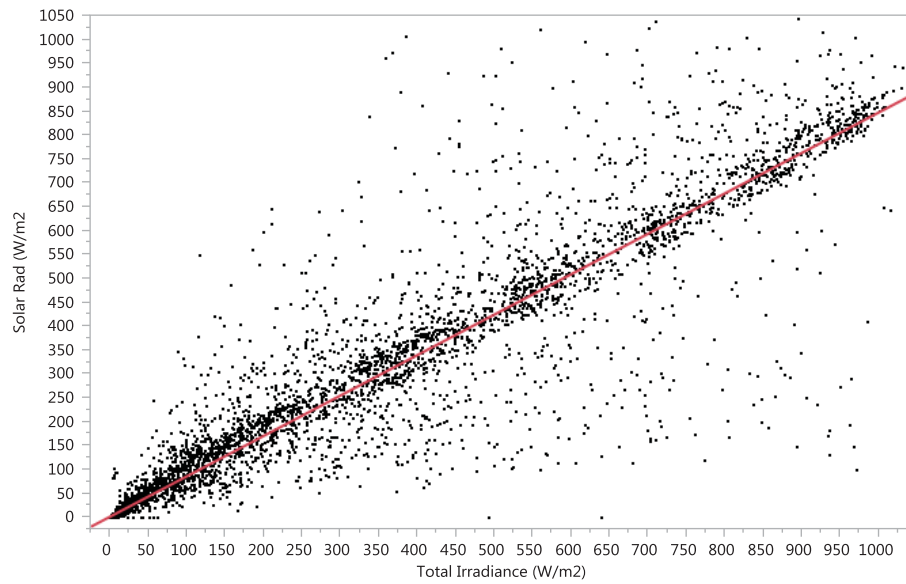


**Figure 4-10** Solar Irradiance Data Comparison for Below Region

Figure 4-10 shows the correlation for the lower group, where agreement between our and reference measurements are more close. After the comparison of the data, the following equation is found with  $R^2$  value of 0.91.

$$\text{Solar Irr. HOB0} = 4.5905497 + 0.8454973 \cdot \text{Solar Irr. Reference} \quad (4.4)$$

Solar Irradiance value is in ( $\text{watt/m}^2$ ). This shows that our measurement is consistent in terms of trending with the reference but is approximately 15% off as the slope is around 0.85 instead of unity. The scatter in the data could be due instantaneous differences in cloud cover.

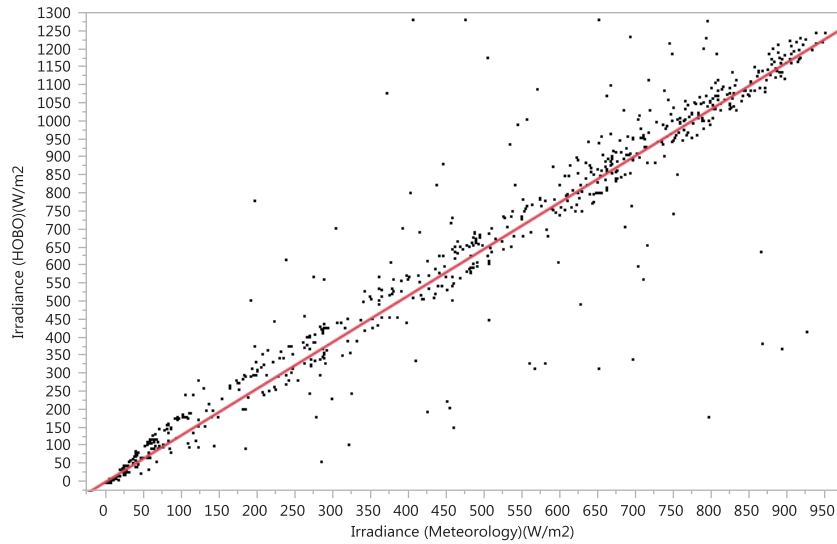


**Figure 4-11** Solar Irradiance Data Comparison for Above Region

We then look at the upper region in Figure 4-9 separately in Figure 4-11. After the comparison of the data, the following equation is found with  $R^2$  value of 0.95.

$$\text{Solar Irr. HOBO} = 5.2701976 + 1.2895323 \cdot \text{Solar Irr. Reference} \quad (4.5)$$

Solar Irradiance value is in ( $\text{watt/m}^2$ ). Again there is a consistent trend but now more than a 25% offset with respect to the reference is seen, in comparison to the 15% offset in the opposite direction for the remaining dataset.

Table 4-1 below summarizes the intercept and slope values of the parameters in the weather station for a linear fit with the reference data. These values are further used to calculate the corrected values for HOBO Weather Station and used in the performance characterization parameters of the solar modules. The significant values are taken up to the last digit since they are going to be used in the correction formula in this form, without rounding.



**Table 4-1** Summary for Correction Values of Meteorological Parameters

<b>Parameter</b>	<b>Intercept</b>	<b>Slope</b>
Temperature	1.3756009	0.9546787
Pressure	-4.381457	0.9994373
Relative Humidity	7.3141599	0.8306818
Solar Irradiance (Above Region)	5.2701976	1.2895323
Solar Irradiance (Below Region)	4.5905497	0.8454973

After the correction of the solar irradiance data – using different calibration factors based on the slopes and intercepts summarized in Table 4-1, the correlation between the reference irradiance and our measurements is very strong. The scatter is still there as expected since we are calibrating based on the correlation of the data on an overall basis.

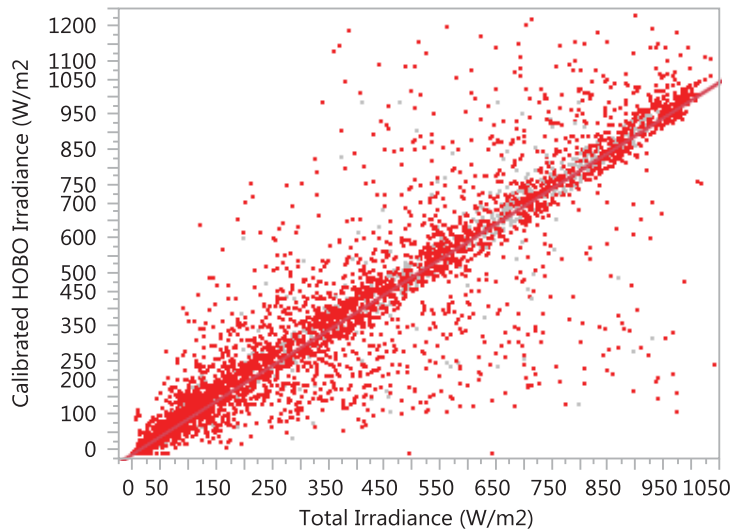


**Figure 4-12** Corrected HOB0 Irradiance vs. Reference

$$\text{Calibrated Irrad. HOB0} = 3.1013 \cdot 10^{-8} + 1 \cdot \text{Irrad. Ref} \quad (4.6)$$

### 4.1.3. Correction for Module Tilt

One of the primary issues with the present set-up to capture solar irradiance data is that the pyranometer that is used to capture the irradiation data and the solar panels are at different levels of inclination with respect to the horizon. The pyranometer is horizontal and equipped with a 180° cosine collector that captures the total incident irradiation within its entire field of view. The panels, on the other hand, face directly south and are inclined at an angle of 28.6° with respect to the horizontal. In fact all panels in the northern hemisphere are directed towards the equator (or directly south) and installed at ever increasing angles as one moves away from the equator. This is to capture as much sun possible throughout the year. Thus a panel inclined at the correct angle will receive, on the average, more irradiation than a horizontal panel.

One way to account for this discrepancy is to install the pyranometer at the same level of inclination as the solar panels and it would be subjected to exactly the same conditions as the panels. This however would invalidate any efforts to calibrate the installed pyranometer against the reference data collected by the meteorology department, who have pyranometers installed horizontally only. So even if one were to install two pyranometers, one horizontal and the other inclined with the panels, one would still have to be able to estimate the correlation between the two. The estimation of this correlation depends on the specific position on the globe (which is fixed by the coordinates of the station in terms of latitude and longitude) as well as the precise position of the sun, which is a function of time of the day and the year.

#### 4.1.3.1. Determination of the Tilt Correction

##### 4.1.3.1.1. Horizontal to Tilted Irradiance – Geometrical Input

The equation that relates the irradiation,  $E_s$ , on a surface tilted by  $s$  degrees from the horizontal is given by

$$E_s = E_{bn} \cos \theta + E_d R_d + \rho E R_r \quad (4.7)$$

Where  $E_{bn}$  is the direct normal irradiance,  $E_d$  is the diffuse horizontal irradiance;  $E$  is the global horizontal irradiance.[118] The other factors appearing in this equation are  $\theta$  representing the angle of incidence of the sun rays on the tilted plane,  $R_d$  denoting the diffuse transposition factor,  $\rho$  for the foregrounds' albedo and finally  $R_r$  as the transposition factor for ground reflection. The irradiance factors that appear on the right hand side are also interrelated with the expression

$$E = E_{bn} \cos(Z) + E_d \quad (4. 8)$$

where  $Z$  denotes the zenith angle of the sun.

Using this second relationship, one may be able to use two out of the three irradiance terms and calculate  $E_s$ . However in our case, as is the case in many situations, Only  $E$  is available (this is what is measured by the horizontal pyranometer) and  $E_s$  must be estimated based only on this component.

Further simplifications to this set of equations (based on ignoring the ground reflections and the dependence of the diffuse irradiation to the sun's position) results in a purely geometrical relationship between the measured horizontal irradiance and the inclined irradiance as

$$E_s = E \frac{\sin(\alpha + s)}{\sin(\alpha)} \quad (4. 9)$$

Where the newly introduced variable,  $\alpha$ , represents the solar elevation angle and is given at any time by the relationship

$$\alpha = 90 - \phi + \delta \quad (4. 10)$$

where  $\phi$  is the latitude and  $\delta$  is the declination angle of the sun.

#### **4.1.3.1.2. Solar Position Estimation**

Then the problem is reduced to determination sun with respect to the METU PV performance monitoring station so that the time dependent declination angle and elevation angle can be calculated.

There are several methods available in the literature to make these estimations. We preferred the usage of the method utilized by the NOAA (National Oceanic and Atmospheric Administration).[119] Their website provides downloadable and editable spreadsheets whose prediction formulae can be directly integrated into our MATLAB code. The details of the calculations can be found on their web-site which indicates a very good level of accuracy between the years of 1800-2100. Like most other solar vector estimation algorithms, the calculations depend on the determination of the Julian century – which estimates the approximate position of the earth on its solar orbit based on the current date and time. The celestial coordinates, namely the declination and right ascension, estimated based on this position of earth are then converted to the coordinate system that is centered on the position of the globe where the observation station is located – as defined by the longitude and latitude. Once this conversion is complete, the elevation and zenith of the sun is calculated – which can then be used in (3) and (4) to convert the measured horizontal irradiance to the inclined irradiance as seen by the modules.

#### **4.1.3.2. Yearly Trends of Solar Position**

The METU solar station is positioned at  $39.39^\circ$  North latitude and  $32.72^\circ$  East longitude – based on the coordinates provided by Google Maps.[120] The local time at any given point must be converted to the Coordinated Universal Time (UTC). When daylight savings time is not in effect, local time in Turkey is UTC+2hrs. The daylight savings time adds another hour, bringing Turkey to UTC+3hrs. The beginning and end dates of the daylight savings time in Turkey over the past few years can be found that the ministry of Energy's website.[121] The general trend is that daylight savings time begins in the last week of March and lasts until the last

week of October. The implementation is made during the night that connects the last Saturday of the week to the last Sunday.

The location and daylight savings time correction have been coded into MATLAB along with the NOAA algorithm that calculates the solar position. This code allows for the determination of the correction factor to convert the measured horizontal irradiation to the desired inclined irradiation for any given day and time.

This script was used to evaluate the solar position as a function of date and time for the METU solar monitoring station. The data is summarized in terms of monthly averages vs. time of the day in Figure 4-13. Sunset and sunrise is defined formally as when the zenith angle crosses over the  $90^\circ$  value. As once can see, days get longer and peak at around June and July, then fall back to minimum levels close to December and January – in line with the summer and winter solstices falling on June 21<sup>st</sup> and December 21<sup>st</sup> respectively.

The presented modeling approach does have two significant shortcomings around sunset and sunrise however. The NAOO algorithm demonstrates most errors in this region as it does not incorporate the reflections that sunlight goes through in the atmosphere. These effects are most pronounced during sunrise and sunset where the angle of incidence of the sun rays is close to the horizon. Furthermore the atmospheric effects that greatly influence the diffuse radiation are most significant during these extreme times – and this effect is ignored in the geometrical only approach that is taken to convert horizontal to inclined radiation.

In order to filter out these points, a more conservative definition of sunrise and sunset is implemented – otherwise negative correction factors are possible. Based on the analysis of the data, we define the presence of the sun in the sky for zenith angles that are less than  $80^\circ$ , which systematically filters out the cases where the sun is very close to the horizon. Beyond these points, we defined the correction factor as zero, meaning that there is no sun in the sky. This actually does not impact our calculations very significantly because these time periods correspond to very low

irradiation levels anyway and does not capture any significant power generation from the modules.

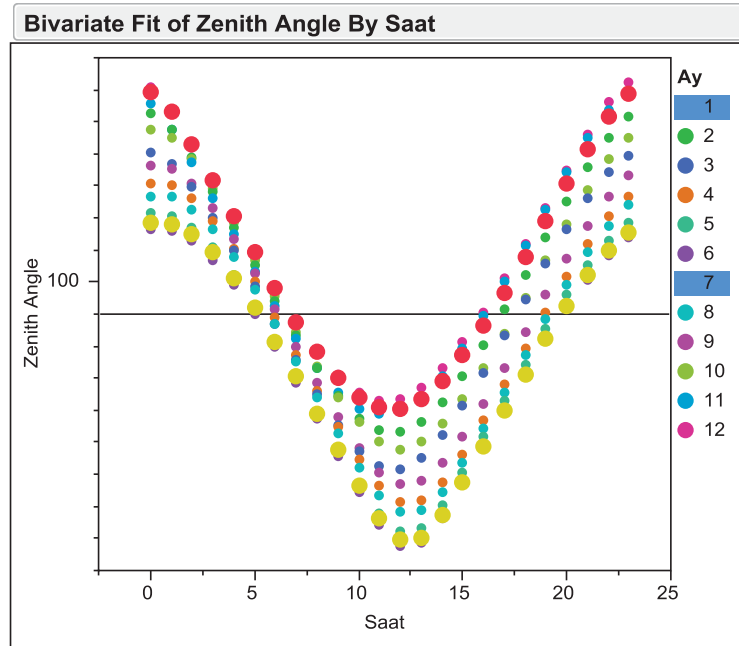


**Figure 4-13** Solar Zenith Angle

Based on this filter, the hourly average tilt correction factors are plotted in Figure 4-14, with respect to time of day. The larger dots represent the winter months, where the correction factor is always above 1.0 – this compensates for the relatively lower levels of solar irradiation during these months and tries to even out the total power generation through the year. This however results in tilt correction factors that are very close to 1.0 and actually lower than 1.0 during the hours right after sunrise and right before sunset - during the summer months. So one may actually propose to implement different inclination angles by season or month – with the extreme case of

this proposal being solar vector dependent inclination angles, which is the basis for trackers. One would need to carry out a cost vs. benefit analysis here because any dynamic change in inclination angle, even though on a seasonal basis, is going to require some operational cost.

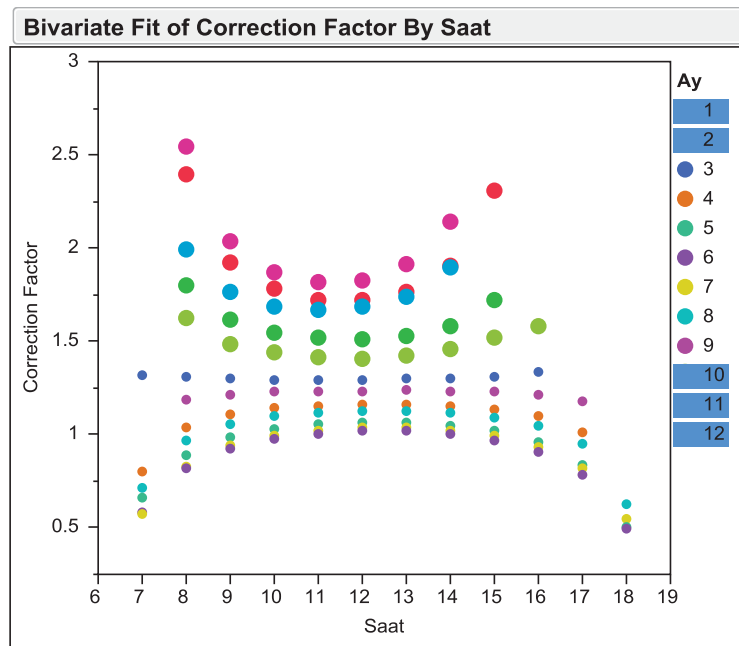


**Figure 4-14** Tilt Correction Factors by Time of day, colored by month

#### 4.1.4. Analysis of Solar Panel Performances

The HOBO data that is calibrated and confirmed with respect to the reference measurements are then merged with the Daystar readings that capture the panel performance. The HOBO irradiance data is also corrected for the module tilt as outlined in Section 4.1.3. Panel performance is quantified based on regularly captured IV traces from which the Daystar software automatically captures  $P_{max}$ ,  $I_{sc}$ ,

$V_{oc}$  and the FF. We have developed our own MATLAB code that further analyzes the IV traces to capture  $R_s$  and  $R_{sh}$  values from the slopes near  $V_{oc}$  and  $I_{sc}$  points.

With this data set at hand, it will be possible to correlate all relevant performance metrics to meteorological conditions. The number of valid data points per installed panel and technology are outlined in Table 4.2.

For analysis purposes, the radiation levels are also grouped into specific irradiance bins – to see later on in the analysis whether some correlations exist with respect to the irradiance level. Again this grouping is made based upon the irradiance level that is corrected for module tilt.

It is also customary to normalize power outputs with respect to nominal panel production and the level of irradiance in order to be able to compare a large dataset involving panels of different technologies. The specifics of the metrics introduced below are explained in Section 1.3.7. First the final yield normalizes the power output with respect to nominal panel output at STC by

$$Y_F = E \cdot P_{PV,Rated} \quad (1.5)$$

Then the reference yield is defined as solar radiation divided by the reference solar radiation at STC which is  $1000 \text{ W/m}^2$ .

$$Y_R = H_t / 1000 \quad (1.6)$$

Finally the performance ratio normalizes  $Y_F$  with  $Y_R$  to indicate whether the panel is producing as much power as it should under the given irradiance conditions.

$$PR = Y_F / Y_R \quad (1.7)$$

If all measurements are correct, the PR can take a maximum and optimal value of unity.



**Table 4-2** Summary of Data Points

<b>Panel ID</b>	<b>Technology</b>	<b>Data Points</b>	<b>Date Installed</b>
Chiner (160W) – Clean	Monocrystal Silicon	4261	8/2/2012
Chiner (160W) – Dirty	Monocrystal Silicon	7660	4/7/2012
Chiner (240W)	Polycrystal Silicon	1981	4/7/2012
Isophoton (240W)	Monocrystal Silicon	7372	4/7/2012
Sanyo HIT (230W)	Monocrystal Heterojunction with Intrinsic Thin Layer	1813	6/28/2013
Sharp (128W)	Amorphous Thin Film Silicon	8914	4/7/2012
SolarA (130W)	Polycrystal Silicon	4444	7/23/2012

**Table 4-3** Grouping Radiation Levels

<b>Sun Level</b>	<b># of Points</b>	<b>LOW</b>	<b>HIGH</b>
4	3095	750	-
3	5808	500	750
2	3961	250	500
1	11416	0	250

We first investigate what drives power generation from the modules. The  $V_{oc}$  and  $I_{sc}$  plots vs  $P_{max}$  clearly show that increased power generation is driven most significantly by  $I_{sc}$ . The  $V_{oc}$  values quickly reach their nominal values and stay there for entire region for all technologies. This is the expected behaviour for photovoltaic panels, where the power generation is driven by the number of photons – where larger numbers generate more electron hole pairs resulting in larger photocurrent. The  $V_{oc}$  is a fundamental material property that does not change with the level of irradiance.

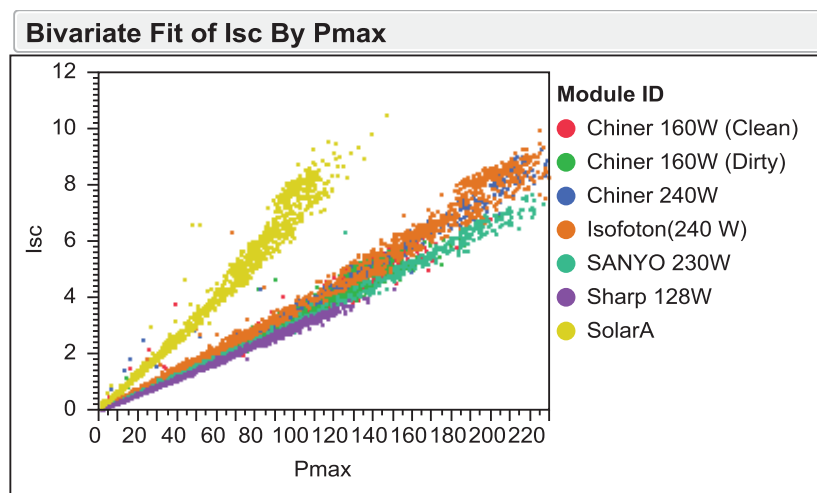


**Figure 4-15** Maximum Power vs. Short Circuit Current for Installed Panels

In Figure 4-17, we look more closely at the FF. The fill factor shows a steady decrease with increasing power output as the panel approaches its nominal capacity. This can be due to either increases in  $R_s$  or decreases in  $R_{sh}$ . We then look at these two parameters in further detail in Figure 4-18 and Figure 4-19.

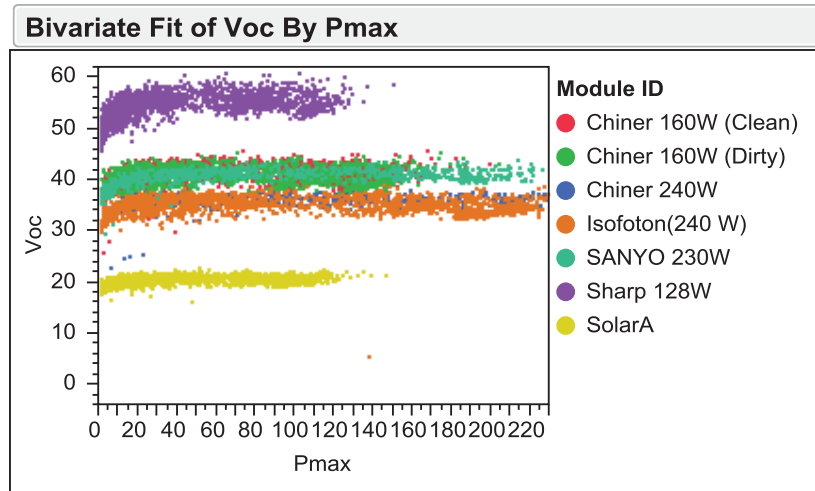


**Figure 4-16** Maximum Power vs. Open Circuit Voltage for Installed Panels

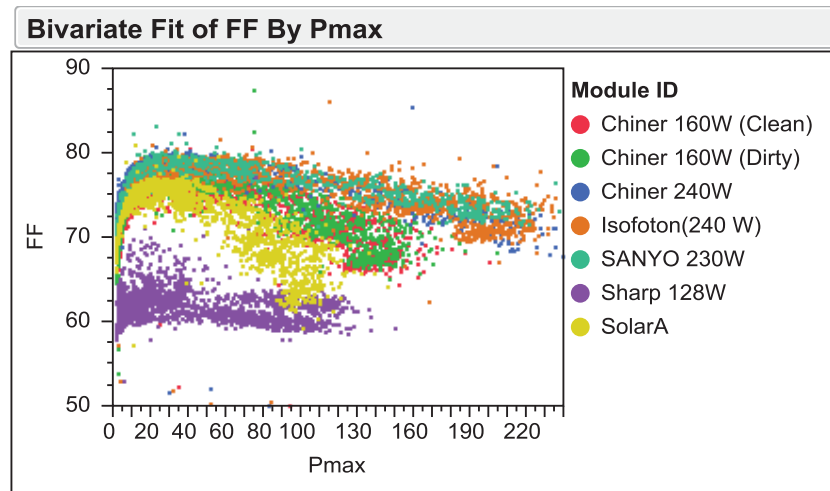


**Figure 4-17** Maximum Power vs Fill Factor for Installed Panels

It is clearly seen that the series resistance is changing in the positive direction as power production increases whereas the shunt resistance is changing in the undesired direction. So we can conclude that the loss of fill factor is due to the falling value of  $R_{sh}$ , which is an indication of the increase in the slope of the IV curve where it nears the  $I_{sc}$  point. This is inline with the previous observation of  $P_{max}$  being driven by the  $I_{sc}$ . The  $V_{oc}$  point is relatively fixed and power generation is driven by increasing  $I_{sc}$  and as indicated by the falling  $R_{sh}$  and subsequently the FF, the portion of the IV curve between  $I_{max}$  and  $I_{sc}$  is not shifting up parallel to the horizontal axis but also changing its slope slightly as  $I_{sc}$  increases. This loss mechanism shows different levels of significance depending on the module technology.

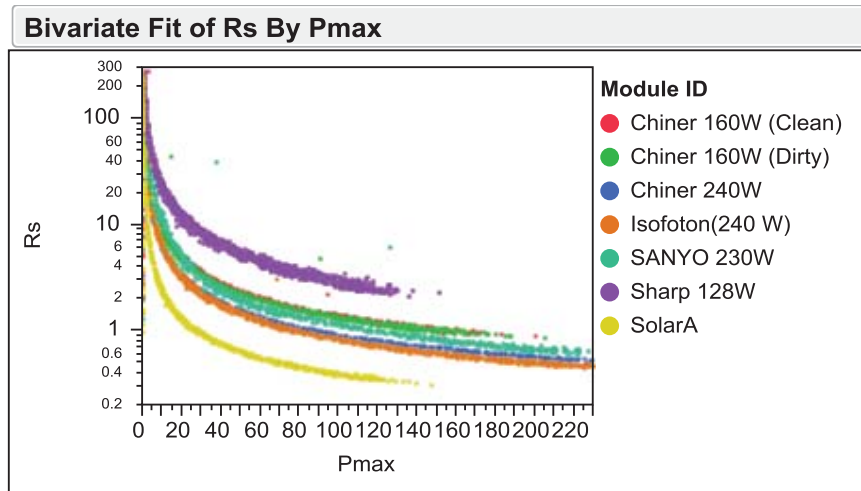


**Figure 4-18** Maximum Power vs Series Resistance for Installed Panels

Next we investigate the overall performance of the panels based on their performance ratios. The box plot in Figure 4-20 is generated to make this comparison. Note that there are still some points for PR greater than unity, which means that there are still some inaccuracies in our solar irradiance data. However more than 95% of the data points included are below unity in terms of performance ratio.

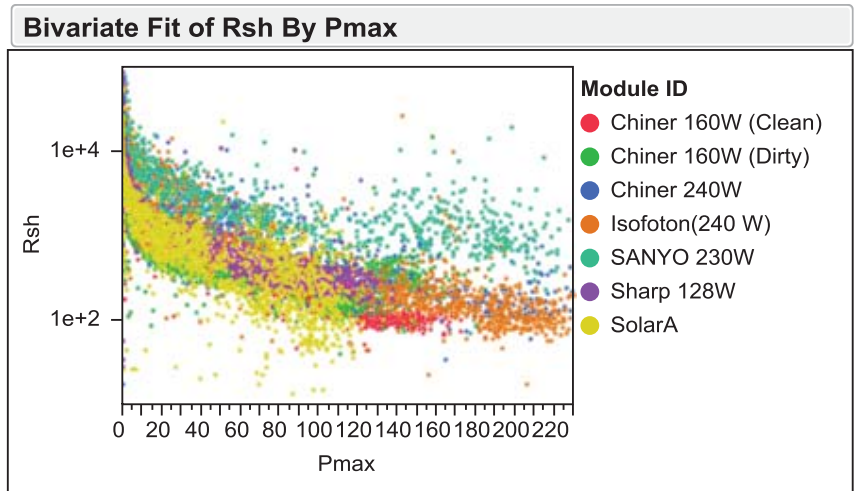
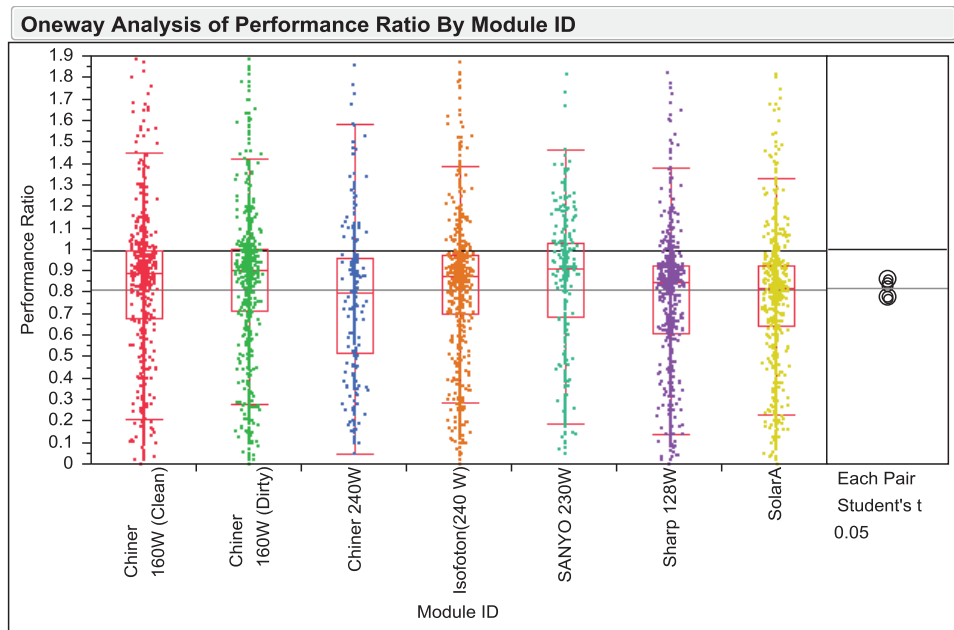


**Figure 4-19** Maximum Power vs Shunt Resistance for Installed Panels



Excluded Rows 6607

**Figure 4-20** Performance Ratio Comparison

When one makes a statistical evaluation of the performance ratio metric, it is seen that the panels fall into two distinct categories. Table 4-4 shows the pair wise t-test comparison of the mean of the  $P_R$  with a 95% confidence level. The monocrystalline based technologies are in the upper groups where as the polycrystalline and amorphous thin film technologies fall into the second category. Among the upper group, the heterojunction technology shows superior performance – and among the lower group the amorphous technology shows the worst performance. However these two conclusions are not statistically justified at the 95% level.

The  $P_R$  metric is also very useful when considering the impact of secondary factors such as temperature, pressure and RH on panel performance because it normalizes the impact of solar irradiance – which by far has the most significant on  $P_{max}$ . Therefore we investigate these impacts based on the  $P_R$ .

This analysis is visualized in Figure 4.21 through Figure 4.23. It is seen; in general that increasing temperature and decreasing RH have a negative impact on panel performance. This is most strongly demonstrated at higher irradiation levels – thus the aforementioned plots are generated for irradiance conditions that are larger than  $750W/m^2$ . Below  $500W/m^2$ , and particularly below  $250W/m^2$ , the correlations gradually lose significance and eventually disappear. The pressure has no impact on performance.

The loss in performance is inline with the expectations based on the negative temperature coefficient at  $P_{max}$ . It is very difficult to make a quantitative analysis based on individual panels and PV technologies due to the large amount of scatter in the data. It seems from a qualitative perspective that there are no significant differences between the panels. The range of quoted temperature coefficients are between 0.24 and 0.55; so one would expect to see some difference. However we would have to generate more data to observe these differences.

**Table 4-4** Statistical Comparison of Panel Performance Ratios

<b>Level</b>	<b>Category</b>	<b>Mean</b>
SANYO 230W	A	0.8624
Chiner 160W (Dirty)	A	0.8587
Chiner 160W (Clean)	A	0.8424
Isofoton 240W	A	0.8284
Chiner 240W	B	0.7810
SolarA	B	0.7781
Sharp 128W	B	0.7703

A fundamental measurement issue could also be in play here, where we are assuming that the ambient temperature is a direct indication of the panel temperature – which is a questionable assumption. The temperature measurements in the HOBO station are taken through a shaded temperature measurement device whereas the panels are exposed to radiation and their temperature could vary significantly from those measured under the shade. This is probably what is causing the scatter in the data and can be resolved by installing thermocouples to monitor actual panel temperatures. The Daystar equipment already has this monitoring capability.

The impact of RH can be attributed to the diffuse radiation component, where when there is more moisture in the air, the diffuse component of the radiation is potentially higher than the dryer conditions where the sunlight is not going to have as many water molecules on its path.

## 4.2. LID Station Measurements

### 4.2.1. Light Intensity Measurements

Once the construction is made, the next step was to characterize the light distribution and fine tune the spacing to deliver  $1000\text{W}/\text{m}^2$  average intensity. We first look at how long it takes for the light intensity to stabilize. For this purpose we fix the table at 47cm, place the reference cell at a fixed position and begin the record the intensity at 1 minute intervals. We see a very rapid increase in the first 10 minutes that then very slowly stabilizes in the next 20 minutes. Based on this transient data, it would be fair to say the output of the lamps stabilize within 30 minutes. Any further characterization or aging study needs to take this into account.

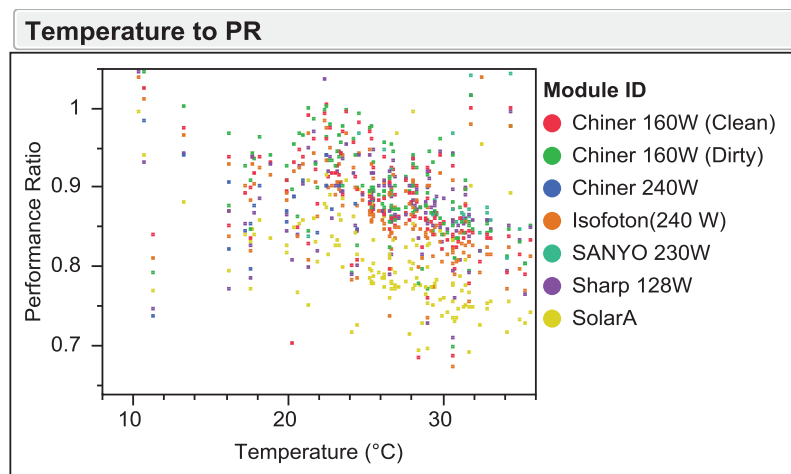


**Figure 4-21** Performance Ratio vs Temperature for Installed Panels



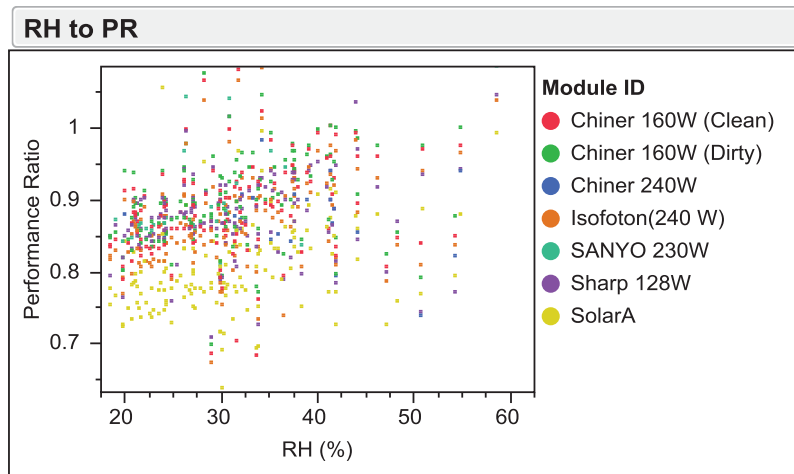


**Figure 4-22** Performance Ratio vs Relative Humidity for Installed Panels

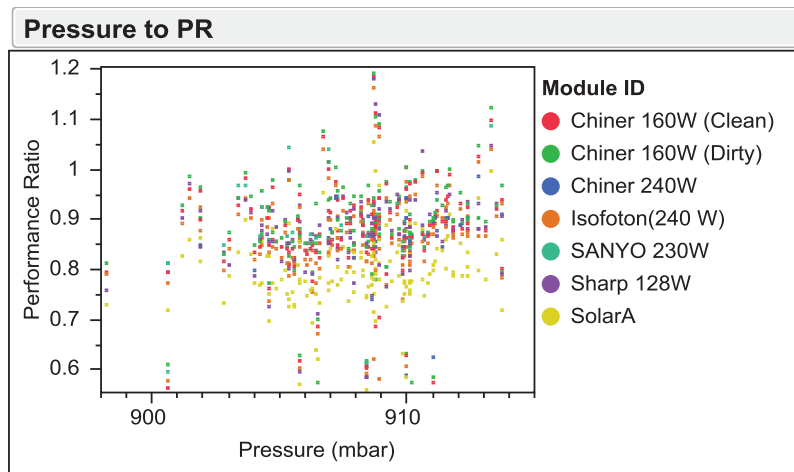


**Figure 4-23** Performance Ratio vs Pressure for Installed Panels

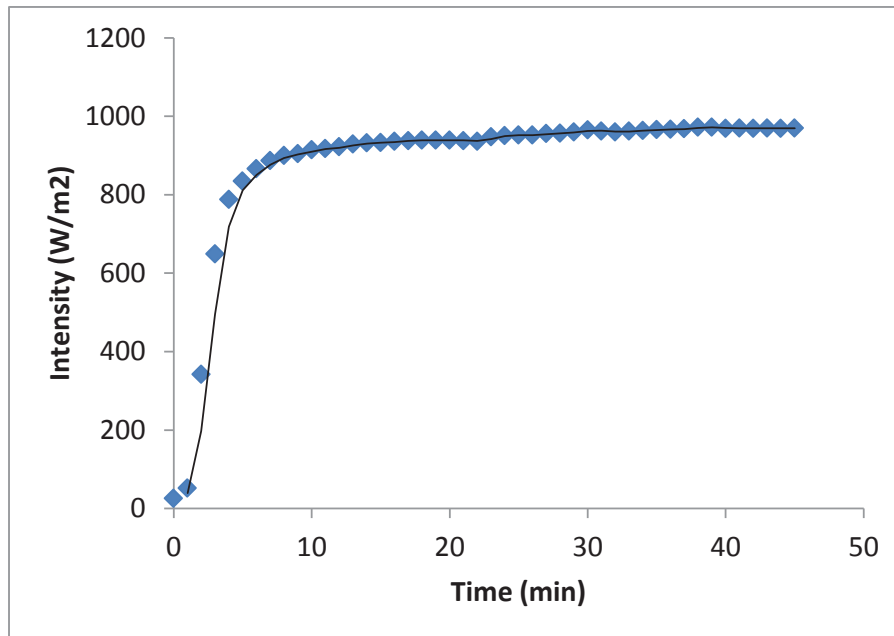


**Figure 4-24** Light Intensity as a Function of Time at 47 cm Table to Lamp Separation

We then marked a 120x120cm grid centered on the center of the table with 20cm interval spacing. We then proceeded to characterize the intensity distribution for table to lamp separation distances of 47cm, 52cm and 63cm. A typical contour plot is given in Figure 4-25 below. One can immediately notice here that the points beyond the 100x100cm square result in very poor light intensity as these locations are only lit by the single lamps near the edges – no overlap is available to increase intensity.

These are numerically summarized in Table 4.5 where the average and standard deviation of the intensity distributions are broken down by the smaller and larger squares. At 52cm, the uniformity over the 100x100cm square is predicted to be 17% - which is slightly higher than the modelled value of 12%. This can be a direct result of the 20cm spacing on the grid which we took our measurements. We can further refine this grid spacing to capture the uniformity and distribution with a higher degree of accuracy. The mean of 861 W/m<sup>2</sup> is somewhat higher than the predicted

value of  $777 \text{ W/m}^2$  – which again could be a direct result of inadequate sampling during the characterization. However when one considers the crude nature of the modeling approach, the resulting mismatch is not too unrealistic. Also based on these measurements and the inverse square law, one can predict a separation of 38cm to deliver a  $1000 \text{ W/m}^2$  average intensity over the  $100 \times 100 \text{ cm}$  square in the middle of the table.

This one is for 47 cm separation. Remaining two separations show similar characteristics.

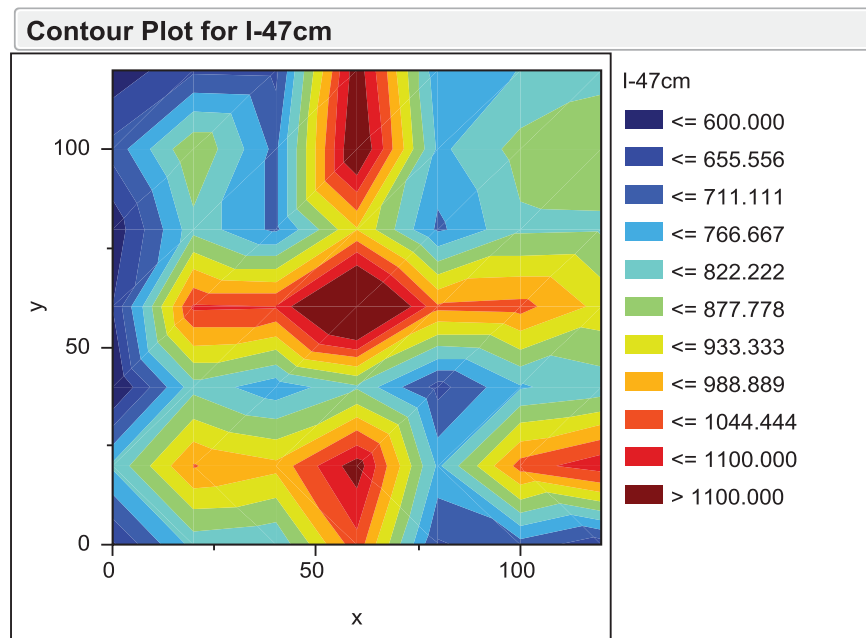


**Figure 4-25** Typical Contour Plots

**Table 4-5** Summary Statistics for Light Intensity Distribution

Separation	Area	Intensity		% Sigma
		Mean (W/m <sup>2</sup> )	Sigma	
47cm	100x100	891	171	19%
47cm	120x120	822	181	22%
52cm	100x100	861	147	17%
52cm	120x120	796	160	20%
63cm	100x100	802	102	13%
63cm	120x120	740	127	17%

#### **4.2.2. Test Run of the Light Soaking Station**

Light soaking station is successively run and the temperature and I – V measurements are done for four different locations in the station and for 2 different test modules (1 and 4 cells). Figure 4-26 shows how the temperature of the system is stabilized with respect to time.

The system is started simultaneously by powering up the lamps and the cooling fans. In order to see the effect of the cooling fans, at a specified time interval, fans are turned off and it could be seen in Figure 4-27 around time zone 390, the temperatures rises very quickly up to elevated levels which could be dangerous for the system. Therefore, it can be said that 10 cooling fans are very important for the stabilization of the temperature in the system.

The loss in performance is inline with the expectations based on the negative temperature coefficient at  $P_{max}$ . It is very difficult to make a quantitative analysis based on individual panels and PV technologies due to the large amount of scatter in the data. It seems from a qualitative perspective that there are no significant

differences between the panels. The range of quoted temperature coefficients are between 0.24 and 0.55; so one would expect to see some difference. However we would have to generate more data to observe these differences.

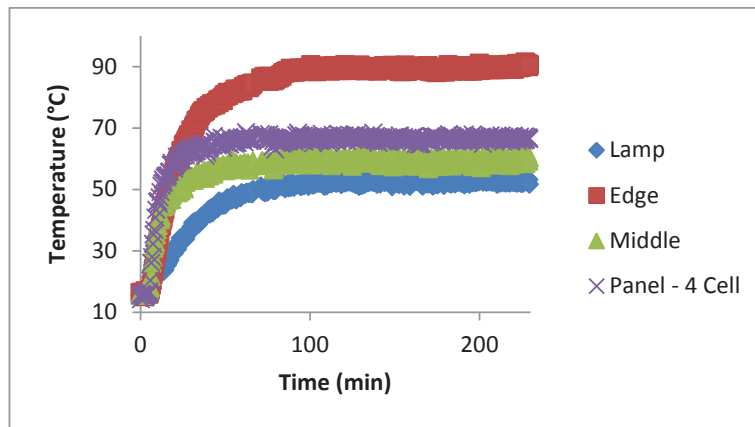


**Figure 4-26** Temperature vs Time Plot for Different Points in the LID Station

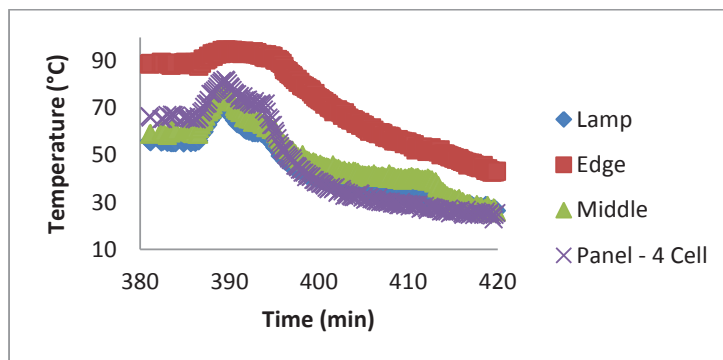


**Figure 4-27** Time Period when the Cooling Fans are Turned off

Figure 4-28 shows the effect of lamps and the illumination amount on the test module performances. In specified times during the trial experiment, some lamps are randomly closed to see the effect on the temperature and performance of the test modules. One can see by looking at Figure 4-28 that  $I_{SC}$  decreases as the illumination decreases while  $V_{OC}$  does not change with respect to the illumination conditions.

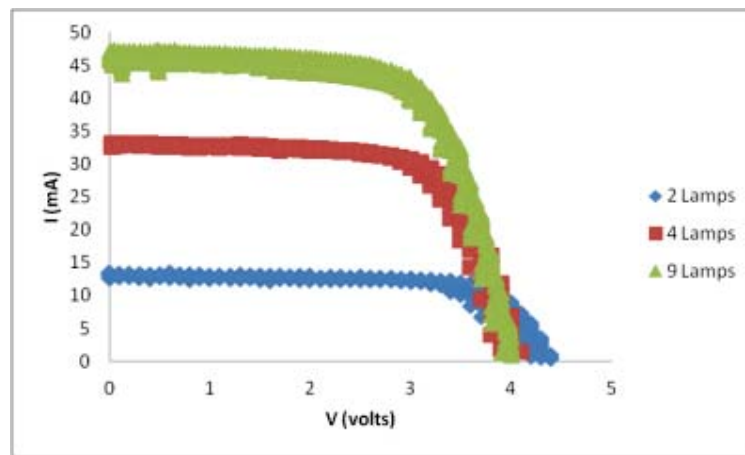


**Figure 4-28** I- V Curve under Different Illuminations for 1 Cell Module

The same behavior goes for the 4 cell module too, however if one looks closer to the data, it could be observed that  $V_{OC}$  is also changing for this module along with the  $I_{SC}$ .

The change in  $V_{OC}$  seems to be related with the changing temperature because of the decrease in the illumination in that area. Figure 4-30 shows the changing  $V_{OC}$  values and Figure 4-31 shows the correlation with the changing temperature.

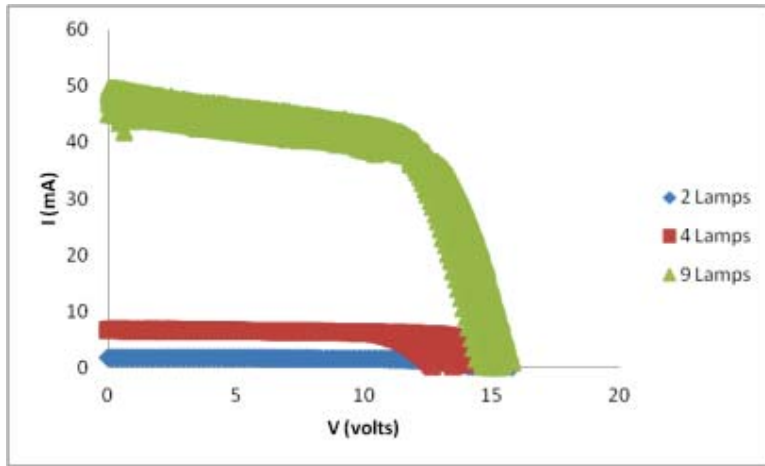


**Figure 4-29** I - V Curve under Different Illuminations for 4 Cell Module

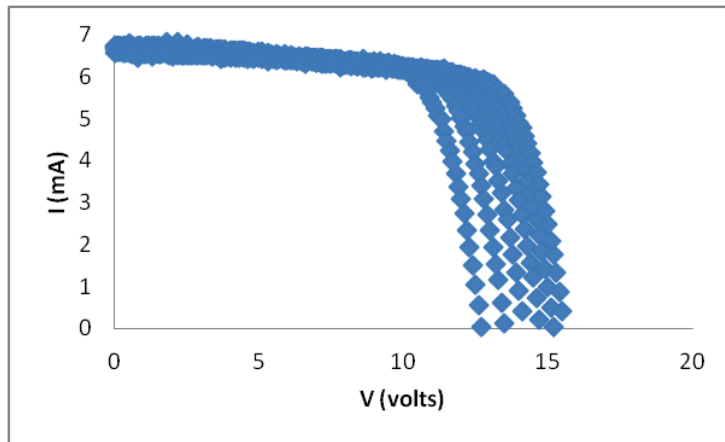


**Figure 4-30** Voc Change for 4 Cell Module

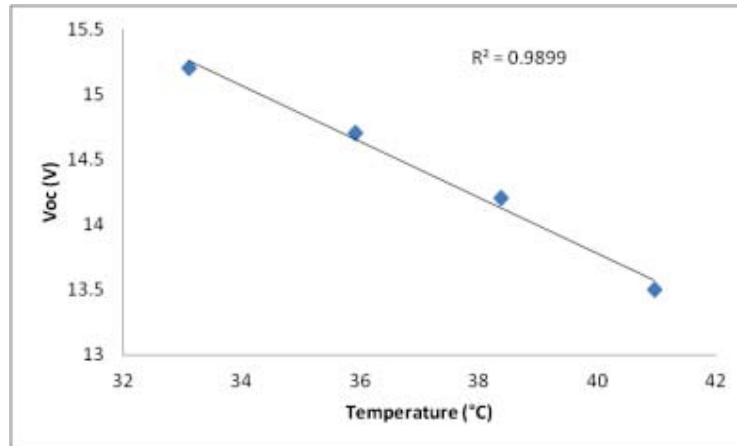


**Figure 4-31** Voc Temperature Relationship for 4 Cell Module

### 4.3. Future Improvements

Further items that need to be fine tuned or upgraded on the light soaking station include the modification of the characterization set-up to provide for adjustable loads for the panels being tested while their IV curves are not being captured (which can be achieved by the NI PXI-2527 switch for up to 8 panels simultaneously), upgrading of the cooling set-up to provide for active conductive cooling on the table surface and improvements to the user interface to further enhance user friendliness. Also additional ambient condition monitors such as a reference cell can be included in the set-up.



## CHAPTER 5

### SUMMARY AND CONCLUSIONS

In this study, the properties of commercial solar modules, characterization methods and the degradation modes are discussed. An outdoor test station consisting of a continuously working weather station and the module performance measuring I – V tracer is installed and a light soaking station is designed and operated in order to conduct accelerated tests for the sample modules. It is observed that continuous data collection requires high amount of automated hardware and software in order to fully avoid errors and data loss. It is also very important to backup the data stored in the outdoor station. For this purpose, An FTP server is established to automatically get the data from equipments and store them in a place that could be reached remotely and safely. Statistical analysis made upon the merging of the performance and meteorology data show that solar irradiation and temperature are primarily important for the performance of the solar modules. Other variables like pressure, humidity are of secondary concern. Solar irradiance collected by HOBO U30 Weather Station is calibrated considering the inclination of the modules along with the solar vector and latitude and longitude information. Performance metrics for the solar modules show that monocrystalline panels show better performance in terms of  $P_R$  than the polycrystalline and thin film technologies respectively. For the light soaking station, temperature control in the test chamber is very important to conduct accelerated tests in a stabilized environment. The designed system requires a stabilized temperature for the tests, however further modification is needed if the temperature is wanted to be hold in a specific value for testing purposes. In addition to that, the light soaking station designed in this study could characterize the sample modules with their temperature and I – V curve measurements on a basic basis.



## REFERENCES

- [1] T. J. M. Oliver, "The market for solar photovoltaics," *Energy Policy*, pp. 371-385, 1999.
- [2] V.V.Tyagi, "Progress in solar PV technology: Research and achievement," *Renewable and Sustainable Energy Reviews*, pp. 443-461, 2013.
- [3] "European Photovoltaic Industry Association," 2008. [Online]. Available: <http://www.epia.org/about-us/about-photovoltaics/solar-photovoltaic-technology/>.
- [4] Paolo Frankl, Stefan Nowak, Marcel Gutschner, Stephan Gnos, Tobias Rinke, "Technology Roadmap Solar photovoltaic energy," International Energy Agency, 2010.
- [5] "Photovoltaic (PV) Cell," 2011. [Online]. Available: <https://sites.google.com/site/reetech/home/photovoltaic> .
- [6] T. Saga, "Advances in crystalline silicon solar cell technology for industrial mass production," *NPG Asia Materials*, pp. 96-102, 2010.
- [7] Y. Chu, August 2011. [Online]. Available: <http://www.geni.org/globalenergy/research/review-and-comparison-of-solar-technologies/Review-and-Comparison-of-Different-Solar-Technologies.pdf>.
- [8] M. W. Alan Goodrich\*, "A wafer-based monocrystalline silicon photovoltaics road map: Utilizing known technology improvement opportunities for further reductions in manufacturing costs," *Solar Energy Materials & Solar Cells*, pp. 110-135, 2013.
- [9] G. Simbolotti, "Solar Photovoltaics Technology Brief," IEA-ETSAP, 2013.
- [10] R. H. Bube, *Photovoltaic Materials*, 1998.
- [11] Martin A. Green, Keith Emery, Yoshihiro Hishikawa, Wilhelm Warta, Ewan D. Dunlop, "Solar cell efficiency tables (version 42)," *Progress in Photovoltaics*, pp. 827-837, 2013.
- [12] "Energy Technology Perspectives," 2008.

- [13] R.W. Miles\*, K.M. Hynes, I. Forbes, "Photovoltaic solar cells: An overview of state-of-the-art cell development and environmental issues," *Progress in Crystal Growth and Characterization of Materials*, pp. 1-42, 2005.
- [14] A. Goetzberger, W. Shockley, "Journal of Applied Physics," p. 409, 1960.
- [15] Adolf Goetzberger, Christopher Hebling, Hans-Werner Schock, "Photovoltaic materials, history, status and outlook," *Reports: A Review Journal*, pp. 1-46, 2003.
- [16] M. A. Green, "Crystalline and thin-film silicon solar cells: state of the art and future potential," *Solar Energy*, pp. 181-192, 2003.
- [17] Bhubaneswari Parida, S. Iniyar, Ranko Goic, "A review of solar photovoltaic technologies," *Renewable and Sustainable Energy Reviews*, p. 1625–1636, 2011.
- [18] T. Markvart, *Solar Electricity*, 1995.
- [19] D. L. King and J. A. Hansen, "Proceedings of the 25th IEEE PV Specialists Conference," in *Dark current-voltage measurements on photovoltaic modules as a diagnostic or manufacturing tool*, 1997.
- [20] S. R. Rummel and T. J. McMahon, "13th NREL Photovoltaics Program Review," in *Effect of cell shunt resistance on module performance at reduced light levels*, Lakewood, 1995.
- [21] Edson L. Meyer and E. Ernest van Dyk, "IEEE TRANSACTIONS ON RELIABILITY," in *Assessing the Reliability and Degradation of Photovoltaic Module Performance Parameters*, 2004.
- [22] S. Durand, "Attaining Thirty-Year Photovoltaic System Lifetime," *Progress in Photovoltaics: Research and Applications*, 1994.
- [23] Wenger HJ, Schaefer J, Rosenthal A, Hammond B, Schlueter L., "Decline of the Carrisa Plains PV Power Plant: The Impact of Concentrating Sunlight on Flat Plates," in *22nd IEEE Photovoltaic Specialists Conference*, 1991 .
- [24] F. J. Pern, "Ethylene-vinyl acetate (EVA) encapsulants for photovoltaic modules: Degradation and discoloration mechanisms and formulation modifications for improved photostability," *Die Angewandte Makromolekulare Chemie*, pp. 195-216, 1997.

- [25] J. Pern, "Module Encapsulation Materials, Processing and Testing," Shanghai, 2008.
- [26] D. C. Jordan and S. R. Kurtz, "Photovoltaic Degradation Rates-an Analytical Review," *Progress in Photovoltaics: Research and Applications*, p. 12–29, January 2013.
- [27] W. H. Holley, S. C. Agro, J. P. Galica, L. A. Thoma, R. S. Yorgensen, M. Ezrin, P. Klemchuk, and G. Lavigne, "Investigation into the causes of browning in EVA encapsulated flat plate PV modules," in *Conference Record of the 24th IEEE Photovoltaic Specialists Conference*, Waikoloa, 1994.
- [28] D. Berman, S. Biryukov, and D. Faiman, "EVA laminate browning after 5 years in a grid-connected, mirror-assisted, photovoltaic system in the Negev desert: effect on module efficiency," *Solar Energy Materials and Solar Cells*, p. 421–432, April 1995.
- [29] Lawrence Dunn, Michael Gostein and Bill Stueve, "Literature Review of the Effects of UV Exposure on PV Modules," 2013.
- [30] Kempe, M.D., Jorgensen, G.J., Terwilliger, G.J., McMahan, T.J., Kennedy, C.E., Borek, T.T., "Acetic acid production and glass transition concerns with ethylene-vinyl acetate used in photovoltaic devices," *Solar Energy Materials & Solar Cells*, p. 315–329, 2007.
- [31] P. Klemchuk, M. Ezrin, G. Lavigne, W. Holley, J. Galica, and S. Agro, "Investigation of the degradation and stabilization of EVA-based encapsulant in field-aged solar energy modules," *Polymer Degradation and Stability*, p. 347–365, March 1997.
- [32] F. J. Pern and A. W. Czanderna, "EVA degradation mechanisms simulating those in PV modules," pp. 445-452, 1992.
- [33] M. Kempe, " Ultraviolet test and evaluation methods for encapsulants of photovoltaic modules," *Solar Energy Materials & Solar Cells*, p. 246–253, 2010.
- [34] Abdérafi Charki, Rémi Laronde, David Bigaud, "Accelerated degradation testing of a photovoltaic module," *Journal of photonics for energy*, 2013.
- [35] Ethan Wang, Hsinjin Edwin Yang, Jerry Yena, Sunny Chia, Carl Wang, "Failure Modes Evaluation of PV Module via Materials Degradation Approach," *Energy*

- Procedia*, pp. 256-264, 2013.
- [36] Claudio Ferrara and Daniel Philipp, “Why Do PV Modules Fail?,” *Energy Procedia*, pp. 379-387, 2012.
- [37] N. Bosco, “Reliability Concerns Associated with PV Technologies,” 2010.
- [38] M. Kemp, “Control of moisture ingress into photovoltaic,” in *31st IEEE Photovoltaic Specialists Conference and*, Florida, 2005.
- [39] Munoz, M.A., Alonso-Garcia, M.C., Nieves, V., Chenlo, F., “Early degradation of silicon PV modules and guaranty conditions,” *Solar Energy*, p. 2264–2274, 2011.
- [40] Carlson, D.E., Romerol, R., Willing, F., Meakin, D., Gonzalez, L., “Corrosion effects in thin film photovoltaic modules,” *Photovoltaics: Research and Applications*, p. 377–386, 2003.
- [41] Osterwald, C.R., Anderberg, A., Rummel, S., Ottoson, L., “Degradation Analysis of Weathered Crystalline-Silicon PV Modules,” in *IEEE Photovoltaic Specialists Conference*, New Orleans.
- [42] Ababacar Ndiaye, Abde'rafi Charki, Abdessamad Kobi, Cheikh M.F. Kebe., “Degradations of silicon photovoltaic modules: A literature review,” *Solar Energy*, p. 140–151, 2013.
- [43] Oreski, G., Wallner, G.M., “Evaluation of the aging behavior of ethylene copolymer films for solar applications under accelerated weathering conditions,” *Solar Energy*, pp. 1040-1047, 2009.
- [44] Kojima, T., Yanagisawa, T., “The evaluation of accelerated test for degradation a stacked a-Si solar cell and EVA films,” *Solar Energy Materials & Solar Cells*, pp. 119-123, 2004.
- [45] Wohlgemuth, J.H., Kurtz, S., “Reliability Testing Beyond Qualification as a Key Component in Photovoltaic’s Progress Toward Grid Parity,” in *IEEE International Reliability Physics Symposium*, California, 2011.
- [46] M. Kempe, “Modelling the moisture ingress into photovoltaic modules,” *Solar Energy Materials & Solar Cells*, p. 2720–2738, 2006.
- [47] Kaplanis, S., Kaplani, E., “Energy performance and degradation over 20 years performance of BP c-Si PV modules,” *Simulation Modeling Practice and Theory*,

pp. 1201-1211, 2011.

- [48] Lombardo T, Ionescu A, Lefe`vre RA, Chabas A, Ausset P, Cachier H, “Soiling of silica-soda-lime float glass in urban environment: measurements and modeling,” *Atmospheric Environment*, 2005.
- [49] Skoczek, A., Sample, T., Dunlop, E.D., Ossenbrink, H.A., “Electrical performance results from physical stress testing of commercial PV modules to the IEC61215 test sequence,” *Solar Energy Materials & Solar Cells*, p. 1593–1604, 2008.
- [50] Jansen, K.W., Delahoy, A.E., “A laboratory technique for the evaluation of electrochemical transparent conductive oxide delamination from glass substrates,” *Thin Solid Films* , p. 153–160, 2003.
- [51] Paula Sanchez-Friera, Michel Piliouguine, Javier Pelaez, Jesus Carretero and Mariano Sidrach de Cardona, “Analysis of degradation mechanisms of crystalline silicon PV modules after 12 years of operation in Southern Europe,” *Progress in Photovoltaics: Research and Applications*, pp. 658-666, 2011.
- [52] H. J. Möller, “Semiconductors for Solar Cells: Artech House,” p. 41–46, 1993.
- [53] E. L. Meyer and E. E. van Dyk, “Proceedings of the 17th European Photovoltaic Solar Energy Conference,” in *Monitoring I - V and performance parameters of photovoltaic modules*, 2001.
- [54] Stephan, M., Thomas, K., Wolfgang, J., Hurbert, F., “Proceedings of the 19th EU PVSEC,” in *Quality testing for PV modules according to standards and performance control for supporting manufacturing*, Paris, 2004.
- [55] Kempe MD, Jorgensen GJ, Terwilliger KM, McMahon TJ, Kennedy CE, Borek TT, “Proceedings of the 4th World Conference on Photovoltaic Energy Conversion,” in *Ethylene-vinyl acetate potential problems for photovoltaic packaging*, 2006.
- [56] Quintana, M.A., King, D.L., McMahon, T.J., Osterwald, C.R., “Commonly observed degradation in field-aged photovoltaic modules,” in *Proceedings 29th IEEE Photovoltaic Specialists Conference*, 2002.
- [57] Dallas, W., Polupan, O., Ostapenko, S., “Resonance ultrasonic vibrations for crack detection in photovoltaic silicon wafers,” *Measurement Science and Technology*, p. 852–858, 2007.

- [58] Rueland, E., Herguth, A., Trummer, A., Wansleben, S., Fath, P., “Optical l-crack detection in combination with stability testing for inline inspection of wafers and cells,” in *Proceedings of 20th EU PVSEC*, Barcelona, 2005.
- [59] Schütze, M., Junghanel, M., Friedrichs, O., Wichtendahl, R., Scherff, M., “Investigations Of Potential Induced Degradation Of Silicon Photovoltaic Modules,” in *26th European Photovoltaic Solar Energy Conference*, Hamburg, 2011.
- [60] P. Hacke, “37th IEEE PVSC,” in *System Voltage Potential-Induced Degradation*, 2011.
- [61] Molenbroek, E., Waddington, D.W., Emery, K.A., “Hot spot susceptibility and testing of PV modules,” in *Conference Record of the 22th IEEE*, Las Vegas, 1991.
- [62] Rauschenbach, H., Mauder, E.E., “Breakdown phenomena in reverse biased silicon solar cells,” in *Proceeding 9th photovoltaic specialist’s conference*, 1972.
- [63] W. Hermann, W. Wiesner, W. Vaaen, “Proceedings of the 26th IEEE PV Specialists Conference,” in *Hot spot investigations on PV modules-new concepts for test standard and consequences for module design with respect to bypass diodes*, 1997.
- [64] E. E. van Dyk, B. J. Scott, E. L. Meyer, and A. W. R. Leitch, “Temperature dependence of performance of crystalline silicon photovoltaic modules,” *South African Journal of Science*, p. 198–200, 2000.
- [65] Changwoon, H., Nochang, P., Jaeseong, J., “Photovoltaic Module Reliability Workshop,” in *Lifetime prediction of silicon PV module ribbon wire in three local weathers*, 2012.
- [66] T. McMahon, “Accelerated Testing and Failure of Thin-film PV Modules,” *Progress in Photovoltaics: Research and Applications*, p. 235–248, 2004.
- [67] D. L. Staebler and C. R. Wronski, “Reversible conductivity changes in discharge-produced amorphous Si,” *Applied Physics Letters*, p. 292–294, 1977.
- [68] J. Yang, A. Banerjee, T. Glatfelter, S. Sugiyama, and S. Guha, “Proceedings of the 26th IEEE Photovoltaic Specialists Conference,” in *Recent progress in amorphous silicon alloy leading to 13% stable cell efficiency*, 1997.
- [69] R. Biswas and B.C. Pan, “Mechanisms of metastability in hydrogenated



- amorphous silicon,” *Solar Energy Materials and Solar Cells*, pp. 447-467, 2003.
- [70] Stutzmann, M.; Jackson, W.B. & Tsai, C.C., “Light-Induced Metastable Defects in Hydrogenated Amorphous Silicon: A Systematic Study,” *Physical Review B*, pp. 23-47, July 1985.
- [71] M.C. Rossi, M.S. Brandt, and M. Stutzmann, “Accelerated stability test for amorphous silicon solar cells,” *Applied Physics Letters*, pp. 1709-1711, 1992.
- [72] A. Luque and S. Hegedus, *Handbook of photovoltaic science and engineering*, John Wiley and Sons, 2003.
- [73] R. Ruther, J. del Cueto, G. Tamizh-Mani, A. Montenegro, S. Rummel, A. Anderberg, and B. von Roedern, “33rd IEEE Photovoltaic Specialists Conference,” in *Performance test of amorphous silicon modules in different climates - year four: Progress in understanding exposure history stabilization effects*, 2008.
- [74] J.A. del Cueto and B. von Roedern, “Temperature-induced changes in the performance of amorphous silicon multi-junction modules in,” *Progress in Photovoltaics: Research and Applications*, pp. 101-112, 1999.
- [75] Chin, K. K.; Gessert, T.A. & Su-Huai, W., “Proceedings of the 35th IEEE Photovoltaics Specialists Conference,” in *The Roles of Cu Impurity States in CdTe Thin Film Solar Cells*, Honolulu, 2010.
- [76] Dobson, K.D.; Visoly-Fisher, I.; Hodes, G. & Cahen, D., “Thin-Film Solar Cells,” *Solar Energy Materials and Solar Cells*, pp. 295-325, May 2000.
- [77] Powell, R.C.; Sasala, R.; Rich, G.; Steele, M.; Bihn, K.; Reiter, N.; Cox, S. & Dorer, G., “Proceedings of the 25th IEEE Photovoltaic Specialists Conference,” in *Stability Testing of CdTe/CdS Thin-Film Photovoltaic Modules*, Washington, 1996.
- [78] Batzner D.; Romeo, A.; Terheggen, M.; Dobeli, M.; Zogg, H. & Tiwari, A.N., “Stability Aspects in CdTe/CdS Solar Cells,” *Thin Solid Films*, pp. 536-543, 2004.
- [79] Degrave S.; Nollet P.; Stojanoska G.; Burgelman M. & Durose K., “Proceedings of 17th International Photovoltaic Science and Engineering Conference,” in *Interpretation of Ageing Experiments on CdTe/CdS Solar Cells*, Fukuoka, 2007.

- [80] V. Solanki, *Solar Photovoltaics: Fundamentals Technologies And Applications*, PHI Learning Pvt. Ltd., 2009.
- [81] A. Romeo, M. Terheggen, D. Abou-Ras, D.L. Bätzner, F. Haug, M. Kälin, D. Rudmann, and A.N. Tiwari, "Development of thin-film Cu(In,Ga)Se<sub>2</sub> and CdTe solar cells," *Progress in Photovoltaics: Research and Applications*, pp. 93-111, 2004.
- [82] R.A. Sasala, R.C. Powell, G.L. Dorer, and N. Reiter, "AIP Conference Proceedings," in *Recent progress in CdTe solar cell research at SCI*, 1997.
- [83] J.F. Hiltner and J.R. Sites, "AIP Conference Proceedings," in *Stability of CdTe solar cells at elevated temperatures: Bias, temperature, and Cu dependence*, 1999.
- [84] A. Pudov, M. Gloeckler, S. Demtsu, J. Sites, K. Barth, R. Enzenroth, and W. Sampath, "Photovoltaic Specialists Conference," in *Effect of back-contact copper concentration on CdTe*, 2002.
- [85] Guillemoles, J.-F.; Kronik, L.; Cahen, D.; Rau, U.; Jasenek, A. & Schock, H.-W., "Stability Issues of Cu(In,Ga)Se<sub>2</sub>-Based Solar Cells," *Journal of Physical Chemistry B*, pp. 4849-4862, 2000.
- [86] Schmidt, M.; Braunger, D.; Schäffler, R.; Schock, H.W. & Rau, U., "Influence of Damp Heat on the Electrical Properties of Cu(In,Ga)Se<sub>2</sub> Solar Cells," *Thin Solid Films*, pp. 283-287, February 2000.
- [87] U. Rau, M. Schmitt, J. Parisi, W. Riedl, and F. Karg, "Persistent photoconductivity in Cu(In,Ga)Se<sub>2</sub> heterojunctions and thin films prepared by sequential deposition," *Applied Physics Letters*, pp. 223-225, 1998.
- [88] R. Sasala and J. Sites, "Photovoltaic Specialists Conference," in *Time dependent voltage in CuInSe<sub>2</sub> and CdTe solar cells*, 1993.
- [89] Malmström, J.; Wennerberg, J. & Stolt, L., "A Study of the Influence of the Ga Content on the Long-Term Stability of Cu (In,Ga)Se<sub>2</sub> Thin Film Solar Cells," *Thin Film Solids*, pp. 436-442, May 2003.
- [90] Igalson, M.; Wimbor, M.; Wennerberg, J. , "The Change of the Electronic Properties of CIGS Devices Induced by the Damp Heat Treatment," *Thin Solid Films*, pp. 320-324 , February 2002.

- [91] A. Klaver and R. van Swaaij, "Modeling of light-induced degradation of amorphous silicon solar cells," *Solar Energy Materials and Solar Cells*, pp. 50-60, 2008.
- [92] S. Kalogirou, *Solar energy engineering: processes and systems*, Academic Press, 2009.
- [93] Razykov TM, Ferekides CS, Morel D, Stefanakos E, Ullal HS, Upadhyaya HM, "Solar photovoltaic electricity: current status and future prospects," *Solar Energy*, p. 580–608, 2011.
- [94] Becker C, Sontheimer T, Steffens S, Scherf S, Rech B, "Polycrystalline silicon thin films by high rate electron beam evaporation for photovoltaic applications influence of substrate texture and temperature," *Energy Procedia*, p. 1–5, 2011.
- [95] A. Acevedo, "Thin film CdS/CdTe solar cells: Research Perspectives," *Solar Energy*, pp. 675-681, 2006.
- [96] Barnett AM, Rand JA, Hall RB, Bisailon JC, DelleDonne EJ, Feyock BW, Ford DH, Ingram AE, Mauk MG, Yasko JP, Sims PE, "High current thin silicon ceramic solar cell," *Solar Energy Materials & Solar Cells*, pp. 645-650, 2010.
- [97] Kumar R, Rosen MA, "A critical review of photovoltaic-thermal solar collectors for air heating," *Applied Energy*, p. 3603–3614, 2011.
- [98] Ali AHH, Matsushita Y, Ookawara S, "Photovoltaic module thermal regulation: effect of cell arrangement configurations on the performance," *International Journal of Thermal & Environmental Engineering*, pp. 241-247, 2011.
- [99] Eikelboom JA, Jansen MJ, "Characterisation of PV modules of new generations. Results of tests and simulations," *Solar Energy*, p. 1291–1301, 2011.
- [100] El-Sebaï AA, Al-Hazmi FS, Al-Ghamdi AA, Yaghmour SJ, "Global, direct and diffuse solar radiation on horizontal and tilted surfaces in Jeddah, Saudi Arabia," *Applied Energy*, p. 568–576, 2010.
- [101] Demain C, Journée M, Bertrand C, "Evaluation of different models to estimate the global solar radiation on inclined surfaces," *Renewable Energy*, p. 710–721, 2013.
- [102] Yadav AK, Chandel S, "Tilt angle optimization to maximize incident solar radiation: a review," *Renewable and Sustainable Energy Reviews*, pp. 503-513,

- [103] “Photovoltaic system performance monitoring—guidelines for measurement, data exchange and analysis,” Geneva, 1998.
- [104] Marion B, Adelstein J, Boyle K, Hayden H, Hammond B, Fletcher T. et al, “31st IEEE, photo- voltaic specialists conference,” in *Performance parameters for grid-connected PV systems*, 2005.
- [105] Ayompe LM,Duffy A,McCormackSJ,Conlon M, “Measured performance of a 1.72kW roof top grid connected photovoltaic system in Ireland,” *Energy Conversion and Management*, p. 816–825, 2011.
- [106] Emmanuel K,Kalykakis S,Papazoglou TM, “Performance analysis of a grid connected Photovoltaic Park on the island of Crete,” *Energy Conversion and Management*, pp. 433-438, 2009.
- [107] Pietruszko SM, Fetlinski B, Bialecki M., “IEEE, photovoltaic specialists conference,” in *Analysis of the performance of grid connected photovoltaic system*, 2009.
- [108] Pietruszko SM,Gradzki M, “Performance of a grid connected small PV system in Poland,” *Applied Energy*, pp. 177-184, 2003.
- [109] Soa JH,Jung YS,Yu GJ,Choi JY,Choi JH, “Performance results and analysis of 3 kW grid-connected PV systems: Field Demonstration Test Center in South Korea,” *Renewable Energy*, pp. 1858-1872, 2007.
- [110] Sharma V,Chandel SS, “Performance analysis of a 190kWp grid interactive solar photovoltaic power plant in India,” *Energy*, pp. 476-485, 2013.
- [111] Makrides G,Zinsser B,Norton M,Georghiou GE,Schubert M,Werner JH, “Potential of photovoltaic systems in countries with high solar irradiation,” *Renewable and Sustainable Energy Reviews*, pp. 754-762, 2010.
- [112] Adhikari S,Kumar S,Siripuekpong P, “Performance of household grid- connected PV system in Thailand,” *Progress in Photovoltaic Research and Applications*, pp. 557-564, 2003.
- [113] Ruther R,Knob P,Beyer HG,Dacoregio MM,Montenegro AA, “Third world conference, photovoltaic energy conversion,” in *High performance ratios of a double-junction a-SiBI PV grid-connected installation after five years of continuous operation in Brazil*, 2003.

- [114] R. S. Y. L. Vicky Svidenko.USA / Houston, TX Patent US 2010/0073011 A1, 2010.
- [115] “Heraeus Noblelight,” 2013. [Online]. Available: [http://www.heraeus-noblelight.com/en/applications/arcflashlamps\\_1/af\\_photovoltaics/af\\_photovoltaics\\_1.aspx](http://www.heraeus-noblelight.com/en/applications/arcflashlamps_1/af_photovoltaics/af_photovoltaics_1.aspx).
- [116] “Simulation of Solar Irradiation,” 1996. [Online]. Available: <http://www.newport.com/Technical-Note-Simulation-of-Solar-Irradiation/411986/1033/content.aspx>.
- [117] 2013. [Online]. Available: [http://www.kimo.fr/produits/243/sl\\_100.html?lang=en](http://www.kimo.fr/produits/243/sl_100.html?lang=en).
- [118] Pern, F.J.; Czanderna, A.W.; Emery, K.A. & Dhere, R.G., “22nd IEEE Photovoltaic Specialists Conference,” in *Weather Degradation of EVA Encapsulant and the Effect of its Yellowing on Solar Cell Efficiency*, Las Vegas, 1991.